Gas-Phase Redox Dynamics in High-Energy Collisions

Anders Nielsen, MSc.

Thesis submitted to the University of Nottingham for the degree of Doctor of Philosophy

October 2009

Abstract

Mass analysed ion kinetic energy (MIKE) spectra following collisions have been recorded using a double focusing mass spectrometer with 5 kV acceleration voltage. Metal complexes studied were formed by pick-up of metal atoms in mixed argon/solvent clusters made by supersonic expansion. DFT calculations were used to rationalise experimental data.

Complexes of the form ML_n^+ where M = Mg, Ca, Mn, Cu, and Zn while L = NH_3, CO_2, benzene, pyridine, acetonitrile, and acetone have been collided with O_2 and MgL_n^+ also with CO_2, N_2O, acetonitrile, and benzene. Complexes with few ligands are the most prone to oxidation due to their high speed which facilitates electron transfer. Calculated electron affinities, Mulliken populations, and natural bond orbitals of collision gases were used to rationalise electron transfer trends. Collision gases trap electrons more efficiently if they have π-bonds or adjacent electronegative atoms.

Metal complex and molecular dications were collided with H_2 and O_2 to determine the stability of their reduced products. No systematic differences were found between collisions with the two gases at the collision energies examined. The fate of monocations formed in collision depends on their relaxation energy and the dissociation energy of relaxed monocations. LZ theory was unable to explain MIKE spectra.

Metal complexes ML_n^+ and ML_n^{2+} were collided with O_2 to determine the propensity to form MXL_{n-m}^+ where M = Mg, Ca, Mn, Cu, and Zn while L = CH_3X with X = F and Cl. Reactivity is determined by the IE of ML_n^+ which decrease with increasing n. Dications due to their high dissociation energy are much more likely to react as they can have enough internal energy to overcome potential barriers.

Acknowledgements

I would like to thank Tony Stace my supervisor for accepting me as a student. Thanks to Bridgette Duncombe for the many times she has fixed the machine I have recklessly broken. Thanks to Niel Barnes and the workshop for doing the supply work needed to keep the ZAB working. Thanks to my lab colleagues for the good times and many laughs I have had working here. Thanks to Tony, Ivan, Nick, Adrian, Rossana for proof reading this thesis. Thanks to my parents for visiting me in Nottingham and abroad in Spain and Norway. Thanks to Rossana and Tim for the many parties held in their house. Thanks to Penny and Tony for the party in their house. Thanks to Khadar, Dennis, Dino, Hamish, Xiao, and Guohua for interesting discussions offering viewpoints and knowledge from other parts of the world.

Table of contents

List of Abbreviations

Acronym	Explanation	Section
BDE	Bond Dissociation Energy	1.2
CI	Chemical Ionisation	2.2.7
CID	Collision Induced Dissociation	2.3.2
COB	Classical Over Barrier model	1.1.4
DFT	Density Functional Theory	
EA	Electron Affinity	1.2
ECP	Effective Core Potentials	2.4
EI	Electron Impact ionisation	2.2.7
FFR	Field Free Region	2.2.10
HF	Hartree-Fock	
HOMO	Highest Occupied Molecular Orbital	
IE	Ionisation Energy	1.2
LUMO	Lowest Unoccupied Molecular Orbital	
LZ	Landau-Zener theory	1.6
MIKE	Mass analysed Ion Kinetic Energy	2.3.2
MS	Mass Spectrum	2.3.1
PBN	Pyrolytic Boron Nitride	2.2.9
RE	Recombination Energy	1.2

Chapter 1
Introduction

1.1 Introduction

Collisions between fast moving projectiles and static target gases can be examined experimentally. Electron transfer may occur during such collisions and it is desirable to have knowledge about the dynamics of various electron transfer reactions.

The first result chapter in this work regards collisions where projectiles collide with target gases and become cationic. The second chapter regards collisions where dications collide with target gases and become monocationic. Finally a redox reaction is also examined which does not permute the overall charge of a cluster. Instead an atomic metal ion abstracts halogen atoms from surrounding organic halides. Each of these reactions will be described in the following three subsections which include reactions and background literature.

1.1.1 Charge stripping

Fast moving neutral projectiles can become ionised upon collision with neutral target gases. The electrons removed from projectiles can be trapped by target gases or they can be ejected into the continuum. The two processes are described in Reactions R1.1 and R1.2.

$$P + T \rightarrow P^{+} + T^{-} \qquad \text{(R1.1)}$$

$$P + T \rightarrow P^{+} + T + e^{-} \qquad \text{(R1.2)}$$

The potential energy curves describing Reaction R1.1 are shown in Figure 1.1.

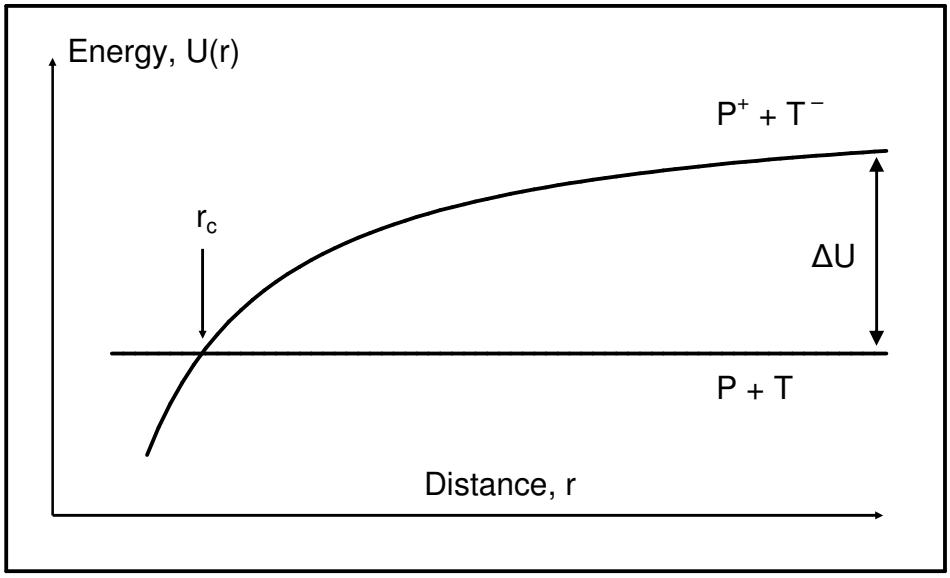

Figure 1.1 Potential energy curves for charge stripping. The two curves describe reactants and products in Reaction R1.1 with r_c denoting the curve crossing distance. ΔU describes the reaction energy for the reaction.

According to LZ theory electron transfer occurs in Reaction R1.1 at the distance where the Coulomb potential arising from the ion pair crosses the negligible dispersion potential between the two neutral species. Reaction R1.1 converts translational kinetic energy into potential energy as the products attract each other.

This work theoretically examines the effect of different collision gases on projectile ionisation in fast collisions. It attempts to understand why gases have different charge stripping efficiencies rather than trying to experimentally measure those efficiencies. To this end a model is employed using electron affinities of target gases and centrifugal barriers derived from angular momenta of LUMO orbitals. The

experimental section also includes studies of the effect of different projectiles on charge stripping efficiency. Reactions R1.3 and R1.4 are studied experimentally in the mass spectrometer in this work and are likely to give information about Reactions R1.1 and R1.2.

$$P^+ + T \rightarrow P^{2+} + T^- \quad \text{(R1.3)}$$

$$P^+ + T \rightarrow P^{2+} + T + e^- \quad \text{(R1.4)}$$

Literature on charge stripping

One study by Danis *et al*. [1] revealed the following trend in the ability of selected species to remove electrons from a series of fast moving neutral molecules O_2 > NO > Cl_2 > NO_2 > N_2 > He > CH_4 > SF_6 > Xe. The study also went on to say the species from O_2 to N_2 can capture electrons from fast moving neutral species according to Reaction R1.1. In contrast the species from He to Xe only remove electrons from their collision partners via Reaction R1.2. While it is likely that the vertical EA plays some role in the ability to abstract electrons it does not give a complete description. It is poorly understood why O_2 whose vertical EA is -91 meV [2] is so good at abstracting electrons from collision partners. By comparison C_{60} whose EA is 2.67 eV [3] is not nearly as efficient as O_2 at trapping electrons [4].

Anions were produced following collision of $FeCl_m^+$ with Xe [5] and O_2^+ with noble gases and with Hg [6]. Electron transfer in collisions from neutral alkali metal projectiles to isotropically oriented neutral target gases include the target gases O_2, Cl_2, Br_2 [7], CH_3NO_2, CF_3Br, CF_3I [8], CO_2, OCS, and CS_2 [9], Cl_2, Br_2, I_2, CO, N_2,

NO_2 [10], CH_3CN [11], MF_6 for M = S, Se, Te, Mo, W, Re, Ir, and Pt [12], C_6F_6 [13], p-quinone [14]. These collisions occurred at low energies and it was concluded that the cationic collision partner and the long collision time helped form stable or long lived anions. Formation of stable anions would often not be possible in vertical high energy collisions or by attachment of free electrons. Collisions between alkali metals and target gases were frequently used to determine the EA of molecules and often anions produced by fragmentation of the target gas was observed. Scott studied collisions of Na^- and K^- ions with H_2, D_2, N_2, O_2, CO, CO_2, CH_4 in the energy range 1-300 eV in the lab frame. Detachment was found as the dominating reaction in all cases except O_2 and long lived anion production was found for O_2 and CO_2. In most cases detachment could be described by an optical model [15]. Nielsen found RuL_3^- (L = bipy and phen) following multiple collisions of RuL_3^{2+} precursors with Na [16].

Brooks studied collisions of neutral alkali metals with oriented polar molecules including CH_3NO_2 [17] and CH_3CN, CH_3NC, and CCl_3CN [18]. From these studies it was observed that electron transfer is favoured when the alkali metal pass close through the part of the target gas containing the LUMO relative to passage through a far end of the target gas molecule. Anion producing collisions even included cases where the reactant was already anionic but upon collision became dianionic. Anions collided with Na producing dianions included deprotonated AMP [19], $Fe(CN)_4^-$ [20], $TCNQ^-$ [21], and C_{60}^- [22]. Landau Zener theory [23] is still being used to rationalise cross sections in anion producing reactions [24].

Summary

Many unstable anions can be produced in high or even low energy collisions with alkali metals being the best electron donors among neutral collision partners. LZ theory is still being used to calculate capture cross sections despite obvious limitations.

1.1.2 Charge recombination

Collisional charge recombination is the process where an electron is transferred from a neutral target to a dicationic projectile as displayed in Reaction 1.5. The process is called several names where the first part is either charge or electron while the last part is either recombination, transfer, or exchange.

$$P^{2+} + T \rightarrow P^{+} + T^{+} \qquad \text{(R1.5)}$$

The associated potential energy curves for Reaction R1.5 are given in Figure 1.2.

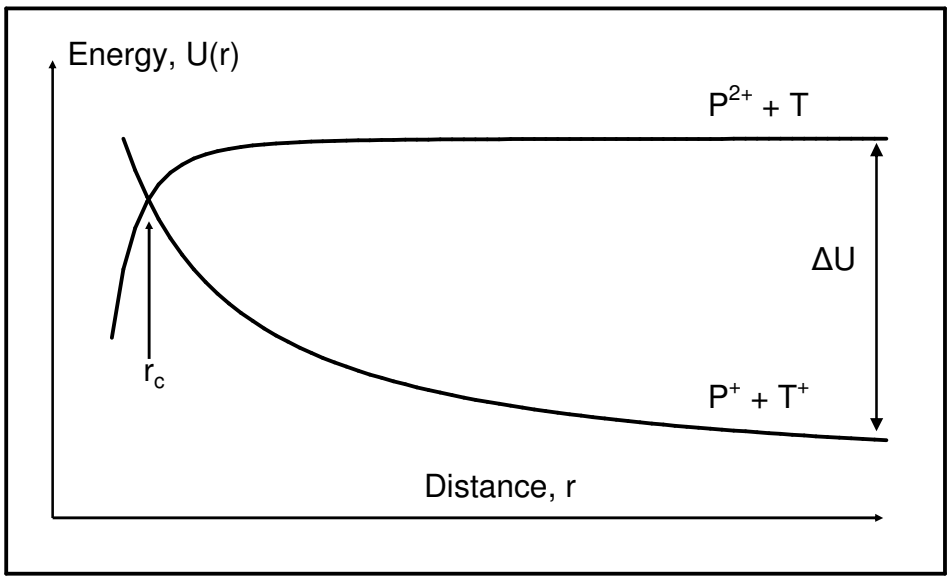

Figure 1.2 Potential energy curves for charge recombination. The two curves describe reactants and products in Reaction R1.5 with r_c denoting the curve crossing distance. ΔU describes the reaction energy for the reaction.

According to LZ theory charge exchange occurs at the distance where the repulsive Coulomb potential crosses the attractive polarisation potential. This time potential energy is converted to translational kinetic energy as the two monocations repel each other. The energy available in Reaction R1.5 is often sufficiently large to form excited states of the resulting projectile or target cations. Excited states of projectiles can be expected to fragment prior to detection if the excitation energy is higher than the dissociation energy of the weakest bond in the projectile and the excited state is adiabatically coupled to the separated fragments.

Part of the chapter on recombination involves an examination of the requirements to observe intact projectile monocations. Another topic examined is the fragmentation pattern exhibited by projectiles upon recombination.

Literature on charge recombination

Herman studied translational energy spectra following high energy collision of CO^{2+} with He, Ne, Ar, Kr, and Xe. The resulting CO^{+} ions were formed in increasingly electronically excited states as the IE of the target gases decreased. Xe^{+} was also formed in an excited state [25]. March studied metastable decay of C_2DH^{2+} in a high energy beam and found presence of non-dissociative recombination following collision with background gas [26]. Reid studied MIKE spectra of CO_2^{2+} and OCS^{2+} following high energy collisions with He and Xe. Wide fragment peaks were observed in the spectra and the abundance of the most abundant ions in each spectra were in the order of 2-4 % of the abundance of the intact monocations formed [27]. Nagesha studied MIKE spectra following high energy collision of SF^{2+} with He and found the abundance of S^{+} formed by charge separation to slightly less than that formed by dissociation upon electron transfer from He [28]. Koslowski studied translational energy spectroscopy following high energy collisions of N_2^{2+} with He, Ne, and Ar [29]. Leyh studied translational energy spectra following high energy collisions of NH_3^{2+} with He, Ne, Ar, Kr, Xe, and C_6H_6. The resulting NH_3^{+} ion became increasingly excited as the IE of the collision gas decreased and excited states of $C_6H_6^{+}$ were formed when C_6H_6 was the target gas. Following collision of NH_3^{2+} with Ar the mass region 13-17 amu was scanned and the abundance of the most abundant fragment ion NH_2^{+} was 15 % of that of NH_3^{+} [30]. Leyh studied collision of CCl_2^{2+} with 8 different target gases. Cross sections for production of CCl_2^{+} and CCl^{+} were high for the lowest IE gases and low for the highest IE gases. Production of CCl_2^{+} had a maximum for target gases with IE around 12 eV while production of CCl^{+} decreased steadily with increasing IE of the target gas. Energy releasing reactions were modeled by the Landau Zener model and energy demanding by the Demkov model which

could explain the non-zero cross sections for energy demanding reactions [31]. Schröder studied collisions of $FeCl_m^{2+}$ with He and O_2 and found that non-dissociative charge exchange was much more probable upon energy releasing reaction with O_2 than energy demanding reaction with He [5]. Schröder studied collisions of $C_4H_3^{2+}$ with He and O_2. Intact $C_4H_3^+$ was formed only upon collision with O_2 as charge exchange with O_2 is energy releasing in contrast to charge exchange with He [32]. Nielsen studied collisions of RuL_3^{2+} for L = bipy and phen with He, O_2, and Na. While RuL_3^+ was not observed following collisions with He the cross sections for its formation was in the order of 1-2 Å upon collision with O_2 and 100 Å upon collision with Na [16].

It might be imagined that excited dissociative states are formed upon reduction of doubly charged metal complexes. Duncombe studied high energy collisions of ZnL_n^{2+} for L = CO_2, Me_2CO, MeCN, C_5H_5N, C_6H_6, and Ar while n = 3, 4, and 5 with air and did not observe non-dissociative recombination [33]. Stone studied low energy collisions of $Cu(H_2O)_n^{2+}$ complexes and found no presence of non-dissociative recombination [34]. Seto studied low energy collisions of $Cu(CH_3CN)_n^{2+}$ for n = 2, 3, and 4 with Ar and found no non-dissociative recombination. Non-dissociative recombination of metal complexes was however observed with various molecular collision gases [35].

Price examined low energy collisions between molecular dications and neutral molecules and observed reactions included bond forming reactions [36]. Low energy collisions of CO^{2+} [37] and CF^{2+} and CF_2^{2+} [38] with He, Ne, Ar, Kr, and Xe were performed. Dominating reactions were Coulomb explosion of the dication for high IE

target gases, non-dissociative electron transfer for medium IE target gases, and dissociative electron transfer for low IE target gases.

Summary

In high energy collisions of molecular dications product ion formed by non-dissociative electron transfer dominates for energy releasing or resonant but not necessarily for energy demanding electron transfer. Cross sections for energy demanding electron transfer are low for high energy collisions and even lower for low energy collisions. Three energy regimes exists. Insufficiently energy releasing reactions ($\Delta U_r > -2.5$ eV) rarely occur. Instead the reactants fragment so they either form smaller dications or undergo Coulomb explosion. Moderately energy releasing electron transfers (-2.5 eV $> \Delta U_r > -7$ eV) result in intact products but strongly energy releasing electron transfers ($\Delta U_r < -7$ eV) often lead to dissociation due to formation of dissociative excited states.

1.1.3 Metal halides

Abstraction of halide atoms (X) from organic halides (XR) leaving organic radicals (R) is a common reaction in condensed phase chemistry with alkali metals displaying the highest reactivity. Halide abstraction reaction in the gas phase is a problem of both fundamental and practical importance. The fundamental part regards reactivities and barrier heights while the practical part regards synthetic routes towards salts in the gas phase. Salts are typically refractive and hygroscopic making them unsuitable for mass spectrometric studies and their generation *in situ* would alleviate those problems.

It has been observed that contrary to Landau Zener predictions EAs of neutral compounds turn out to be a poor indicator of their ability to trap electrons in collisions. In order to find trends in the ability to trap electrons it is desirable to examine a wide range of types of compounds including ionic compounds which frequently have high EAs.

Crystal field theory [39] and ligand field theory [40] are simple qualitative applications of molecular orbital theory [41-43] for metal complexes and they can give predictions about the geometry of metal complexes. Schematic energy level diagrams are freely available for crystal fields of common geometries [44]. According to crystal field theory and ligand field theory certain prediction can be made. Four coordinate Cu^{2+} complexes ($4s^0 3d^9$) complexes prefer square planar geometry. For $M(XR)_n^{2+}$ complexes with $n > 2$ and M = Mg, Ca, Mn, and Zn the centre of mass of the halide atoms is likely to be spatially close to the metal atom. This is especially the case if the radius of X greatly exceeds the radius of M and n is large as these factors enhance steric repulsion. Correspondingly the centre of mass of the halide atoms will be offset from the metal atom in $M(XR)_n^{+}$ complexes due to repulsion of the s electron. These predictions are used to justify application of otherwise questionable data from calculations in this work as certain optimised structures are low energy transition states rather than minima.

This work examines abstraction of electronegative atoms in small molecules by metal atoms by means of collisional activation and by electron impact.

Literature on metal halides

Schröder managed to make $FeCl_n$ compounds in the gas phase for MS studies following either vaporisation of $FeCl_3$ or reaction of $Fe(CO)_5$ with Cl_2 but warned about incompatibilities with the ion source [5]. This work included vaporisation of $FeCl_3$ in the high temperature oven but also the subsequent failure and replacement of two turbomolecular pumps that pump the oven chamber. Walker studied microwave spectra of metal complexes in the gas phase made by laser vaporisation of metals which reacted with SF_6, Cl_2, and Br_2 and subsequently with CO to produce OCCuX [45] and OCAgX [46]. Zhao studied reactions of 46 different atomic cations with RX = CH_3F probing Reaction R1.6.

$$M^+ + RX \rightarrow MX^+ + R \qquad \text{(R1.6)}$$

It was found that main group II to side group V metals and germanium undergo reaction R1.6. W, Os, Ir, and Pt by reacted by $MCHF^+$ formation and As by $AsCH_2^+$ formation. Reactions of Tc and Po were not probed and reactions of K and Se were not observed. The rest of the elements reacted by clustering of CH_3F on the atomic cation [47]. Cornehl studied reaction of six lanthanide metals with six different organic fluorides in a FT-ICR mass spectrometer and found that fluorine abstraction occurred from CF and CF_2 groups but not from CF_3 groups or CF_4 due to the higher BDE of such groups arising from the electron withdrawing F atoms. Furthermore the reactivity of M^+ was largely determined by IE(M^+) which thus provides an 'IE indicator' for reactivity [48]. The 'IE indicator' works for s,d, and f block metals within a single charge state. Thus it can be used to compare the reactivity of different M species or different M^+ species but it cannot be used to compare the reactivity of M

and M^+. Uppal studied reaction of Ti^+ with organic halomethanes and organic chlorides in a FT-ICR spectrometer and the dominant reaction was halide abstraction [49]. Fisher studied low energy collisions of Co^+ and Ni^+ with CH_3X (X = Cl, Br, and I) and found MX^+ production in all cases but an energy threshold existed for reaction with CH_3Cl [50]. Fisher also studied reactions of Fe^+ ^6D and Fe^+ ^4F with CH_3X (X = Cl, Br, and I) and found FeX^+ production in all cases. It was also observed that the excited state was the most reactive [51]. Armentrout studied low energy collisions of U^+ with CH_3F, CH_3Cl, CCl_4, and SiF_4 and found UX^+ production in all cases but also the existence of a reaction barrier in the case of SiF_4 [52]. Chowdhury studied thermal reaction of Au^- with organic halides found production of Cl^- and Br^- from CH_3Cl and CH_3Br while reaction with CCl_4 yielded $AuCl_2^-$ [53]. Hu studied photofragmentation of $Mg(C_6H_5OCF_3)^+$ and found that the dominant reaction channel was production of Mg^+ followed by production of MgF^+ [54]. Liu studied photofragmentation of Mg(2-fluoropyridine)$^+$ and found Mg^+ as the dominant fragment ion with MgF^+ being formed in lower abundance than $C_4H_4^+$ [55]. Herman studied flowing afterglow reactions of Ti^+, V^+, Fe^+, Co^+, Ni^+, Cu^+, Zn^+ with CO_2 and found production of MO^+ only for Ti^+ [56].

Summary

Methods that use corrosive and hygroscopic materials exists for generation of salts in the gas phase. In addition less efficient methods exists which abstract electronegative elements from molecular precursors. The ability of an atomic metal ion M^+ to abstract halides depends on IE(M^+) according to the 'IE indicator'. It is unlikely that any reaction barriers exist for halide abstraction by atomic metal monocations.

1.1.4 Background

Here are some observations regarding cross sections and selection rules that may be useful in giving some background on charge exchange, cross sections, and selection rules.

A beam of H^+ produces a beam of predominantly excited H atoms upon collision with cesium atoms [57]. A beam of N_2^+ produces a beam predissociating N_2^* upon collision with Cs atoms [58]. Cross sections have been studied for charge exchange in keV collisions between atomic ions and neutral atoms of the same element. Cross sections are in the order of 100 $Å^2$ for alkali metals and 10 $Å^2$ for noble gases [24]. These trends can all be rationalised by the classical over barrier (COB) model which usually gives a good description for monocations colliding with neutral target gases.

Diatomic molecular ions N_2^+ and O_2^+ underwent resonant neutralisation to excited states upon high energy collision with Cs atoms. Electronic rearrangement of the ionic core is observed for N_2^+ with small HOMO-LUMO gap but not in O_2^+ with large HOMO-LUMO gap [58]. An ensemble of N_2^+ in various states was collided with N_2, O_2, NO, and Ar and the resulting translation energy spectrum was recorded. Inelastic and superelastic processes of N_2^+ dominated. The only transition observed in collision gases was the $^1\Delta_g \leftarrow {}^3\Sigma_g^-$ transition in O_2 with all other target gases being inert. This demonstrates that transitions only occur in cases where the energy difference between states is low and that transitions are not limited to electric dipole transitions [59].

Ionisation of CS_2 was performed by high energy collisions with six different projectile cations and some states of CS_2^+ were formed that could not be formed by electron

impact or photo ionisation according to selection rules. It was concluded that resonant electron transfer is not necessarily dominant for two electron processes [60]. It is observed that geometries are fixed and spins are conserved in high energy collisions [24].

1.2 Reaction energies

The ionisation energy (IE) of an atom is the energy required to remove an electron from it while the electron affinity of an atom (EA) is the energy released by addition of an electron to it. Ionisation energies are always positive while electron affinities are sometimes negative. Ionisation energies and electron affinities also exists for molecules although the situation is complicated by the fact that molecules change equilibrium geometry when they lose or gain electrons. For these processes the reactant is always in its equilibrium geometry. The product is in the equilibrium geometry of the reactant for vertical processes while for adiabatic processes the product is in its own equilibrium geometry. A reverse process of ionisation is called recombination where a positively charges species gains an electron. The recombination energy (RE) is the energy gained by addition of an electron to a positively charged species where the reactant is in its own equilibrium geometry. The vertical RE is an important quantity in Chapter 4.

The energy required to dissociate a diatomic species is called the dissociation energy of the species. For polyatomic species the process requires specification of the bond to be broken forming fragments in their equilibrium geometries. The energy required to dissociate a specific bond in molecule AB is called the bond dissociation energy (BDE) of A–B.

1.3 Clusters

It is necessary to have a basic understanding of cluster types and of how clusters are generated. This section will present some types of clusters, their properties, and methods for generation of gas-phase clusters.

There are several types of clusters characterised by their different constituents and their different types of internal interactions described in Table 1.1.

Cluster	**Examples**	**Localised bonds**	**Delocalised bonds**	**Dominant attraction**	**Binding energy**[1]
Molecules (Localised)	I_2, NH_3, C_2F_4, CO, SF_6, H_2	Yes	No	Covalent	1.8 eV 11 eV
Molecules (Delocalised)	B_2H_6, C_6H_6, C_{60}, C_{50}, C_{70}	Yes	Yes	Covalent	1.9 eV 9.8 eV
Rare gasses	Ne_n, Ar_n, He_n, Rn_n, Xe_n, Kr_n	No	No	Dispersive	2 meV 18 meV
Metals (Closed Shell)	Hg_n, Cd_n, Zn_n, Be_n, Mg_n, Ca_n	No	No	Dispersive	83 meV 0.6 eV
Metals (Open Shell)	Cs_n, Al_n, Mn_n, Mo_n, Cu_n, Pb_n	No	Yes	Metallic	0.5 eV 4.2 eV
Metaclusters[2]	**Monomer examples**	**Orbital perturbation**	**Unidirectional bonds**	**Dominant attraction**	**Binding energy**
Non-polar molecules	N_2, CO, CCl_4, $C_2(CN)_4$, C_3H_8	No	No	Dispersive	7 meV 43 meV
Protic molecules	HF, C_2H_5OH, HCO_2H, NH_3	Yes	Yes	Hydrogen bonding	0.2 eV 0.7 eV
Salts	NaCl, AlF_3, NaF, K_2O	Yes	No	Ionic	2.0 eV 2.8 eV

Table 1.1 Types of gas-phase clusters. It is shown whether a cluster contains localised or delocalised bonds. It is shown if formation of metaclusters changes the orbitals of the monomer and if they move in a single direction. Values needed for calculation of binding energies are taken from [61] and for C_{60} from [62].

---

[1] Values were calculated as follows:
Dissociation energies of I_2, CO, Hg_2, Be_2, Cs_2, and Mo_2 are converted from kJ/mol.
Dissociation was $B_2H_6 \rightarrow 2\ BH_3$ and it was calculated using MP2 with G3LARGE.
Dissociation $C_{60} \rightarrow C_{58} + C_2$ was observed. Less perfect fullerenes are more fragile.
Values for Ne_2, Rn_2, N_2, and $(C_2(CN)_4)_2$ are calculated using kT of their boiling points.
Values for $(HF)_2$, $(HCO_2H)_2$, $(NaCl)_2$, and $(NaF)_2$ are calculated using MP2 with G3LARGE.
[2] 'clusters of clusters'

The types of clusters listed in Table 1.1 were pure types. There can also be mixed types where more than one class of constituent is present. For instance some clusters used experimentally in this work contain both molecules and noble gas atoms.

Clusters can be made by supersonic expansion, sputtering, gas-aggregation, or by techniques which thermally evaporate material from a surface [63]. The method used for generation of clusters in this work was supersonic expansion and a detailed description of the process is given in the experimental section.

1.4 Barriers

Transient negative ions are sometimes called anion resonances and they are of importance to chapter 3 regarding charge stripping. The presence of anion resonances requires some sort of barrier to detachment. In this section some types of barriers are presented.

1.4.1 Centrifugal barriers

Wavefunction overlap formulation

Centrifugal barriers arise when there is a difference between the angular momentum of the initial state and the final state in an electron detachment process because that difference must be carried away by the detaching electron. The process is depicted in Figure 1.3.

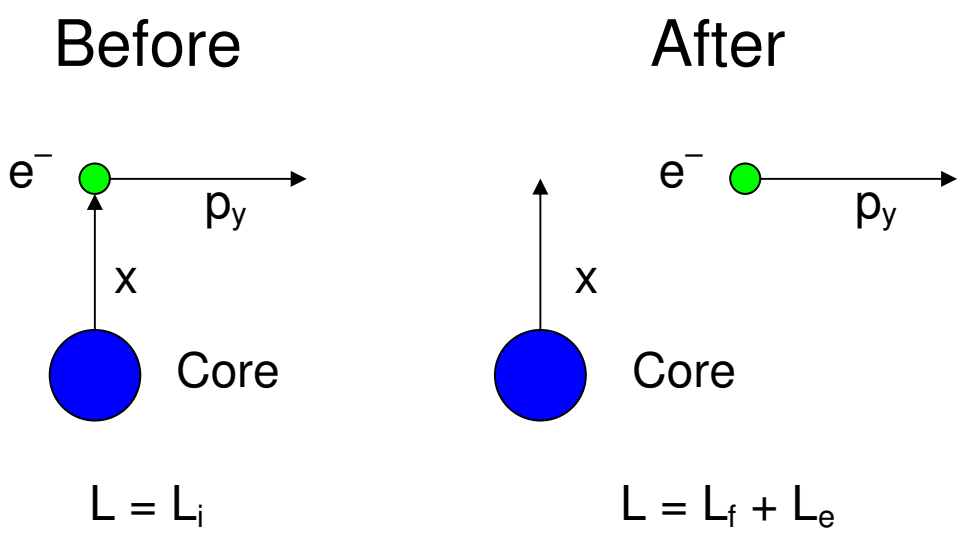

Figure 1.3 Centrifugal barrier. The impact parameter of a detaching electron is called x and its momentum p_y. Angular momenta L_i, L_f, and L_e are initial, final, and electron respectively. L_e is xp_y so the wavefunction must have non-vanishing amplitude at x in order to detach.

In order for the angular momentum of the detaching electron to be non-zero the product of the impact parameter and the momentum of the detaching electron must be non-zero which means the impact parameter must be large if the momentum is small. The momentum is given by the mass of the electron and the kinetic energy of the electron which again is given by the energy difference of the initial and final states. If the impact parameter must be large this poses a problem because the wavefunction of the anion is of finite size so any coupling between the free and the bound states will be small.

Potential formulation

The effective centrifugal barrier is sometimes described by a centrifugal potential given in Equation 1.1.

$$\frac{\hbar l(l+1)}{m_e r^2} \tag{1.1}$$

The centrifugal potential is used in text book to justify the form of the hydrogen p wavefunction [64] and it has been used to calculate potential energy curves relating to photoionisation of heavy atoms [65]. Although the potential formulation gives no understanding of what causes the barrier it has the advantages of allowing easy visualisation as well as easy application in computational programs.

Angular momentum

Atomic orbitals have well defined l quantum numbers but molecular orbitals do not. Atomic p orbitals are odd functions with respect to a mirror plane. Linear molecules have an analogue to atomic p orbitals as the angular momenta projected onto the molecular axes are quantised. Only p orbitals and orbitals with higher orbital momenta contribute to π orbitals calculated by computer programs. All atoms lie in a plane in linear molecules. Perhaps this idea can be extended to molecules which are neither linear nor planar. An atom in such molecules will have an orbital with zero s orbital contribution from it if it and its nearest neigbours lie in a plane. The LUMO orbitals of such molecules typically have atoms which does not contribute s orbital components.

Quantum numbers n and l of basis set functions on atoms are defined by the number of nodes and radial nodes respectively. When atoms are combined into compounds the picture becomes more complicated as for instance orbitals of A_{1u} symmetry in CO_2 have both p orbital contributions from all the atoms and s orbital contributions from the O atoms. It may then not be possible to provide a unique solution to the question

of how the orbitals in CO_2 are partitioned between s and p orbitals on the different atoms. Mulliken populations and natural bond orbitals are two different methods to find atomic partial orbital contributions. The solutions found by the two methods are usually different – hence the solutions are not unique.

It is assumed that partial orbital components are meaningful quantities also for σ-bonds in diatomic species and two observations give hints that they are. Upon dissociation l gradually reemerges as a quantum number for the isolated atoms. The lifetime of vibrationally excited LiH^- is much shorter than that of OH^- [66]. This could be due to s orbital detachment of the electron from LiH^- although energy considerations also play their part. It is likely that the concept of partial orbital components are meaningful for polyatomic species if it is for diatomic species.

1.4.2 Coulomb barriers

Coulomb barriers arise when a long range repulsive Coulomb potential is overcome by a short range attractive potential at short distances. The particle will then be bound either kinetically or thermodynamically at short ranges but unbound at long range.

Coulomb barriers for electron detachment was first observed by X. B. Wang and L. S. Wang [67]. It is observed for diatomic [68] and polyatomic systems. Coulomb barriers for dissociation is observed for diatomic and polyatomic systems.

1.4.3 Shape resonances

Ground states of anions formed by electron attachment to species with negative electron affinity is called shape resonances. Barriers must be present in such systems because they have non-zero lifetimes. The barriers in shape resonances may be centrifugal barriers as in N_2^- but there may also be other types such as in symmetrically vibrationally excited SF_6^-. Shape resonances are indirectly observed in hydrogen plasmas due to formation of H^- anions from transient H_2^- precursors. Shape resonances are important to this work as they are the ground state of transient anions formed in collisions.

1.5 Interaction potentials

Collisional recombination

Large part of this work regard collisions between doubly charged projectiles and neutral target gases. The potential energy for two charged atoms can be approximated by a Coulomb potential as described in Equation 1.2 while the potential energy for a doubly charged atom interacting with a neutral atom can be described by a polarisation potential as given in Equation 1.3.

$$V_c = \frac{q_1 q_2}{4\pi\varepsilon_0 r} \tag{1.2}$$

$$V_p = -\frac{\alpha |q|}{4\pi\varepsilon_0 r^4} \tag{1.3}$$

In the above equations the distance between atoms is r, atomic polarisability is α, and charge is q. Subscripts are used in the presence of more than one charge. The polarisation potential is always attractive. These potentials are most accurate for large internuclear separations where the field strength arising from the overall charge of one atom is approximately constant over the entire wavefunction of the other atom.

The potentials are also being used to describe molecular collisions but this is a severe simplification as no meaningful internuclear separation exists between two molecules. The polarisability of diatomic target gases is anisotropic having much larger magnitude along the molecular axis than perpendicular to it. Furthermore closed shell molecules often attains metallic conductance upon ionisation due to the low HOMO-LUMO gap of the resulting ion. Thus the effect of polarisation significantly alters the resulting Coulomb potential.

Dication stability

Interaction potentials may also be used to predict stability of dicationic complexes. A dicationic complex consisting of a metal atom M and a ligand noble gas atom L is definitely stable if IE(L) exceeds IE(M^+). Such complexes are likely to dissociate into M^{2+} and L upon CID. The potential energy curve approximated by electrostatic polarisation has no minimum but a curve with a minimum can be calculated quantum mechanically. The features of the resulting potential energy curve are then described by a Morse potential. If the energy of separated fragments M^+ and L^+ is higher that of combined ML^{2+} then the complex is stable. The complex may be kinetically stable if the energy of M^+ and L^+ is lower than that of ML^{2+} but the Coulomb potential crosses the calculated Morse potential at a distance where the nuclear wavefunction has

negligible magnitude. Complexes where IE(M^+) exceeds IE(L) are likely to dissociate into M^+ and L^+ upon CID. Finally the complex is unstable if the Coulomb potential crosses the Morse potential near the minimum of the Morse potential. These trends are also valid when L is a molecule so ML^{2+} may be kinetically stable even if its energy is higher than that of separated fragments M^+ and L^+.

1.6 Landau Zener theory

The Landau-Zener (LZ) model [69, 70] describes the probability *P* of nonradiative transitions between two electronic states during atomic collisions. *P* is given in terms of the probability δ that a single passage through an avoided crossing between two electronic states of the same symmetry results in transition. P and δ are described by Equations 1.4 and 1.5.

$$P = 2\delta(1-\delta) \tag{1.4}$$

$$\delta = \exp\left(\frac{-\pi|H_{12}|^2}{2\hbar|V_1 - V_2|v_b}\right) \tag{1.5}$$

Where H_{12} is the coupling matrix element between the two states, V_1 and V_2 refers to energy potentials of the two states, and v_b is the radial velocity between the two atoms. The probabilities of energy demanding reactions increase and those of energy releasing reactions decrease with increasing collisional velocity as can be seen from Equation 1.5. The electrostatic potentials can often be approximated by those given by Equations 1.2 and 1.3. The coupling matrix element $|H_{12}|^2$ can be evaluated by

semiempirical methods and charge exchange cross sections can thus in principle be calculated. It will here be used as a result that the single passage probability δ is small for small crossing radii corresponding to strongly adiabatic avoided crossings. In contrast δ is large for large curve crossing distances with small orbital overlap leading to diabatic transitions. Both these situations lead to small probability P of collisional transfer so reaction is only facile within a window where the curve crossing distance r_c is in the range 2-6 Å. For charge recombination the crossing of potential energy curves is shown in Figure 1.2. Insufficiently energy releasing reactions ($r_c > 6$ Å, $\Delta U > -2.5$ eV) rarely occur. Instead the reactants fragment so they either form smaller dications or undergo Coulomb explosion. Moderately energy releasing electron transfers (2 Å $< r_c <$ 6 Å, -2.5 eV $> \Delta U >$ -7 eV) result in intact products but strongly energy releasing electron transfers ($r_c <$ 2 Å, $\Delta U <$ -7 eV) often lead to dissociation due to formation of dissociative excited states. Curve crossings is also shown for charge stripping in Figure 1.1.

LZ theory give predictions about the translational kinetic energy of projectiles upon reaction as electron transfer is predicted to be strongly localised at the curve crossing. LZ theory was developed to describe atomic collisions but it is frequently employed to describe molecular collisions as well.

1.7 References

1. P. O. Danis, R. Feng, and F. W. McLafferty, *Reionization Agents for Neutralization-Reionization Mass Spectrometry.* Anal. Chem., 1986. **58**: p. 355-358.
2. J. E. Land and W. Raith, *Fine structure of O_2^- measured by electron time-of-flight spectroscopy.* Phys. Rev. Lett., 1973. **30**: p. 193.
3. X. B. Wang, C. F. Ding, and L. S. Wang, *High resolution photoelectron spectroscopy of C_{60}^-* J Chem. Phys., 1999. **110**: p. 8217.
4. P. Hvelplund, et al., *Electron capture and loss by protonated peptides and proteins in collisions with C_{60} and Na.* Eur. Phys. J. D, 2003. **22**: p. 75.
5. D. Schröder, S. Bärsch, and H. Schwarz, *Redox properties of charged and neutral iron chlorides $FeCl_m^n$ (m = 1–3; n = −1, 0, +1, and +2).* Int. J. Mass Spectrom., 1999. **192**: p. 125.
6. F. M. Rourke, et al., *Charge permutation reactions and dissociation of molecular ions by impact with neutral molecules.* J. Chem. Phys., 1959. **31**: p. 193.
7. N. Kashihira, F. Schmidt-Bleek, and S. Datz, *Ionizing collisions of fast alkali atoms with Cl_2, Br_2, and O_2.* J. Chem. Phys., 1974. **61**: p. 160.
8. R. N. Compton, P. W. Reinhardt, and C. D. Cooper, *Collisional ion pair formation: Electron affinities for CH_3NO_2, CF_3I, and CF_3Br.* J. Chem. Phys., 1978. **68**: p. 4360.
9. R. N. Compton, P. W. Reinhardt, and C. D. Cooper, *Collisional ionization of Na, K, and Cs by CO_2, COS, and CS_2: Molecular electron affinities.* J. Chem. Phys., 1975. **63**: p. 3821.
10. A. P. M. Baede and J. Los, *Total cross sections for charge transfer and production of free eletrons by collisions between alkali atoms and some molecules.* Phys., 1971. **52**: p. 422.
11. R. J. Warmack, J. A. D. Stockdale, and H. C. Schweinler, *Collisional ionization of atomic cesium and potassium by CH3CN.* J. Chem. Phys., 1980. **72**: p. 11.
12. R. N. Compton and P. W. Reinhardt, *Collisional ionization between fast alkali atoms and selected hexafluoride molecules.* J. Chem. Phys., 1978. **68**: p. 2023.
13. R. N. Compton and P. W. Reinhardt, *Collisional ionization between fast alkali atoms and hexafluorobenzene.* Chem. Phys. Lett., 1982. **91**: p. 268.
14. C. D. Cooper and W. T. Naff, *Negative ion properties of p-benzoquinone: Electron affinity and compound states.* J. Chem. Phys., 1975. **63**: p. 2752-2757.
15. D. Scott, M.S.H., R. L. Champion, and L. D. Doverspike, *Alkali-negative-ion-molecule collisions.* Phys. Rev. A, 1986. **33**: p. 170.
16. A. B. Nielsen, P. Hvelplund, and S. B. Nielsen, *Ruthenium diimine complexes in unusual charge states formed in collisional electron transfer.* Int. J Mass Spectrom., 2004. **232**(1): p. 79-82.
17. P. R. Brooks, P. W. Harland, and C. E. Redden, *Electron Transfer from Sodium to Oriented Nitromethane, CH_3NO_2: Probing the Spatial Extent of Unoccupied Orbitals.* J. Am. Chem. Soc., 2006. **128**: p. 4773.
18. P. R. Brooks, et al., *Steric Effects in Electron Transfer from Potassium to pi-Bonded Oriented Molecules CH_3CN, CH_3NC, and CCl_3CN.* J. Am. Chem. Soc., 2007. **129**: p. 15572.
19. B. Liu, et al., *Electron Attachment to "Naked" and Microsolvated Nucleotide Anions: Detection of Long-Lived Dianions.* ChemPhysChem, 2003. **4**: p. 1341.
20. A. B. Nielsen, et al., *Coulomb Explosion upon Electron Attachment to a Four-Coordinate Monoanionic Metal Complex.* J Am. Chem. Soc., 2003. **125**: p. 9592-9593.
21. S. B. Nielsen and M. B. Nielsen, *Experimental evidence for the 7,7,8,8-tetracyano-p-quinodimethane dianion in vacuo.* J Chem. Phys., 2003. **119**: p. 10069.
22. B. Liu, et al., *Formation of C_{60}^{2-} Dianions in Collisions between C_{60}^- and Na Atoms.* Phys. Rev. Lett., 2004. **92**: p. 168301.
23. D. Mathur, *A reaction window in double charge-transfer mass spectrometry.* Int. J. Mass Spectrom. Ion Proc., 1988. **83**: p. 203.
24. S. Hayakawa, *Charge inversion mass spectrometry: Dissociation of resonantly neutralized molecules.* J. Mass Spectrom., 2004. **39**: p. 111.
25. Z. Herman, et al., *Non-dissociative single-electron capture by CO^{2+} from rare gases.* Chem. Phys. Lett., 1987. **141**: p. 433.

26. R. E. March, J. G. Macmillan, and A. B. Young, *Unimolecular and collision-induced processes of ethyne and ethyne-d_1 dications and charge separation of dications derived from butadiene.* Int. J. Mass Spectrom. Ion Proc., 1988. **82**: p. 177.
27. C.J. Reid, J. A. Ballantine, and F. M. Harris, *Dissociative and non-dissociative single-electron capture by CO_2^{2+} and OCS^{2+} from rare-gas atoms.* Int. J. Mass Spectrom. Ion Proc., 1989. **93**: p. 23.
28. K. Nagesha, V.R. Marathe, and D. Mathur, *An experimental and theoretical study of SF^{q+} (q = 1-3) ions.* Chem. Phys., 1991. **154**: p. 125.
29. H. R. Koslowski, et al., *Collisions of doubly charged nitrogen molecules with rare gas atoms.* J. Phys. B, 1991. **24**: p. 5023.
30. B. Leyh and A. Hoxha, *Reaction window in the single-electron capture by ammonia dications.* Chem. Phys., 1995. **192**: p. 65.
31. B. Leyh and D. Hautot, *Mechanisms of single-electron capture by the dichlorocarbene dication.* J. Am. Soc. Mass Spectrom., 1996. **7**: p. 266.
32. D. Schroder, et al., *Does ionized diacetylene have a positive proton affinity?* Int. J. Mass Spectrom., 2003. **230**: p. 113.
33. B. J. Duncombe, et al., *Gas-phase experiments on the chemistry and coordination of Zn(II) by aprotic solvent molecules.* Can. J. Chem., 2005. **83**: p. 1994.
34. J.A. Stone and D. Vukomanovic, *Collisional dissociation studies of $Cu^{2+}(H_2O)_n$ using electrospray ionization mass spectrometry.* Int. J. Mass Spectrom., 1999. **185/186/187**: p. 227.
35. C. Seto and J. A. Stone, *The reactions of $Cu^{2+}(CH_3CN)_n$ (n = 2-4) and $Cu^{2+}(CH_3CN)_3(H_2O)$ at low collision energy with neutral molecules in a triple sector quadrupole instrument.* Int. J. Mass Spectrom. Ion Proc., 1998. **175**: p. 263.
36. S. D. Price, M. Manning, and S. R. Leone, *Bond-forming reactions of gas-phase molecular dications.* J. Am. Chem. Soc., 1994. **116**: p. 8673.
37. S. A. Rogers, S. D. Price, and S. R. Leone, *Charge transfer and collision-induced dissociation reactions of CO^{++} with the rare gases at E_{lab} = 49 eV.* J. Chem. Phys., 1992. **98**: p. 280.
38. M. Manning, S. D. Price, and S. R. Leone, *Charge-transfer and collision-induced dissociation reactions of CF^{2+} and CF_2^{2+} with the rare-gases at a laboratory collision energy of 49 eV* J Chem. Phys., 1993. **99**: p. 8695.
39. D. F. Shriver and P. W. Atkins, *Inorganic Chemistry*. 3rd ed. 2001: Oxford University Press.
40. H. L. Schläfer and G. Gliemann, *Basic Principles of Ligand Field Theory*. 1969, New York: Wiley Interscience.
41. F. Hund, *Zur Deutung einiger Erscheinungen in den Molekelspektren.* Z. Phys., 1926. **36**: p. 657.
42. R. S. Mulliken, *The Assignment of Quantum Numbers for Electrons in Molecules. I.* Phys. Rev., 1927. **32**: p. 186.
43. R. S. Mulliken and C. A. Rieke, *Molecular electronic spectra, dispersion and polarization: The theoretical interpretation and computation of oscillator strengths and intensities.* Rep. Progress Phys., 1941. **8**: p. 231.
44. *Wikipedia*. [cited; Available from: http://en.wikipedia.org.
45. N. R. Walker and M. C. L. Gerry, *Microwave spectra, geometries, and hyperfine constants of OCCuX (X = F, Cl, Br).* Inorg. Chem., 2001. **40**: p. 6158.
46. N. R. Walker and M. C. L. Gerry, *Microwave spectra, geometries, and hyperfine constants of OCAgX (X = F, Cl, Br).* Inorg. Chem., 2002. **41**: p. 1236.
47. X. Zhao, G. K. Koyanagi, and D. K. Bohme, *Reactions of Methyl Fluoride with Atomic Transition-Metal and Main-Group Cations: Gas-Phase Room-Temperature Kinetics and Periodicities in Reactivity.* J. Phys. Chem. A, 2006. **110**: p. 10607.
48. H. H. Cornehl, G. Hornung, and H. Schwarz, *Gas-Phase Reactivity of Lanthanide Cations with Fluorocarbons: C−F versus C−H and C−C Bond Activation.* J. Am. Chem. Soc., 1996. **118**: p. 9960.
49. J. S. Uppal and R. H. Staley, *Gas-phase chemistry of Ti^+ with halomethanes, alkyl chlorides, chloroethylenes, and chlorobenzene* J. Am. Chem. Soc., 1980. **102**: p. 4144.
50. E. R. Fisher, L. S. Sunderlin, and P. B. Armentrout, *Guided Ion Beam Studies of the Reactions of Co^+ and Ni^+ with CH_3X (X = Cl, Br, I). Implications for the Metal Methyl Ion Bond Energies.* J. Phys. Chem., 1989. **93**: p. 7375.
51. E. R. Fisher, R. H. Schultz, and P. B. Armentrout, *Guided Ion Beam Studies of the Reactions of $Fe^+(^6D, ^4F)$ with CH_3X (X = Cl, Br, I).* J. Phys. Chem., 1989. **93**: p. 7382.
52. P. B. Armentrout and J. L. Beauchamp, *Thermochemistry of Uranium Halide Ions: Reactions of U^+ with CH_3F, SiF_4, CH_3Cl and CCl_4.* J. Phys. Chem., 1981. **85**: p. 4103.

53. A. K. Chowdhury and C. L. Wilkins, *Reactions of atomic gold ions with aliphatic and aromatic hydrocarbons and alkyl halides.* J. Am. Chem. Soc., 1987. **109**: p. 5336.
54. Y. Hu, H. Liu, and S. Yang, *Photoinduced reaction in the ion-molecule complex* Mg^+-$C_6H_5OCF_3$. Chem. Phys., 2007. **332**: p. 66.
55. H. Liu, et al., *Unusual Chemistry of the Complex Mg•+(2-Fluoropyridine) Activated by the Photoexcitation of Mg•+*. J. Am. Chem. Soc., 2003. **125**: p. 12351.
56. J. Herman, J. D. Foutch, and G. E. Davico, *Gas-phase reactivity of selected transition metal cations with CO and* CO_2 *and the formation of metal dications using a sputter ion source.* J. Phys. Chem. A, 2007. **111**: p. 2461.
57. B. L. Donnally, et al., *Metastable hydrogen atoms produced in charge exchange.* Phys. Rev. Lett., 1964. **12**: p. 502.
58. A. B. Kamp, et al., N_2^+ $(A\ ^2\Pi_u \leftarrow X\ ^2\Sigma_g^+)$ *excitation in the charge-exchange collision with caesium: two-electron effects at keV energies.* J. Phys. B, 1994. **27**: p. 5037.
59. A. R. Lee, C. S. Enos, and A. G. Brenton, *Collisional excitation of the Meinel and first negative systems of* N_2^+. Int. J. Mass Spectrom. Ion Proc., 1993. **124**: p. 85.
60. C. J. Reid, *Electron-transfer ionization of* CS_2 *into hidden cationic states below 20 eV.* J. Phys. B, 1996. **29**: p. 71.
61. D. R. Lide, *Handbook of Chemistry and Physics*. 85th ed. 2004: CRC Press.
62. S. Tomita, et al., *Dissociation Energy for* C_2 *Loss from Fullerene Cations in a Storage Ring.* Phys. Rev. Lett., 2001. **87**: p. 073401.
63. R. L. Johnston, *Atomic and molecular clusters*. 2002, New York: Taylor & Francis.
64. S. Gasiorowicz, *Quantum Physics*. 1996: John Wiley & Sons, Inc.
65. S. T. Manson and J. W. Cooper, *Photo-Ionisation in the Soft X-Ray Range: Z Dependence in a Central-Potential Model.* Phys. Rev., 1968. **165**: p. 126.
66. P. K. Acharya, R. A. Kendall, and J. Simons, *Vibration-induced electron detachment in molecular anions.* J. Am. Chem. Soc., 1984. **106**: p. 3402.
67. X. B. Wang and L. S. Wang, *Observation of negative electron-binding energy in a molecule.* Nature, 1999. **400**: p. 245.
68. L. H. Andersen, et al., *Resonant and nonresonant electron impact detachment of* CN^- *and* BO^-. J. Chem. Phys., 2001. **115**: p. 3566.
69. L. Landau, *Zur Theorie der Energieübertragung II.* Phys. Sov. Union, 1932. **2**: p. 46.
70. C. Zener, *Non-adiabatic Crossing of Energy Levels.* Proc. Royal Soc. London, Series A, 1932. **137**: p. 692.

Chapter 2
Experimental

2.1 Introduction

This chapter gives a description of the experimental apparatus used in this work as well as the scanning techniques used for obtaining spectra. A description of the program package Q-Chem used for quantum chemical calculations is also given.

2.2 Apparatus

The mass spectrometer presented in the thesis consists of three sections, the cluster generation, ionisation, and scanning section. The cluster generation section is a home-built device specifically made to make it possible to make clusters including metal containing clusters. The experiments in this work were performed on a modified VG ZAB-E mass spectrometer which is depicted in Figure 2.1.

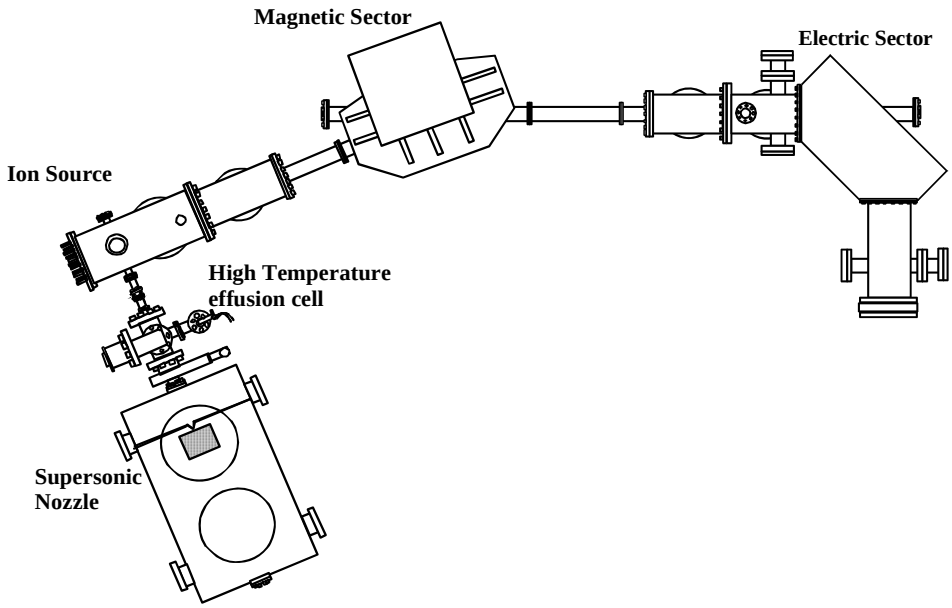

Figure 2.1 Schematic drawing of the VG ZAB-E mass spectrometer [1].

The mass spectrometer consists of parts for gas inlet, cluster generation, pick-up of involatile dopants, and ionisation of clusters or molecules. It further consists of parts for magnetic deflection, collision induced dissociation, electric deflection, and detection of ions. Each of these parts will be described in this chapter.

2.2.1 Gas-inlet system

The clusters are formed during a supersonic expansion of a solvent/argon mixture. Solvents are in the following denoted as gases or liquids depending on their state at room temperature and atmospheric pressure. Gases intended for clustering were bought as a 1% by volume mixture in argon. Mixtures with higher concentrations of the non-argon component were found to cluster poorly. In order to get liquids into the gas phase they were poured in a solvent reservoir which is depicted in Figure 2.2.

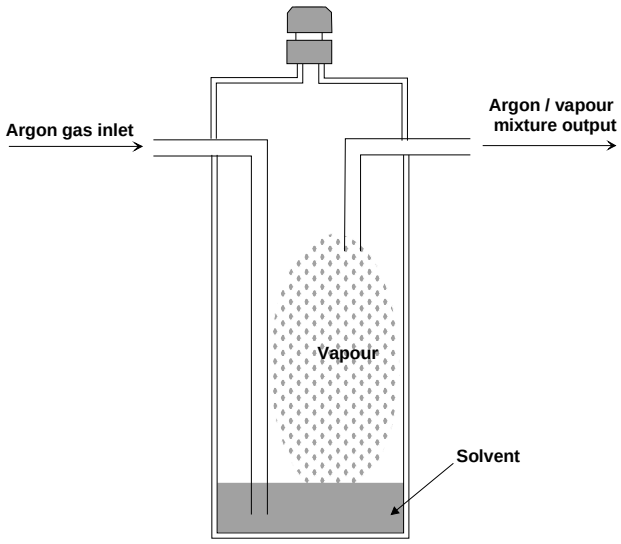

Figure 2.2 Schematic drawing of solvent reservoir [2].

Argon enters through a swagelok^{TM} tube and bubbles through the solvent causing a solvent/argon mixture to leave the reservoir through the exit tube heading for the stagnation chamber. A third tube is at the top of the reservoir has two purposes which are to be able to get solvent into the reservoir and to be able to vent the pressure inside the reservoir down to atmospheric pressure after use. A typical pressure of argon in the reservoir is 4 bars during operation of the mass spectrometer. The partial pressure of liquids at room temperature is usually too high for optimum clustering conditions so it is necessary to submerge the reservoir in an ice bath during operation.

2.2.2 Cluster generation region

The solvent/argon mixture is expanded in the cluster generation region from a high pressure region in the stagnation chamber into a low pressure region in the expansion chamber. The expansion and collimation chambers are depicted in Figure 2.3.

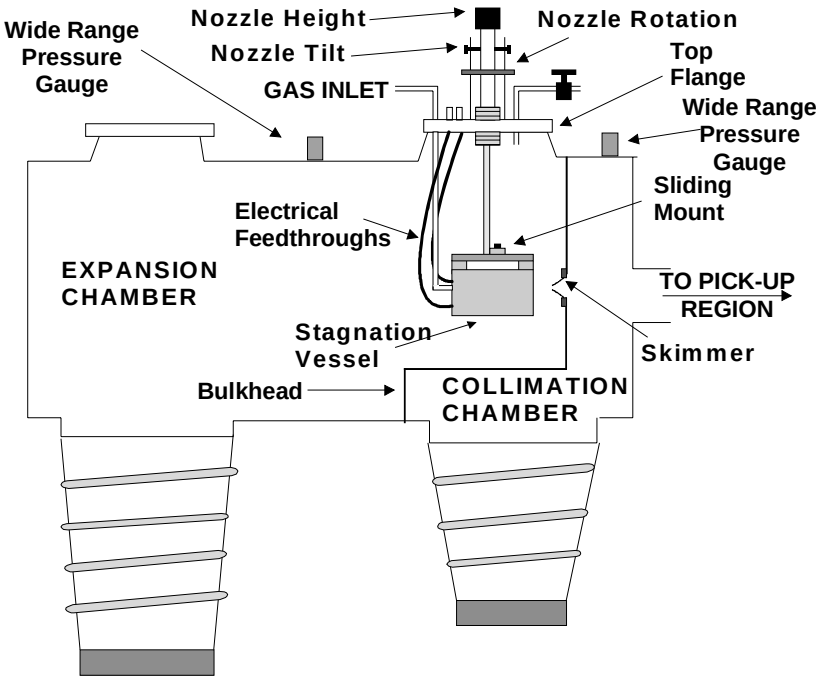

Figure 2.3 Side view of expansion and collimation chambers [1].

The cluster generation region consists of three chambers which are the stagnation chamber, the expansion chamber, and the collimation chamber. The stagnation chamber contains a nozzle which mechanically controls the gas flow into the expansion chamber. A pulse generator sends an electrical signal driving the nozzle to open several times per second so the nozzle is said to be pulsed. The expansion chamber and the collimation chamber divided by a separation wall between them and the only gas flow between them is through a skimmer. The skimmer is 1 mm in diameter in its narrowest point and 25 mm long. It has an internal cone angle of 25° and an external of 30°. The skimmer is placed closer to nozzle than the position which would otherwise be the mach disk so the clusters formed can survive. The expansion and collimation chambers are both a part of the same cylindrical external housing which is approximately 42 cm in inside diameter. The distance from the separation wall to the exterior wall is approximately 110 cm for the expansion chamber 10 cm

for the collimation chamber. In order to keep the pressure below 10^{-4} mbar during operation the expansion chamber it is pumped by an 8000 l/s diffusion pump backed by a 250 l/s booster pump further backed by a 40 l/s rotary pump. The collimation chamber pumped by a 2000 l/s diffusion pump backed by a 40 l/s rotary pump is kept below $2x10^{-6}$ mbar during operation. The mounting of the stagnation chamber makes it possible to align the cluster beam so it passes from the expansion chamber all the way to the ion source because its position and alignment can be adjusted without the need to vent the chamber. The stagnation chamber can be rotated sideways, raised or lowered, and moved closer to or further from the skimmer. The optimum distance between the nozzle in the stagnation chamber and the entrance of the skimmer was close to 30 mm.

2.2.3 Stagnation chamber

The part where clusters are generated is called the stagnation chamber and it is depicted in Figure 2.4.

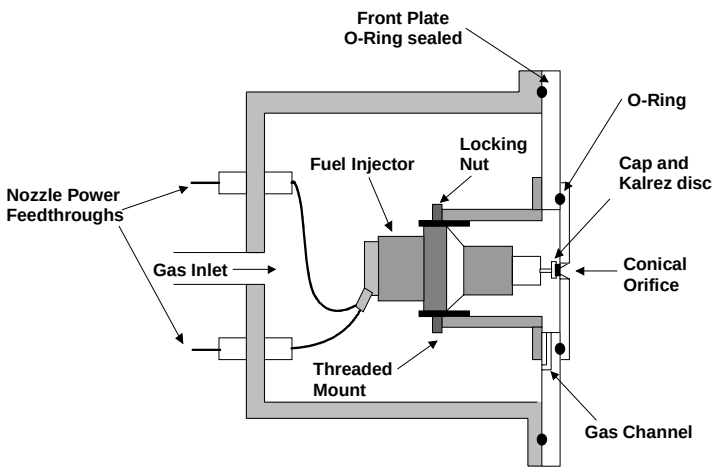

Figure 2.4 Schematic drawing of stagnation chamber [1].

The stagnation chamber has approximate volume of 0.85 l. An argon/solvent mixture enters the stagnation chamber through a gas inlet. A pulsed nozzle made of a fuel injector valve designed for a combustion engine is the moving part of the stagnation chamber. A small rod with a diameter of approximately 1 mm is the moving part of the nozzle and it is welded on to a 3 mm radius metal disk which has a piece of Kalrez^{TM} rubber glued on to it. When the nozzle is closed the rubber makes a gas tight seal with a 0.2 mm diameter conical orifice where gas would otherwise exit. It is through this orifice the supersonic expansion [3-7] takes place. The pinhole is closed when not in operation and during most of the operation cycle. The frequency of the pulses driving the nozzle is controlled by a pulse generator and usually in the range 10-15 Hz. The pulsed nature of the supersonic expansion enables the diffusion pumps to work when the nozzle is closed and this drastically reduces the size of pumps needed to preserve large clusters. It also makes it possible to use phase sensitive data collection by a lock-in amplifier which is an electrical device that amplifies signals of frequencies of interest and filters out other frequencies.

2.2.4 Supersonic expansion

In a supersonic expansion [3-7] gas flows from a high pressure area through a small pinhole into low pressure area. It is necessary to understand the difference between hydrodynamic flow and effusive for a proper description of supersonic expansions. One quantity the mean free path of a gas atom λ is vital for the distinction between hydrodynamic and effusive flow.

$$\lambda = \frac{RT_0}{\sqrt{2}\pi \cdot d^2 N_A P_0} \tag{2.1}$$

A flow of gas is said to be effusive if the mean free path is much longer than the diameter of the orifice (λ >> D). In effusive flows collisions rarely occur so redistribution of internal degrees of freedom to translational kinetic energy is practically nonexistent. In contrast if the diameter of the orifice is much larger than the mean free path (λ << D) then the flow is called hydrodynamic and redistribution occurs very efficiently. In an ideal effusive flow the length of the orifice is negligible. The gas flow far from the orifice is then proportional to the area of the projection of the orifice in the direction of the flow. Thus the flow is proportional to cosine of the angle between the axis and the direction of interest. In a hydrodynamic flow the length of the orifice is often not negligible so the gas is pushed more in the forward direction. In fact the orifice is often followed by a cone in order to convert radial flow into axial flow. In an effusive flow the lighter components of a gas mixture will effuse quicker than the heavier as described by Equation 2.2.

$$\frac{r_1}{r_2} = \frac{M_2}{M_1} \tag{2.2}$$

In contrast both gases flow at the same rate in a hydrodynamic flow. Hydrodynamic flows can be categorised as subsonic or supersonic. In order to make that distinction a variable γ must be introduced which depends on the specific heat capacity of a gas at constant pressure C_p and constant volume C_v.

$$\gamma = \frac{C_p}{C_v} \tag{2.3}$$

The quantity γ defines another useful quantity *G*.

$$G = \left(\frac{\gamma + 1}{2}\right)^{\frac{\gamma}{\gamma - 1}} \tag{2.4}$$

The expansion is supersonic if the ratio $P_0/P_b > G$ where P_b refers to the background pressure. The term supersonic means that the flow is higher than the local speed of sound and one way of saying it is that the mach number *M* is larger than 1.

$$M = \frac{u}{c} \tag{2.5}$$

The term *u* denotes the mean flow velocity of the beam while *c* is the local speed of sound. The Mach number can be expressed as a function of the distance *X* downstream from the orifice.

$$M = A\left(\frac{X}{D}\right)^{\gamma - 1} \tag{2.6}$$

The quantity *A* depends on γ and it is 3.26 for a monoatomic gas. From this expression the local translational temperature *T*(*X*) can be calculated at a distance downstream. It should be noted though that the translational temperature mentioned is

in a moving coordinate system having zero flow at X rather than that having origo at the orifice.

$$T(X) = \frac{T_0}{1 + \frac{\gamma - 1}{2} A^2 \left(\frac{X}{D} \right)^{2\gamma - 2}} \tag{2.7}$$

At some point collisions seizes to occur due to low number density so Equation 2.7 is no longer valid. Also if the atoms begin to condense the gas will deviate from an ideal gas and this too will invalidate Equation 2.7. The terminal velocity of the beam is dependent on the molecular weight W.

$$v_{term} = \sqrt{\frac{2R}{W}} \left(\frac{\gamma}{\gamma - 1} \right) T_0 \tag{2.8}$$

Collisional cooling is increasingly more efficient in the order vibrational < rotational < translational. A typical temperature distribution upon expansion of a molecular gas from room temperature and atmospheric pressure is given below.

$$T_{trans} (\approx 0.5K) < T_{rot} (\approx 5K) < T_{vib} (\approx 50K) < T_0 \tag{2.9}$$

In practice it is observed that expansion of pure solvent vapour at standard temperature and pressure does not lead to clustering. Instead a small fraction of solvent seeded in argon gives efficient clustering. The clusters both contain solvent and argon so the solvents are at rest both rotationally and vibrationally as the argon atoms would otherwise quickly evaporate. The final equation necessary for

description of supersonic expansions is the location of the mach disc X_m where successive collisions with the background gas heats up the beam making it subsonic.

$$X_m = 0.67D\sqrt{\frac{P_0}{P_b}} \tag{2.10}$$

There are different regions in a supersonic expansion characterised by their Mach number and Figure 2.5 shows a schematic of a steady state supersonic expansion.

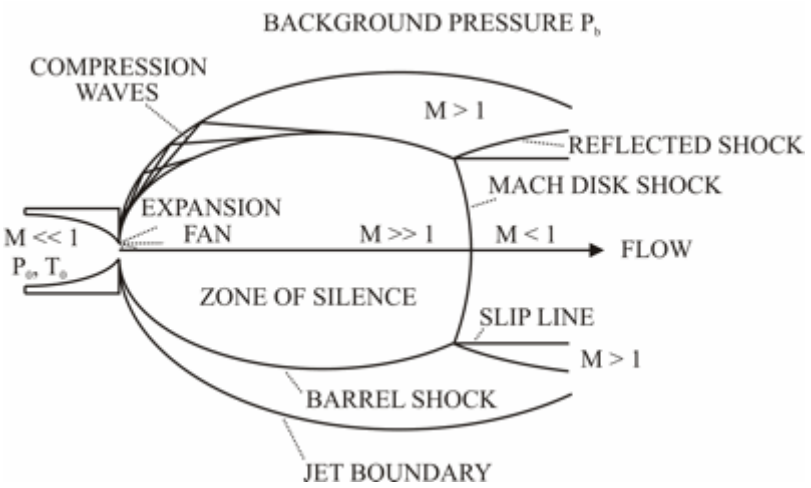

Figure 2.5 Steady state supersonic expansion.

In the zone of silence the flow does not collide with background gas and is not affected by the background pressure. In contrast outside the jet boundary there is little flow so these two situations adapt between the barrel shock and the jet boundary by shock waves in a thin non-adiabatic area of large density, pressure, temperature, and velocity gradients.

2.2.5 High temperature oven

It may be desired to add an involatile component to clusters generated by the expansion. A high temperature effusion cell is used for achieving this goal and it is depicted in Figure 2.6.

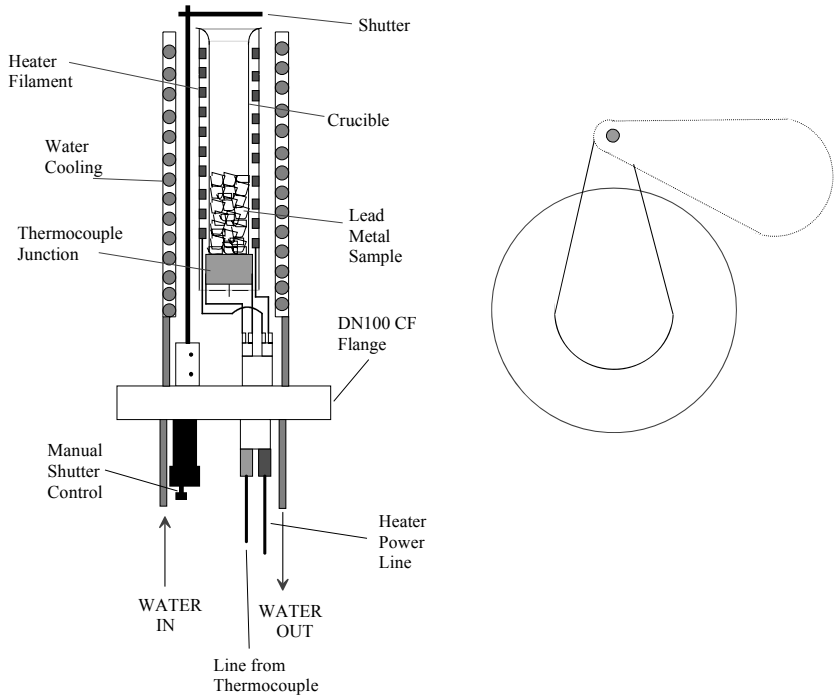

Figure 2.6 Schematic drawing of high temperature effusion cell [1] and shutter [8]. The solid line describes the closed position of the shutter and the dashed line the open position.

The effusion cell also called an oven is built into a thick metal disk called a flange which is mounted on the wall of the pick-up chamber. This creates a gas tight seal so high vacuum can be achieved in the pick-up chamber during operation. The region surrounding the effusion cell is pumped by two 150 l/s turbomolecular pumps backed a single 8 l/s rotary pump. The involatile sample is put in a crucible which is lowered into the oven. The oven contains graphite so any presence of oxygen during high temperature would lead to combustion of this expensive part. The crucible material

was usually pyrolytic boron nitride (PBN) but certain metals destroy PBN necessitating use of aluminium oxide crucibles. During operation the oven is resistively heated and the temperature is measured by measuring the resistivity of a second resistor. A digital feedback system is used to adjust the temperature of the effusion cell to the desired value in order to get a suitable vapour density of the metal. The specific temperature needed depends on which metal is being used, where the trend follows that of boiling points at standard pressure. Thus metals which boil at high temperatures need high temperatures in the effusion cell. The cell also has a shutter which is much colder than the oven causing most metal atoms hitting the shutter to get stuck. Most metal atoms will hit the shutter when it is in the closed position. This can be used to find out whether a beam at a particular mass contains any metal dependent signal because then signal will be much higher when the shutter is open than when it is closed.

Charge stripping experiments have been made with six different metals. Results are shown for five of the metals in the results chapters. The oven temperatures used for the six metals are given in Table 2.1.

Metal	Colour	Crucible	Temp /°C
Mg	Silver	PBN	470
Ca	Silver	Al_2O_3	580
Mn	Brown	PBN	1050
Cu	Red	PBN	1280
Zn	Silver	PBN	320
Pb	Grey	Al_2O_3	800

Table 2.1 Metals used in the oven. Crucible materials, temperatures, and colours of the metals are also shown.

The temperature in the oven was read using a thermocouple but it only read the temperature every few minutes. In order to ensure a stable temperature it was necessary to set the heating voltage so the ultimate temperature is only slightly higher than the desired temperature.

2.2.6 Pick-up chamber

The oven is needed to vaporise involatile compounds whose vapour crosses the cluster beam in the pick-up chamber. The pick-up chamber is depicted in Figure 2.7.

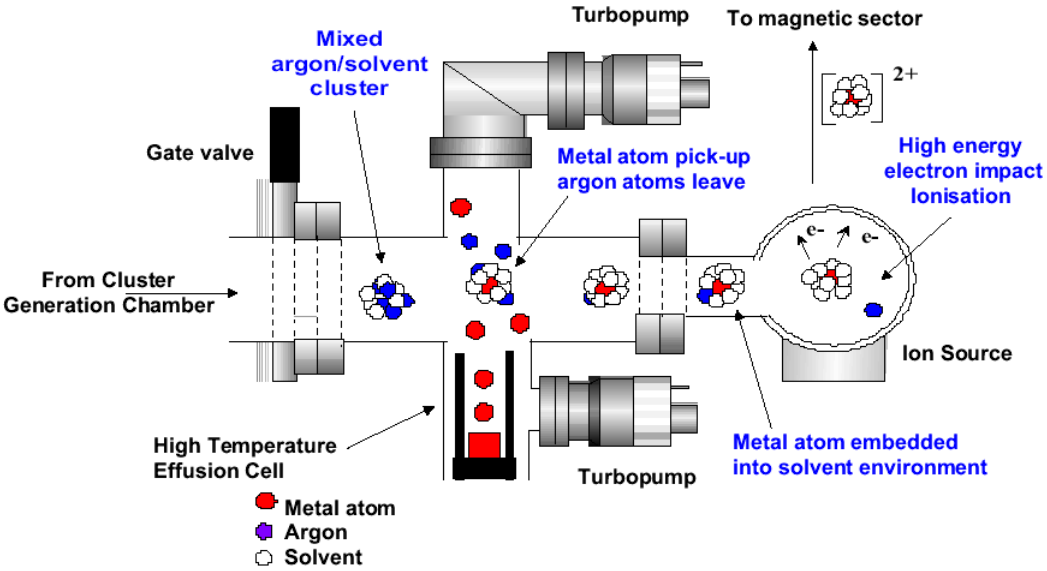

Figure 2.7 Schematic drawing of pick-up region [2].

The pick-up region is where the effusing metal is crossed by the beam of solvent/argon clusters. The term pick-up was first used by Scoles and co workers for their studies of insertion of SF_6 on the surface of argon clusters [9]. The Stace group used pick-up to generate metal complexes for later ionisation [10, 11]. When a collision occurs between a metal atom and a cluster the metal is likely to merge into

the cluster and the excess energy gained by condensation of the metal is then lost by evaporation of argon atoms. The metal atom is much more likely to be captured if the cluster contains argon atoms than if it only contains solvent molecules. The pick-up chamber is separated from the cluster generation part and the ionisation region by two gate valves enabling the pick-up chamber to be vented without venting the cluster generation part or the ionisation part of the mass spectrometer.

2.2.7 Ionisation source

In order to accelerate the clusters created they must be ionised and that happens in the ionisation source which the clusters enter approximately 1 ms after pickup. The central part of the ionisation source is a metal block approximately 4cm x 4cm x 2cm. It contains two small holes were the cluster beam can enter and exit. Free electrons are generated by a tungsten filament outside the block and they are subsequently accelerated towards the ionisation region inside the block where they hit atoms, molecules, and clusters causing ionisation. The electron energy can go up to 100 eV which is usually desired in order to make dications but it can also go as low as 15 eV. The ion source is in principle capable of functioning both as EI and CI but modifications made to allow for use with a cluster source have rendered the CI mode inoperable because the inlet necessary to make a localised high pressure region have been blocked. Ions formed are extracted by a small voltage difference between +40 V and -40 V towards the acceleration area. There they are accelerated by an adjustable voltage in integer kV units from 1 to 10 kV with 5 kV as the only used voltage in this work.

The kinetic energy expressed by mass m and velocity v is equal to the product of the charge z and the acceleration voltage V used.

$$\tfrac{1}{2}mv^2 = zV \tag{2.11}$$

This quantity will be of use later on when the properties of the magnetic sector is discussed.

2.2.8 Magnetic sector

The magnetic sector used in the ZAB-E mass has a radius of curvature of 66 cm and a 35° deflection angle.

The magnetic sector is designed to have a homogenous magnetic field inside it which will make ions have curved trajectories forming part of a circle. The flight path which has a radius corresponding to the curvature of the mass spectrometer will transmit ions to later parts of the experiment. The force exerted on a charge z in an electromagnetic field is a vector $\boldsymbol{F}$ expressed by its velocity $\boldsymbol{v}$, the magnetic field $\boldsymbol{B}$, and the electric field $\boldsymbol{E}$. In Equation 2.12 vectors are denoted by arrows rather than bold letters.

$$\vec{F} = z(\vec{v} \times \vec{B} + \vec{E}) \tag{2.12}$$

The force on an ion moving perpendicular to a magnetic field has a magnitude which can be expressed by its charge z and the magnitude of its velocity and the magnetic field.

$$F_m = zvB \tag{2.13}$$

The radial force needed to ensure a particle moves in a circular orbit depends on the mass m and velocity v of the particle and the radius r of the orbit.

$$F_{cr} = \frac{mv^2}{r} \tag{2.14}$$

Ions are transmitted when the Lorentz force provides the necessary force to ensure that the ions move in the specific curved trajectory causing transmission of the ion.

$$F_{cr} = F_m = zvB = \frac{mv^2}{r} \tag{2.15}$$

It can be seen by rearrangement of the above equation that a magnetic sector serves to filter ions according to their momentum to charge ratio.

$$\frac{mv}{z} = rB \tag{2.16}$$

The velocity can of course be isolated and described by the other quantities.

$$v = \frac{zrB}{m} \tag{2.17}$$

This can be inserted into equation 2.11.

$$\tfrac{1}{2}mv^2 = \tfrac{1}{2}m\left(\frac{zrB}{m}\right)^2 = \tfrac{1}{2}\frac{z^2r^2B^2}{m} = zV \tag{2.18}$$

This can be rearranged.

$$\frac{m}{z} = \frac{B^2r^2}{2V} \tag{2.19}$$

Since the magnetic field and acceleration voltage can be determined by the mass spectrometer and the radius of the magnet is a fixed value the mass to charge ratio is what is displayed by the mass spectrometer. The charge can only have very few integer values so the magnetic sector is used for selecting ions of a particular mass and charge.

2.2.9 Collision cell

The mass and intensities of fragments from a collision may give useful chemical insight so a collision cell is added in the second FFR in order to achieve collisions between fast moving projectiles and near static target gases. There are entrance and exit slits on collision cell allowing the ions to pass the collision cell which has 20 mm flight path. Gas can be fed into the collision cell from a gas cylinder using a needle valve to control the flow rate of gas. The pressure inside is approximately 10^{-6} mbar

during operation which is much higher than the 10^{-7} mbar in the vacuum chamber surrounding it. The slits are necessary to keep a pressure difference between the collision cell and the surroundings. In order to produce collision spectra the intensity of the ion beam must decrease noticeably upon filling with gas.

2.2.10 Electrostatic sector

Upon passage of the second Field Free Region (FFR) ions enter the electric sector where they follow curved trajectories and this time it is an electric field responsible for bending the flight path of the ions. The electric sector of the ZAB-E has 38 cm radius of curvature and 81° deflection angle. The force exerted by an electric field on an ion is the product of the electric field *E* and the charge of the ion.

$$F_e = zE \tag{2.20}$$

This can be equated to the force in Equation 2.14.

$$F_e = F_r = zE = \frac{mv^2}{r} \tag{2.21}$$

Insertion of equation 2.11 into equation 2.21 makes a relationship between the electric field and the acceleration voltage.

$$zE = \frac{mv^2}{r} = \frac{2\left(\frac{1}{2}mv^2\right)}{r} = \frac{2zV}{r} \tag{2.22}$$

From equation 2.22 it can be seen that an electric sector acts as an energy filter. During a mass scan the electric field is held constant to ensure all accelerated ions are detected.

2.2.11 Detection system

The mass spectrometer is able to operate in both single and double focusing mode with a detector in the second FFR for single focusing and in the third FFR for double focusing. In detectors ions with high velocity hit a metal surface which emits electrons upon impact. The free electrons generated are accelerated towards a phosphor screen which lights up upon impact. A photomultiplier tube converts the light into an electrical pulse which can be recorded by the lock-in amplifier to make a computer readable data file.

2.3 Experiments

The results presented in this work arise from one type of experiment only called mass analysed ion kinetic energy (MIKE) spectra. However some work was done during the project using another scan technique called mass spectra (MS). In order to make a complete description of the methods used and the versatility of the mass spectrometer both methods are described.

2.3.1 Mass spectra (MS)

Mass spectra are obtained by scanning the magnetic field while keeping the electric field constant. The abundances of ions are recorded and converted to abundances as a function of mass.

2.3.2 MIKE spectra (MIKE)

Mass analysed Ion Kinetic Energy (MIKE) spectra measure the mass of ions formed from fragmentation in the second FFR by assuming there is a linear relationship between the mass of an ion and the kinetic energy of an ion. Two processes which can prompt fragmentation are collision and photon absorption. A third situation where fragmentation occurs is metastable decay. Spectra arising from the first process which is often called collision induced dissociation (CID) are the only ones examined in this work. Equations already derived can be used to find the electric field necessary to transmit certain daughter ions produced from the parent ion. It is assumed that the velocities of the daughter and parent ions are the same. Their kinetic energies are known from the classical equations.

$$K_p = \tfrac{1}{2} m_p v^2 \tag{2.23}$$

$$K_d = \tfrac{1}{2} m_d v^2 \tag{2.24}$$

Equation 2.21 is rewritten in another form by multiplying by *r* on both sides enabling subsequent manipulation.

$$rzE = mv^2 \tag{2.25}$$

The terms on each side of Equation 2.24 for a daughter ion can now be divided by those for a parent ion.

$$\frac{rz_d E_d}{rz_p E_p} = \frac{2K_d}{2K_p} = \frac{m_d}{m_p} \tag{2.26}$$

Subsequent rearrangement yields an equation which expresses the scanning voltage in terms of properties of the ions.

$$E_d = \frac{z_p}{z_d}\frac{m_d}{m_p}E_p \tag{2.27}$$

Thus a MIKE scan using a doubly charged parent ion must go from double the voltage of passage of the parent down to zero in order to include the whole range.

2.4 Theoretical methods

Quantum chemical calculations were performed using the program package Q-Chem 3.0. The thermodynamically potential calculated quantum mechanically is the internal energy denoted U. Many of the calculations performed involved transition metal atoms but unfortunately only few basis sets supports transition metal atoms. Those that do are two Pople basis sets (6-31G and 6-31G*), three Aldrich's basis sets (TZV, VDZ, and VTZ), the thermochemical basis sets G3MP2LARGE, and finally several pseudopotentials. The manual for Q-Chem 2.1 says G3MP2LARGE supports

transition metal atoms while the manual for Q-Chem 3.0 says it does not. This is a mistake in the manual as transition metal atoms are indeed supported. The small basis sets 6-31G* and VTZ both have d orbitals while G3MP2LARGE has g orbitals as the highest angular momentum orbitals. The result is that calculations using the small basis sets quickly converge in contrast to those using G3MP2LARGE. Conversely the calculated energies using small basis sets are inaccurate while those using G3MP2LARGE are close to the complete basis set limit. Calculations using G3MP2LARGE frequently do not converge and this is especially the case for calculations involving transition metals. This problem can be remedied by starting the calculation using initial orbitals projected from optimised orbitals calculated using a small basis set. Two methods exists for projection and the only one of them that usually works with transition metal atoms is called by setting the keyword BASISPROJTYPE to OVPROJECTION. Q-Chem displays orbital energies and often the orbital energies are ordered according to irreducible representation of the orbitals. If the species examined is spherical or linear it may be necessary to make a CCSD calculation to get the irreducible representations printed. This does not have to be time consuming as all orbitals can be set as core orbitals leaving them out of the correlated optimisation. Molpro in contrast to Q-Chem can optimise states of molecules specified by their irreducible representation and also generate tables of energies as a function of internuclear distances. Unfortunately the manual and user interface of Molpro is rather user unfriendly.

2.5 References

1. B. J. Duncombe, *Energetics and fragmentation pathways of multiply charged metal-ligand complexes*. 2003, The University of Sussex, DPhil thesis.
2. L. Puskar, *Gas Phase Ligand Field Photofragmentation Spectroscopy*. 2001, The University of Sussex, DPhil Thesis.
3. K. R. Jennings, *Fundamentals and Applications of Gas Phase Ion Chemistry*. 1999: Kluwer Academic Publishers.
4. H. Haberland, *Clusters of Atoms and Molecules*. 1994, Berlin: Springer-Verlag.
5. J. E. Campana, *Cluster ions. I. Methods.* Mass Spectrom. Rev., 1987. **6**: p. 395.
6. R. Camparague, *Progress in overexpanded supersonic jets and skimmed molecular beams in free-jet zones of silence.* J. Phys. Chem., 1984. **88**: p. 4466.
7. O. F. Hagena, *Nucleation and growth of clusters in expanding nozzle flows.* Surf. Sci., 1981. **106**: p. 101.
8. N. R. Walker, *Gas-Phase Studies of Multiply-Charged Transition Metal Complexes*. 1999, The University of Sussex, DPhil Thesis.
9. T. E. Gough, et al., *Infrared spectroscopy at the surface of clusters: SF6 on Ar.* J. Chem. Phys., 1985. **83**: p. 4958.
10. Woodward, C.A.D., M. P.; Stace, A. J., *Intracluster Charge-Transfer Chemistry in [Mg·(C3H7OH)n]2+ Complexes* J. Phys. Chem., 1996. **100**: p. 5605.
11. M. P. Dobson and A. J. Stace, *$Mg(thf)_4^{2+}$: The first gas-phase evidence of a stable multiply charged metal-ligand unit.* Chem. Com., 1996. **13**: p. 1533.

Chapter 3
Charge stripping

3.1 Introduction

This chapter presents theoretical results regarding transfer of electrons from projectiles to neutral target gases as described in Reaction R1.1. The chapter also presents experimental results regarding transfer of electrons from monocationic metal complexes to neutral target gases as described in Reaction R1.3.

3.2 Orbitals of molecules

The focus of these calculations is to find out which molecules can trap electrons in fast collisions where the nuclei in the target have approximately fixed positions. Molecular orbitals do not have quantised angular momenta although linear molecules have quantised angular momenta projections along the molecular axis. Angular momenta lead to centrifugal barriers. It is hypothesised that the efficiency of trapping relates to the propensity of a trapped electron to tunnel away in the electric field of a charged collision partner.

These calculations determine the amount of atomic s, p, and d orbital component as well as the orbital energies. Three methods for finding the EA are used here which are ΔSCF, Koopmans' theorem [1], and Tozer's theorem [2]. The equations for the energies by ΔSCF, Koopmans' theorem, and Tozer's theorem are given below.

$$EA_{\Delta SCF} = E(M) - E(M^{-}) \tag{3.1}$$

$$EA_{KT} = -\varepsilon_{LUMO} \tag{3.2}$$

$$EA_{TT} = -\varepsilon_{LUMO} - \left(IE + \varepsilon_{HOMO}\right) \tag{3.3}$$

From the last two equations it can be seen that Tozer's theorem is a correction to Koopmans' theorem. DFT calculations were performed using B3LYP with the aug-cc-pVDZ basis set. B3LYP is a hybrid functional with the exchange part comprised of 72% Becke, 20% Hartree-Fock, and 8% Slater while the correlation part is comprised of 81% LYP and 19% VWN1RPA. The Hartree-Fock exchange is deficient in the sense that it does not have the charge discontinuity property that Tozer's theorem relies on. For this reason BLYP was used rather than B3LYP to calculate HOMO and LUMO energies. B3LYP was used to calculate all other properties because it gives accurate results and calculations using it rarely fail to converge.

Orbitals are analysed by partial Mulliken populations and by natural bond orbitals. Mulliken population analysis uses the optimised orbitals which are frequently delocalised over several atoms. All the occupied orbitals are normalised and orthogonal to each other and all virtual orbitals. The virtual orbitals are not normalised and only orthogonal to each other if they belong to symmetries of different irreducible representations. Partial Mulliken populations are supposed to give contributions ranging from 0 % to 100 % but may sometimes give percentages outside this range although they strictly add up to 100 % for any molecule where all the contributions are added. The problem of negative contributions is bad for s orbital contribution of totally symmetric orbitals particularly of molecules with large HOMO LUMO gaps. Partial Mulliken population analysis is thus a rather poor method for

determining orbital components. In natural bond orbitals (NBO) the orbitals are normalised and localised as lone pairs or as localised bonds. Bonds are treated as additions between two atomic hybrid orbitals and anti bonds are subtractions. Thus the charge of bonds are the integrals of $(A + B)^2$ where A and B are atomic hybrid orbitals and this is normalised to unity. In contrast the charge of anti bonds is $(A - B)^2$ and this is smaller than unity. NBO give percentages in the range 0 % to 100 % and sums up to 100 %. NBO gives reasonably good results even for delocalised bonds but it fails for open shell species and hypervalent species containing π bonds.

3.2.1 Electron deficient σ-bonds

Electron deficient sigma bonds are defined here as localised σ-bonds where at least one of the participating atoms does not have a lone pair. Orbital numbers, orbital energies, orbital symmetries, and partial Mulliken populations of the LUMO and HOMO orbitals in H_2 and HF are shown in Table 3.1.

Orbital	Symbol	Energy	H s%	H p%	H d%	H s%	H p%	H d%
1	A_{1g}	-11.6	50	-	-	50	-	-
2	A_{1u}	0.4	41	9	-	41	9	-
Location	Type		H s%	H p%	H d%	H s%	H p%	H d%
1	σ		50	-	-	50	-	-
2	σ*		50	-	-	50	-	-
Orbital	Symbol	Energy	F s%	F p%	F d%	H s%	H p%	H d%
4-5	E_1	-11.5	-	98	-	-	2	-
6	A_1	-0.8	1	2	-	91	6	-
Location	Type		F s%	F p%	F d%	H s%	H p%	H d%
F	LP		-	100	-	-	-	-
H-F	σ*		4	18	-	78	-	-

Table 3.1 Mulliken populations of electron deficient diatomic molecules. Populations shown for hydrogen contain the sum of the contributions from both hydrogen atoms. Values were calculated by DFT using B3LYP with aug-cc-pVDZ and the energies given are orbital energy eigenvalues in eV. The symbols given are the symmetries of each orbital with the LUMO marked in bold.

The simplest molecules examined were the simple hydrides H_2, CH_4, NH_3, H_2O, and HF. It is observed that the LUMO orbital energies progressively decrease along the series from 0.4 eV for H_2 to -0.8 eV for HF. This is no surprise as the electronegativity of the central atom progressively increases. Koopmans' theorem incorrectly predicts that all the molecules examined containing heavy atoms have positive electron affinities. For molecules containing heavy atoms calculated partial Mulliken populations become increasingly physically unrealistic as the electronegativity of the heavy atom decreases. The s orbital contribution to the LUMO from the heavy atom progressively decreases from 1% for HF to -40% for CH_4 while the sum of the s orbital contributions increases from 91% for HF to 136% for CH_4. The molecules are all isoelectronic with Ne and the triplet excited state has an electron in an orbital corresponding to 3s making it a totally symmetric anti-bonding orbital. The higher lying 3p orbital would give an odd wavefunction with respect to

mirroring in one plane. Also C_2H_6, CH_3F, and CH_3Cl were examined and they too had problems with negative s orbital contributions from heavy atoms.

The last molecule containing only electron deficient σ-bonds is SF_6 and the results are shown in Table 3.2.

Sulphur hexafluoride SF_6			Partial Mulliken populations					
Orbital	Symbol	Energy	S s%	S p%	S d%	F s%	F p%	F d%
33-35	T_{1g}	-12.2	-	-	-	-	100	-
36	A_g	-3.7	55	-	-	-7	53	-1
Sulphur hexafluoride SF_6			Natural bond orbitals					
Location	Type		S s%	S p%	S d%	F s%	F p%	F d%
F	LP		-	-	-	-	100	-
S-F	σ*		13	40	26	3	18	-

Table 3.2 Mulliken populations of SF_6. Populations, symmetries, and energies shown in eV are calculated using B3LYP with aug-cc-pVDZ where populations are sums for each element. The population of the LUMO marked in bold is calculated from the triplet excited state.

SF_6 is the only electron deficient molecule examined containing bonds between two electronegative atoms and its LUMO is symmetrically delocalised between all seven atoms. The result is that SF_6 has a very low lying LUMO but because it has large s orbital component SF_6^- should easily field detach in the presence of an electric field which certainly would be present in a collision complex.

3.2.2 Electron rich σ-bonds

Electron rich bonds are defined here as bonds where both participating atoms have lone pairs. F_2, Cl_2, NF_3, and SF_4 were examined and he results for F_2 are displayed in Table 3.3.

Fluorine F_2			Partial Mulliken populations					
Orbital	Symbol	Energy	F s%	F p%	F d%	F s%	F p%	F d%
8-9	E_{2g}	-11.5	-	50	-	-	50	-
10	A_{2u}	-4.5	-	50	-	-	50	-
Fluorine F_2			Natural bond orbitals					
Location	Type		F s%	F p%	F d%	F s%	F p%	F d%
F	LP		-	100	-	-	-	-
F-F	σ*		2	48	-	2	48	-

Table 3.3 Mulliken populations of F_2. Populations, symmetries, and energies shown in eV are calculated using B3LYP with aug-cc-pVDZ where populations are sums for each element. The population of the LUMO marked in bold is calculated from the triplet excited state.

The halogens appear to be able to attach electrons to their LUMO orbitals because of their calculated low energies. This is consistent with the high electronegativity of both elements. In both molecules the LUMOs have almost complete p orbital character giving rise to centrifugal barriers to detachment.

3.2.3 Isolated π-bonds

This group contains C=C, C=O, and S=O double bonds as the molecules examined were ethylene, formaldehyde, acetone, and DMSO. The results for ethylene and formaldehyde are displayed in Table 3.4.

Ethylene C_2H_4			Partial Mulliken populations					
Orbital	Symbol	Energy	C s%	C p%	C d%	H s%	H p%	H d%
8	B_{1u}	-7.6	-	95	1	-	4	-
9	B_{2g}	-0.3	-	91	3	-	6	-
Ethylene C_2H_4			Natural bond orbitals					
Location	Type		C s%	C p%	C d%	H s%	H p%	H d%
C-C	π		-	100	-	-	-	-
C-C	π*		-	100	-	-	-	-
Formaldehyde CH_2O			Partial Mulliken populations					
Orbital	Symbol	Energy	C s%	C p%	C d%	O s%	O p%	O d%
8	B_1	-7.6	-	4	4	-	68	-
9	B_2	-1.8	-	72	2	-	19	-
Formaldehyde CH_2O			Natural bond orbitals					
Location	Type		C s%	C p%	C d%	O s%	O p%	O d%
C-O	π		-	35	-	-	65	-
C-O	π*		-	65	-	-	35	-

Table 3.4 Mulliken populations of ethylene and formaldehyde. Populations, symmetries, and energies shown in eV are calculated using B3LYP with aug-cc-pVDZ where populations are sums for each element. The population of the LUMO marked in bold is calculated from the triplet excited state.

The Mulliken populations on hydrogen are not shown in Table 3.4 therefore the populations do not add up to 100% in the table presented. The presence of an electronegative oxygen atom lowers the LUMO energy of formaldehyde relative to the LUMO energy of ethylene. All the molecules have π* LUMO orbitals giving rise to centrifugal barriers.

3.2.4 Conjugated carbonyl groups

This group contains both aliphatic and aromatic molecules. Glyoxal, cyclopentadienone, and para-quinone containing conjugated carbonyl bonds were examined. The results for glyoxal are displayed in Table 3.5.

Glyoxal $C_2H_2O_2$			Partial Mulliken populations					
Orbital	Symbol	Energy	C s%	C p%	C d%	O s%	O p%	O d%
15	A_g	-7.7	1	11	5	-	66	-
16	A_u	-3.5	-	56	5	-	37	-
Glyoxal $C_2H_2O_2$			Natural bond orbitals					
Location	Type		C s%	C p%	C d%	O s%	O p%	O d%
O	LP		-	-	-	-	100	-
C-O	π*		-	65	-	-	35	-

Table 3.5 Mulliken populations of formaldehyde and glyoxal. Populations, symmetries, and energies shown in eV are calculated using B3LYP with aug-cc-pVDZ where populations are sums for each element. The population of the LUMO marked in bold is calculated from the triplet excited state.

Mulliken populations on hydrogen are not shown in Table 3.5 so the populations do not add up to 100%. The presence of a conjugated carbonyl group lowers the LUMO energies relative to the LUMO energy of formaldehyde so they all form stable anions. From an analysis of the complete dataset it is seen that molecules with LUMO energies higher than -3 eV do not form stable anions whereas those with LUMO energies lower than -3 eV do. The LUMO orbitals examined in this section are all π* orbitals giving rise to centrifugal barriers.

3.2.5 Aromatic molecules

The aromatic molecules benzene, perfluorobenzene, and furan were examined and the results for benzene are displayed in Table 3.6.

Benzene C_6H_6			Partial Mulliken populations					
Orbital	Symbol	Energy	C s%	C p%	C d%	H s%	H p%	H d%
20-21	E_{1g}	-7.0	-	95	3	-	2	-
22-23	E_{2u}	-0.5	-	88	8	-	3	-
Benzene C_6H_6			Natural bond orbitals					
Location	Type		C s%	C p%	C d%	C s%	C p%	C d%
C-C	π		-	50	-	-	50	-
C-C	π*		-	50	-	-	50	-

Table 3.6 Mulliken populations of aromatic molecules. Populations, symmetries, and energies shown in eV are calculated using B3LYP with aug-cc-pVDZ where populations are sums for each element. The populations of the LUMO orbitals marked in bold are calculated from the triplet excited states.

The molecules in Table 3.6 are closed shell aromatic molecules. The presence of many fluorine atoms in perfluorobenzene lowers the LUMO energy relative to that of benzene enabling it to adiabatically form a stable anion [3]. The molecule AMP contains an aromatic moiety that form a sufficiently long lived anion resonance to fragment by hydrogen atom loss [4]. However none of the molecules can support an extra electron vertically according to calculations in this work. Both benzene and furan have π* LUMO orbitals giving rise to centrifugal barriers. Fullerenes can be though of as extended π systems so they should be very able to trap electrons. Unfortunately they are much less able than O_2 at trapping electrons and this needs an explanation. If fullerene anions have an s orbital component they would be much more efficiently field ionised than if they do not. In order to find out if fullerenes have an s orbital component a constrained calculation reflecting the geometry of fullerenes was carried out. C_{60} is composed of regular pentagons and hexagons with bond angles of 108° and 120° respectively. A constrained optimisation using B3LYP with aug-cc-pVDZ was performed on ethylene where the CCH angles were 120° and the HCH angles were 108°. Due to the non-planarity of the constrained molecule some s orbital

component of the π orbitals is mixed in and the resulting natural bond orbital of the π bond contains 12 % s orbital character. Assuming π orbitals in fullerene have similar s orbital components this could explain why fullerene is not a good charge stripper as fullerene anions can easily be field ionised due to their absent centrifugal barriers arising from their s orbital components.

3.2.6 Oxygen rich molecules

This group is defined as having at least two oxygen atoms bound to a sp^2 hybridised atom but also includes singlet O_2. O_2, O_3, SO_2, SO_3, and CF_3NO_2 were examined and the results for O_2, SO_2, and SO_3 are displayed in Table 3.7.

Singlet oxygen O_2			Partial Mulliken populations					
Orbital	Symbol	Energy	O s%	O p%	O d%	O s%	O p%	O d%
8	B_{2g}	-7.6	-	99	1	-	-	-
9	B_{3g}	-5.7	-	100	-	-	50	-
Singlet oxygen O_2			Natural bond orbitals					
Location	Type		O s%	O p%	O d%	O s%	O p%	O d%
O	LP		-	100	-	-	-	-
O-O	π*		-	50	-	-	50	-
Sulphur dioxide SO_2			Partial Mulliken populations					
Orbital	Symbol	Energy	S s%	S p%	S d%	O s%	O p%	O d%
16	A_1	-9.4	12	10	9	2	68	-
17	B_2	-4.2	-	56	4	-	41	-1
Sulphur dioxide SO_2			Natural bond orbitals					
Location	Type		S s%	S p%	S d%	O s%	O p%	O d%
O	LP		-	-	0	2	97	1
S-O	π*		-	67	1	-	32	-
Sulphur trioxide SO_3			Partial Mulliken populations					
Orbital	Symbol	Energy	S s%	S p%	S d%	O s%	O p%	O d%
20	A2'	-9.8	-	-	-	-	100	-
21	A2"	-3.5	-	54	-	-	47	-1
Sulphur trioxide SO_3			Natural bond orbitals					
Location	Type		S s%	S p%	S d%	O s%	O p%	O d%
C-C	π		-	28	1	-	71	-
C-C	π*		-	70	2	-	28	-

Table 3.7 Mulliken populations of oxygen rich molecules. Populations, symmetries, and energies shown in eV are calculated using B3LYP with aug-cc-pVDZ where populations are sums for each element. The populations of the LUMO orbitals marked in bold are calculated from the triplet excited states.

The definition of what constitutes an oxygen rich molecule was carefully chosen to encompass molecules with π* LUMO orbitals delocalised over at least two O atoms. All the LUMO orbitals are π* orbitals with very low energy so they should have centrifugal barriers and be very able to trap electrons. A study by S. Tomita *et al*. [5] revealed that O^- ions were formed in high energy collisions between cationic biomolecules and O_2. The interpretation was that some O_2^- was formed in the excited $^2\Pi_u$ state which subsequently decayed into O^- and O. This state might be more

resistant to field ionisation than the ground state of O_2^- because it would decay by a single electron process to the excited $^3\Sigma_u^-$ state of neutral O_2. Furthermore the hole in the electron density would result in an overall positive charge between the two atoms causing the LUMO electrons to be very resistant to external fields. This might explain the ability of O_2 to capture electrons.

3.2.7 Linear molecules

This group contains molecules with π bonds but without π* orbitals. N_2, CO, N_2O, CO_2, and C_2H_2 were examined and the results for CO are displayed in Table 3.8.

Carbon monoxide CO			Partial Mulliken populations					
Orbital	Symbol	Energy	C s%	C p%	C d%	O s%	O p%	O d%
7	A_1	-10.5	43	39	-	7	10	1
8-9	E_1	-1.2	-	67	5	-	28	1
Carbon monoxide CO			Natural bond orbitals					
Location	Type		C s%	C p%	C d%	O s%	O p%	O d%
C-O	σ		7	21	-	32	40	1
C-C	π*		-	77	-	-	23	-

Table 3.8 Mulliken populations of linear molecules. Populations, symmetries, and energies shown in eV are calculated using B3LYP with aug-cc-pVDZ where populations are sums for each element. The populations of the LUMO orbitals marked in bold are calculated from the triplet excited states.

The molecules in this section are linear and electron deficient molecules. The calculated LUMO orbitals have π* character except for C_2H_2 where it has σ* character. However when the triplet excited state is calculated the converged LUMO is of π* character. It is interpreted as the LUMO being of π* character resulting in a centrifugal barrier. These molecules have high HOMO-LUMO gaps compared to

other unsaturated closed shell species. This is consistent with the experimental electron affinities which are very negative [6].

3.3 Electron affinities

Electron affinities were calculated as a first estimate from application of Koopmans' Theorem (Equation 3.3) in the preceding section. The two methods ΔSCF (Equation 3.2) and Tozer's Theorem (Equation 3.4) can also be employed after calculation of the energies of the corresponding cations and anions. Electron affinities calculated by the three methods are listed in Table 3.9 and Table 3.10.

Molecule	EA KT	EA ΔSCF	EA TT	EA Lit	Method
Cl_2	4.90	1.37	0.64	2.50 [7]	NBIE
SF_6	5.31	1.02	0.48	0.46 [7]	NBIE
SF_4	4.19	0.53	0.01	1.50 [7]	IMRB
F_2	6.29	0.71	-0.09	3.12 [7]	CID
NF_3	2.59	-1.83	-2.12		
CH_3Cl	1.03	-0.51	-3.32	-3.7 [8]	ETS
C_2H_6	0.49	-0.64	-3.66		
NH_3	0.84	-0.51	-3.95	-5.6 [8]	ETS
CH_4	0.46	-0.69	-4.43	-7.8 [8]	ETS
CH_3F	0.54	-0.60	-4.49	-6.2 [8]	ETS
H_2O	1.12	-0.52	-4.50	-6.4 [8]	ETS
HF	1.22	-0.59	-5.55	-6.0 [8]	ETS
H_2	-0.05	-1.23	-6.22	-2.0 [8]	ETS

Table 3.9 Electron affinities of saturates molecules. HOMO and LUMO energies are calculated by BLYP and all other quantities by B3LYP while the basis set in all cases was aug-cc-pVDZ. KT = Koopmans' Theorem, TT = Tozer's Theorem, NBIE = Neutral Beam Ionisation Energy, IMRB = Ion Molecule Reaction Bracketing, CID = Collision Induced Dissociation, and ETS = Electron Transfer Spectroscopy.

It is observed that the first four molecules have positive vertical electron affinities but all the rest have high negative electron affinities. SF_6 stands out by having a totally symmetric LUMO which has considerable s orbital component on the sulphur atom. The LUMO orbitals of F_2 and Cl_2 have very little s orbital component and the LUMO

of SF_4 has no s orbital component as the symmetry prohibit that. It was difficult to analyse the s orbital component of certain polyatomic molecules as the orbitals were not localised NBO orbitals. Thus Cl_2, SF_4, F_2 have centrifugal barriers and should be able to trap electrons. Fluorine atoms have smaller spatial extent than chlorine atoms so they should be more affected by centrifugal barriers which have r^{-2} dependence. Thus F_2 should be more able than Cl_2 to trap electrons in a centrifugal barrier. The electron affinities calculated by Equation 3.4 have large deviation from literature values but the sign is correct and the magnitude clearly follows the experimental values. The electron affinities calculated by ΔSCF becomes completely inaccurate when the experimental vertical electron affinities becomes negative as expected.

Molecule	EA KT	EA ΔSCF	EA TT	Theo	Exp	Method
O_2	5.66	2.10	1.50		-0.091 [9]	ETS
O_3	6.29	2.21	1.46		2.10 [7]	LPES
Quinone	4.52	1.88	0.92		1.86 [7]	LPES
C_5H_4O	3.81	1.01	0.51			
SO_2	4.95	1.45	0.50		1.11 [7]	LPES
Glyoxal	4.35	1.00	0.23		0.62 [7]	CID
SO_3	4.35	0.85	-0.17		1.90 [7]	IMRB
C_6F_6	2.53	-1.60	-0.41		0.52 [7]	IMRE
CF_3NO_2	4.24	0.68	-0.42			
CH_2O	2.69	-0.59	-1.97		-1.5 [8]	
C_6H_6	1.14	-0.52	-2.00	-1.76 [10]	-1.2 [8]	TT/ETS
Acetone	1.69	-0.41	-2.33	-2.06 [11]	-1.5 [8]	PW/ETS
N_2O	2.20	-1.32	-2.46		-2.2 [8]	ETS
Furan	0.90	1.08	-2.49	-2.31 [11]	-1.76 [11]	PW/ETS
DMSO	0.79	-0.38	-2.81			
C_2H_4	1.03	-0.87	-2.97	-2.64 [11]	-1.8 [8]	PW/ETS
CO	2.12	-1.08	-3.06		-1.8 [8]	ETS
N_2	2.12	-1.85	-3.49		-2.2 [8]	ETS
C_2H_2	0.44	-0.27	-3.92		-2.6 [8]	ETS
CO_2	0.95	-0.90	-4.26		-3.8 [8]	ETS

Table 3.10 Electron affinities of unsaturated molecules. HOMO and LUMO energies are calculated by BLYP and all other quantities by B3LYP while the basis set in all cases was aug-cc-pVDZ. The state used theoretically as ground state for O_2 was $^1\Delta$ and unfortunately it could only be converged using B3LYP. KT = Koopmans' Theorem, TT = Tozer's Theorem, LPES = Laser Photo Electron Spectroscopy, CID = Collision Induced Dissociation, IMRB = Ion Molecule Reaction Bracketing, IMRE = Ion Molecule Reaction Equilibrium, ETS = Electron Transmission Spectroscopy, PW = Potential Wall.

The electron rich molecules and those with conjugated carbonyl groups have positive electron affinities while all the rest have negative electron affinities. The LUMO orbitals except in C_6F_6 are all π* orbitals so there should be centrifugal barriers to detachment of electrons.

3.4 Experimental charge stripping

Metal complexes were collided with a collision gas upon acceleration by a 5 keV potential and the resulting MIKE spectra were recorded. The experimental conditions are given in chapter 2. Unfortunately the gas pressure gauge was localised outside the

collision chamber so it was not possible to get a reliable estimate of the pressure in the collision chamber. However the ratio between the abundance of any doubly charged ion formed and the most abundant ion formed can be determined experimentally and it is expressed in Equation 3.5.

$$R = \frac{A(M^{2+})}{A(F_1^{+})} \tag{3.4}$$

There are two competing effects influencing the ratio *R*. Complexes with many ligands will stabilise the ionic core better than those with few ligands so they should donate an electron more easily. The acceleration voltage was in all cases 5 kV causing heavier complexes with many ligands move more slowly which has the effect of increasing the interaction time. Such complexes are thus less able to become stripped of electrons.

3.4.1 Charge stripping with O_2

Projectile metal complexes examined in this section were of the form ML_n^+ where M = Mg, Ca, Mn, and Zn while L = benzene, pyridine, acetone, acetonitrile, CO_2, and NH_3 with n = 1-6. The collision gas was O_2 and the ratios *R* are displayed in Figures 3.2 to 3.5 as a function of velocity of the complexes.

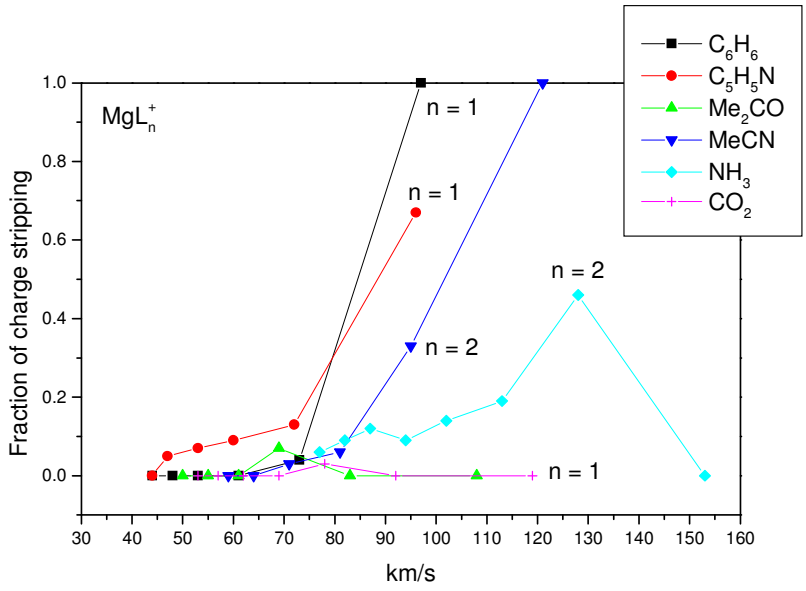

Figure 3.1 Charge stripping ratios of MgL_n^+ complexes. The charge stripping ratio is shown as a function of the velocity of the complexes.

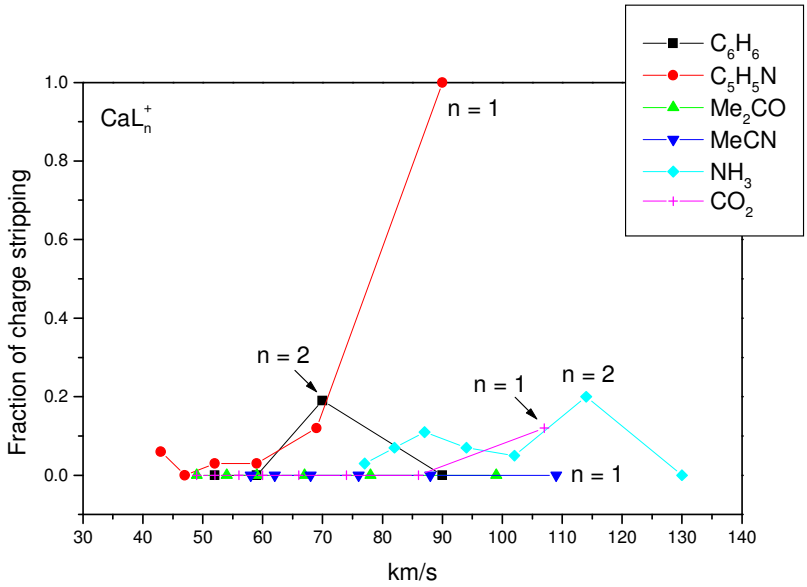

Figure 3.2 Charge stripping ratios of CaL_n^+ complexes. The charge stripping ratio is shown as a function of the velocity of the complexes.

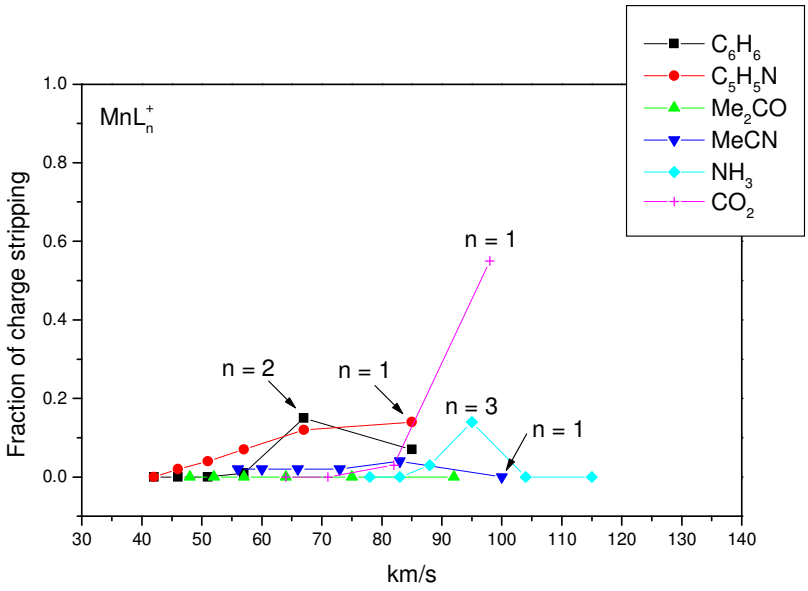

Figure 3.3 Charge stripping ratios of MnL_n^+ complexes. The charge stripping ratio is shown as a function of the velocity of the complexes.

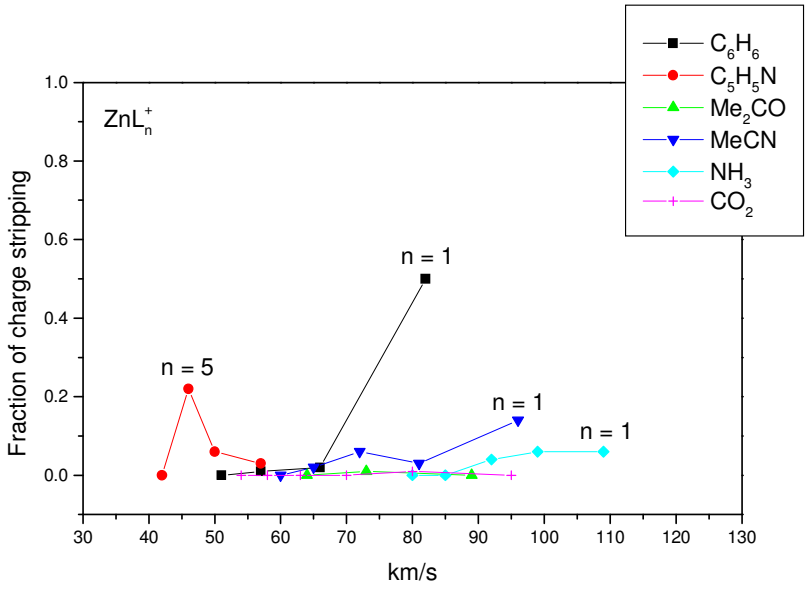

Figure 3.4 Charge stripping ratios of ZnL_n^+ complexes. The charge stripping ratio is shown as a function of the velocity of the complexes.

The data are divided into four series MgL_n^+, CaL_n^+, MnL_n^+, and ZnL_n^+ where n = 1-6. In each series the R ratio increases with the velocity of the complex and decrease with the second ionisation energy of the complexes. The general trend is one where the ratio increases with the velocity of the complex occasionally reaching a maximum value before decreasing.

In $M(benzene)_n^+$ complexes only the first two benzene ligands bind directly to the metal so they are strongly bound and this makes complexes robust for n = 1-2. In contrast, complexes for n > 2 may easily dissociate with charge separation, which would prevent dicationic complexes from being observed, consistent with their sudden disappearance in the spectra.

The experimental data obtained by collision in of metal complexes with O_2 did not reveal any discernible pattern that could be used to calculate *R* ratios.

3.4.2 Charge stripping with various targets

Complexes MgL_n^+ where L = benzene, pyridine, acetone, acetonitrile, CO_2, and NH_3 were collided with the collision gases benzene, acetonitrile, N_2O, and CO_2. It was found that only rarely could these collision gases strip electrons from a projectile. Charge stripping is used in neutralisation reionisation mass spectrometry [12], but it becomes much harder to strip an electron from a species which is already ionised. This can explain the absence of dications formed in collision with benzene, acetonitrile, N_2O, and CO_2. Thus it is not possible to compare experimental and theoretical data as collisional charge stripping was only possible for O_2 at the 5 keV

available. At higher collision energies charge stripping becomes more efficient so it might be possible to strip monocationic complexes by collision with other collision gases. In contrast it was possible to strip $Ru(bipy)_3^{2+}$ into $Ru(bipy)_3^{3+}$ by collision with O_2 using 50 kV acceleration voltage [13].

3.5 Summary and conclusions

Experimentally metal complexes of the form ML_n^+ where M = Mg, Ca, Mn, Cu, Zn with L = ammonia, carbon dioxide, acetone, acetonitrile, benzene, and pyridine and n = 1-6 have been collided with O_2 and the resulting MIKE spectra have been obtained. The experimental conditions were those standard conditions given in chapter 2. MgL_n^+ complexes have also been collided with carbon dioxide, nitrous oxide, acetonitrile, and benzene. Electron affinities of target gases have been calculated by DFT using the BLYP and B3LYP functionals with the basis set aug-cc-pVDZ. Vertical electron affinities have been calculated by Tozer's theorem. Atomic orbital components of LUMO orbitals of target gases have for the first time been calculated by partial Mulliken populations and natural bond orbitals in order to analyse for centrifugal barriers.

The acceleration voltage in the mass spectrometer was unfortunately too low to allow charge stripping with collision gases other than O_2. Thus any systematic experimental study of the effect of the collision gas on the charge stripping efficiencies was not possible. This makes the comparison between theory and experimental data in this work impossible as the theory developed here only deals with the electron trapping species in depth, while treating the electron donor only by its IE.

The σ* orbitals of saturated molecules have been analysed using the NBO package. The sum of s orbital contributions of σ* bonds between two heavy atoms are found to decrease steadily with increasing electronegativity of the two atoms according to the series C_2H_6 (28%) > CH_3F (21%) > CH_3Cl (16%) > SF_6 (16%) > NF_3 (11%) > SF_4 (9%) > Cl_2 (0%) ≈ F_2 (0%). This is hardly surprising as the difference between s and p orbital energies of atoms within a row in the periodic table increases with increasing atomic number. This trend for atoms persists for molecules so the s orbital component of frontier orbitals in molecules like C_2H_6 must be high while it must be low for molecules like F_2. The centrifugal barriers of Cl_2^- and F_2^- should then be the most effective towards detachment. Unsaturated molecules always have low energy π* orbitals which usually are the LUMO orbitals. Those orbitals due to symmetry have no s orbital contributions so they have efficient centrifugal barriers.

The centrifugal potential has r^{-2} dependence so atomic radii are expected to play a role in the depth of centrifugal barriers. Hence the ability to trap electrons should decrease in the series S < Cl < C < N < O < F as it reflects falling atomic radii. The effect of atomic radii can explain certain trends in reported electron capture cross sections. In Appendix A some bond lengths are given which are directly linked to the atomic radii in the hard sphere model.

It was known prior to this work that collisions are more likely to result in electron capture if the electron donor passes close through the LUMO of the electron acceptor. Ambiguity exists regarding whether sideways or end-on closest passage is most likely to result in transfer as each of those conclusions have been published for acetonitrile by the same group. SF_6 is reported to trap electrons from alkali metals [14] but not

from organic compounds [12]. It is not known if the poor capture cross section of SF_6 is due to poor overlap between initial and final states or due to s orbital character of the LUMO of SF_6.

Charge stripping cross sections tend to be high for molecules with high vertical EAs. Such behaviour could be explained by LZ theory if it was a near linear relationship rather than just a trend. The vertical EAs of molecules where the LUMO is σ* bonding between two atoms increase but the s orbital contribution of the LUMO decrease with increasing electronegativity of the two atoms. It is then not possible to tell how much charge stripping cross sections is influenced by each of those properties. It is also not easy to tell how much steric hindrance means to charge stripping cross sections. Isolated atoms should be the least hindered and coupled with the effects of EA and atomic radius the predicted best neutral charge stripper imaginable would be atomic fluorine which is a prime candidate for further research.

3.6 References

1. T. Koopmans, *Ordering of Wave Functions and Eigenvalues to the Individual Electrons of an Atom.* Physica, 1933. **1**: p. 104.
2. D. J. Tozer and F. De Proft, *Computation of the Hardness and the Problem of Negative Electron Affinities in Density Functional Theory.* J Phys. Chem. A, 2005. **109**: p. 8923-8929.
3. T. M. Miller, J. M. Van Doren, and A.A. Viggiano, *Electron attachment and detachment: C_6F_6.* Int. J Mass Spectrom., 2004. **233**: p. 67.
4. B. Liu, et al., *Electron Attachment to "Naked" and Microsolvated Nucleotide Anions: Detection of Long-Lived Dianions.* ChemPhysChem, 2003. **4**: p. 1341.
5. S. Tomita, et al., *Coincidence studies of O_2^-, O^- and electron formation in electron stripping of cationic biomolecules by molecular oxygen.* Int. J Mass Spectrom., 2002. **214**: p. 57-62.
6. G. J. Schulz, *Resonances in electron impact on diatomic molecules.* Rev. Mod. Phys., 1973. **45**: p. 423.
7. NIST. *NIST Chemistry WebBook*. [Webpage] [cited; Available from: http://webbook.nist.gov/chemistry/.
8. R. G. Pearson, *Absolute electronegativity and hardness: Application to inorganic chemistry.* Inorg. Chem., 1988. **27**: p. 734.
9. J. E. Land and W. Raith, *Fine structure of O_2^- measured by electron time-of-flight spectroscopy.* Phys. Rev. Lett., 1973. **30**: p. 193.
10. B. Hajgató, et al., *A benchmark theoretical study of the electron affinities of benzene and linear acenes.* J. Chem. Phys., 2008. **129**: p. 084308.
11. N. Sablon, et al., *On the position of the potential wall in DFT temporary anion calculations.* Phys. Chem. Chem. Phys., 2007. **9**: p. 5880.
12. P. O. Danis, R. Feng, and F. W. McLafferty, *Reionization Agents for Neutralization-Reionization Mass Spectrometry.* Anal. Chem., 1986. **58**: p. 355-358.
13. A. B. Nielsen, P. Hvelplund, and S. B. Nielsen, *Ruthenium diimine complexes in unusual charge states formed in collisional electron transfer.* Int. J Mass Spectrom., 2004. **232**(1): p. 79-82.
14. R. N. Compton and P. W. Reinhardt, *Collisional ionization between fast alkali atoms and selected hexafluoride molecules.* J. Chem. Phys., 1978. **68**: p. 2023.

Chapter 4
Recombination

4.1 Introduction

In this part collisional charge exchange of projectile dications with neutral target gases as described by Reaction R1.5 was examined. In particular it was examined whether projectile monocations formed by non-dissociative charge exchange were sufficiently stable to be detected. Fragmentation patterns following collision of dications with neutral target gases were also investigated.

4.2 Experimental program

The experiments are divided into three classes according to their types of compounds. The three classes of compounds are systems containing σ-bonds, π-bonds, and electrostatic bonds. The last class corresponds to complexes of metal atoms with non-metallic closed shell ligands. The distinction was found useful as it can explain differences in reactivity. Systems with σ-bonds have the strongest anti-bonding bond strengths and dissociation energies of intermediate magnitude. Systems with π-bonds have intermediate anti-bonding bond strengths and the highest dissociation energies. Finally metal complexes have the anti-bonding orbitals of smallest strengths and the weakest bonds. The systems with strongest anti-bonding bonds should have the largest change in geometry upon reduction. From the above considerations it should be obvious that systems with π-bonds are the most stable upon reduction. However it is unclear how fragile different metal complexes are. MIKE spectra were obtained using the standard experimental conditions described in chapter 2.

4.2.1 Systems with σ-bonds

Sulphur fluorides

Experiments with collision of SF_n^{2+} at low energy were reported by Price *et al*. [1-3]. Those studies took place at low collision energies with the important consequence that nuclear coordinates have time to adapt to the equilibrium position in the electronic state. One of the studies concluded that loss of a neutral F atom is an important process in collision of CF_3^{2+} and $SF_{2\text{-}4}^{2+}$ [2]. Electron impact ionisation of SF_6 produces ions of the type SF_n^+ where n = 1-5 meaning SF_6^+ is absent [4]. The relaxation energy of the SF_5^+ moiety is likely larger than the SF_5^+–F bond dissociation energy and this could explain the absence of SF_6^+ in mass spectra of SF_6.

The heaviest dication produced upon EI of SF_6 was SF_4^{2+} and a mass spectrum arising from its collision with H_2 is shown in Figure 4.1.

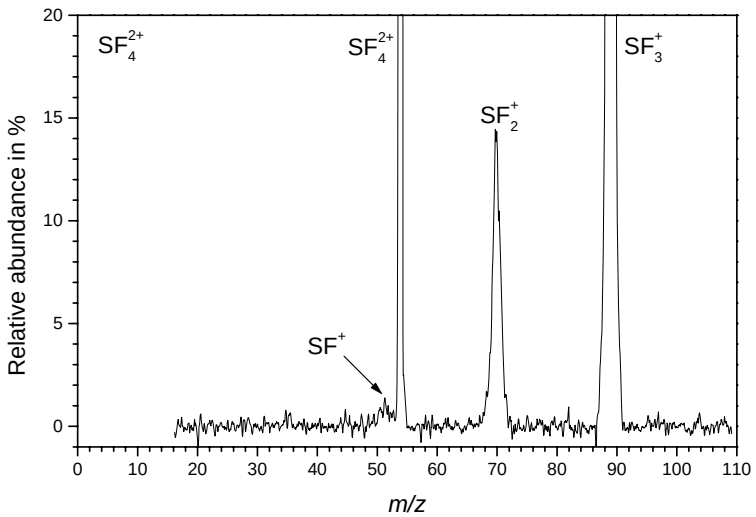

Figure 4.1 MIKE spectrum of SF_4^{2+} upon collision with H_2. The abundances are relative to that of sulphur trifluoride monocation.

The similar spectrum arising from collision of SF_4^{2+} with O_2 is shown in Figure 4.2.

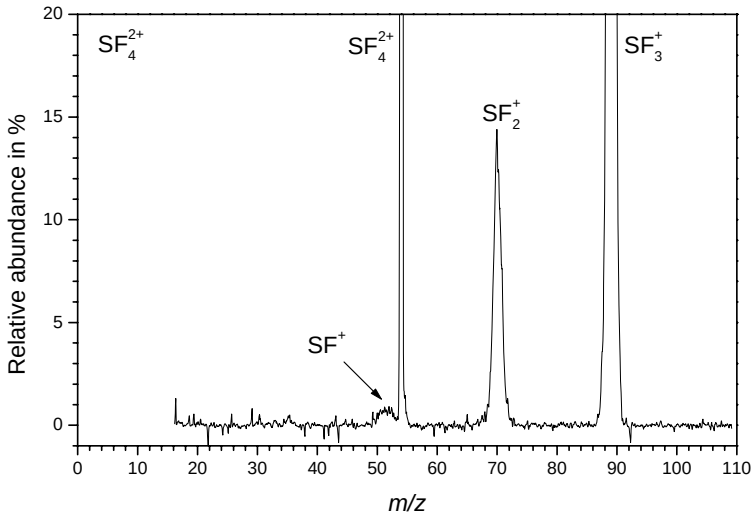

Figure 4.2 MIKE spectrum of SF_4^{2+} upon collision with O_2. The abundances are relative to that of SF_3^+.

There is no significant difference in the products formed by collision with hydrogen and oxygen. SF_3^+ is the largest monocation observed upon collision of SF_4^{2+} with the collision because if SF_4^+ is formed it will not survive long enough to reach the detector. The SF_n^{q+} system was investigated by DFT theory using B3LYP with cc-pVTZ and the results are summarised in Table 4.1. It was found that SF_4^{2+} has the unusually high relaxation energy 3.07 eV. The dissociation energy of SF_4^+ in its equilibrium geometry was found to be 0.64 eV which is low but not as low as a reported value of 0.36 eV found by a thermo chemical study [5]. Vertically formed SF_4^+ will always decay because the relaxation energy is higher than the dissociation energy.

Parent	Ionisation	Relaxation	Dissociation	Experimental [5]
SF_n^+	SF_n^{2+}	SF_n^+	$SF_{n-1}^+ + F$	$SF_{n-1}^+ + F$
n = 4	-17.60	3.07	-0.64	-0.36
n = 3	-21.71	0.85	-4.79	-4.54
n = 2	-20.02	0.20	-3.90	-4.17
n = 1	-21.33	0.11	-4.00	-3.56
Parent	Coulomb exp	Recombination	Dissociation	Decay
SF_n^{2+}	$SF_{n-1}^+ + F^+$	SF_n^+	$SF_{n-1}^{2+} + F$	$SF_{n-1}^+ + F$
n = 4	-0.72	14.53	-4.75	2.43
n = 3	0.08	20.86	-2.25	-3.94
n = 2	-1.57	19.82	-5.22	-3.70
n = 1	-0.35	21.23	-5.92	-3.89

Table 4.1 Calculated energies released by various reactions of sulphur fluorides. Values are calculated using B3LYP with cc-pVTZ and shown in eV. Relaxation is the difference between vertical recombination of its precursor and adiabatic ionisation of the ion. The last column contains experimental dissociation energies and energies released by dissociation of vertically formed monocations.

The equilibrium geometries of the SF_n^{2+} and SF_n^+ were calculated. The results are shown in Table 4.2. SF_4^{2+} has a large geometry change upon reduction which is consistent with the large relaxation energy of SF_4^+.

SF_n^{2+}	Symmetry	Angle (F-S-F)	Distance (Å)
n = 4	T_d	109	1.459
n = 3	C_{3v}	110	1.482
n = 2	C_{2v}	105	1.465
n = 1	-	-	1.458
SF_n^{+}	Symmetry	Angle (F-S-F)	Distance (Å)
n = 4	C_{2v}	103	1.515
n = 4	C_{2v}	160	1.594
n = 3	C_{3v}	100	1.525
n = 2	C_{2v}	102	1.527
n = 1	-	-	1.524

Table 4.2 Symmetries, angles, and S-F distances of SF_n^{2+} and SF_n^{+} ions. Two distinct positions of F atoms are displayed for SF_4^{+}.

The second biggest dication produced was SF_3^{2+} and its spectrum upon collision with O_2 is shown in Figure 4.3.

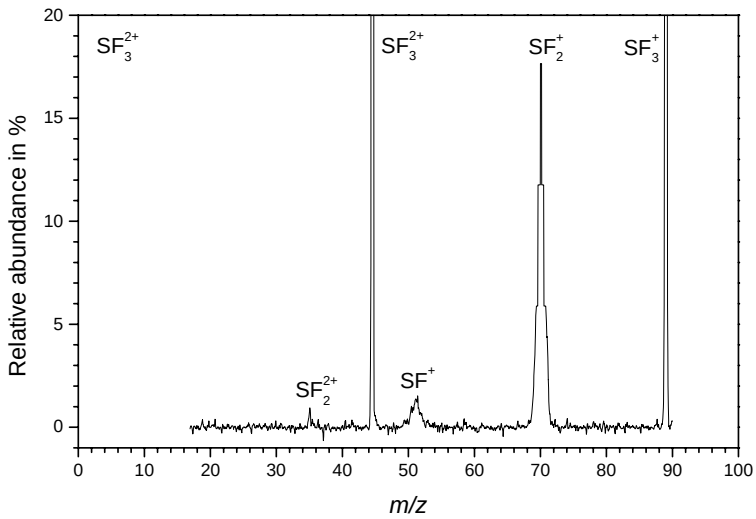

Figure 4.3 MIKE spectrum of SF_3^{2+} upon collision with O_2. The abundances are relative to that of SF_3^{+}.

In low energy collisions it was found that upon collision many SF_n^{2+} ions produces smaller dications by loss of F atoms [2]. In contrast at high collision energies only SF_3^{2+} produces smaller dications and the only product dication is SF_2^{2+}. The reaction is helped along by the fact that SF_3^{2+} is a radical species producing an atomic radical and a closed shell dication upon dissociation. This dramatically influences the dissociation energy which is calculated to be only 2.25 eV in contrast with that of $SF_4^{2+} \rightarrow SF_3^{2+} + F$ which is 4.75 eV. Dissociation of the last two members of the series SF_n^{2+} namely SF_2^{+} and SF_2^{2+} by F loss are both calculated to require more than 5 eV.

Symmetric carbon halides

Collision of CF_2^{2+} was investigated by Price *et al*. [1, 2, 6], Mathur *et al*. [7], and Herman *et al*. [8, 9]. CF_2^{2+} was investigated theoretically by Hrusak *et al*. [10, 11]. Collision of CF_3^{2+} was investigated by Price *et al*. [1, 2, 12-15] and CF_3^{2+} was investigated theoretically by Hrusak *et al*. [16]. Fragmentation of CF_3^{2+} can occur to produce CF_2^{2+} but no other dications are produced and no other CF_n^{2+} dications react by neutral loss [2]. The same study concluded that $CF_{1\text{-}3}^{2+}$ react to produce $CF_{1\text{-}3}^{+}$ without fragmentation and $CF_{0\text{-}2}^{+}$ by loss of one or two F atoms. Hrusak found dissociation of CF_2^{2+} into ground state CF^+ and F^+ to be spin forbidden but releasing 0.09 eV. Singlet and triplet curves cross at 1.85 Å and the associated barrier is calculated to be approximately 5 eV. The C-F bond distance in the linear CF_2^{2+} ion is 1.156 Å [11]. For the CF_3^{2+} ion the D_{3h} symmetry is a minimum structure at the HF theory but a saddle point at higher level theories where the ion is of C_{2v} symmetry. A core is formed with C-F distances of 1.186 Å and a 162° F-C-F angle while the remaining stretched C-F bond is 1.552 Å.

This study used a methane analogue to generate carbon fluoride dications. The chosen precursor gas was CCl_2F_2. CF_2^{2+} was selected and collided with O_2. The spectrum is displayed in Figure 4.4.

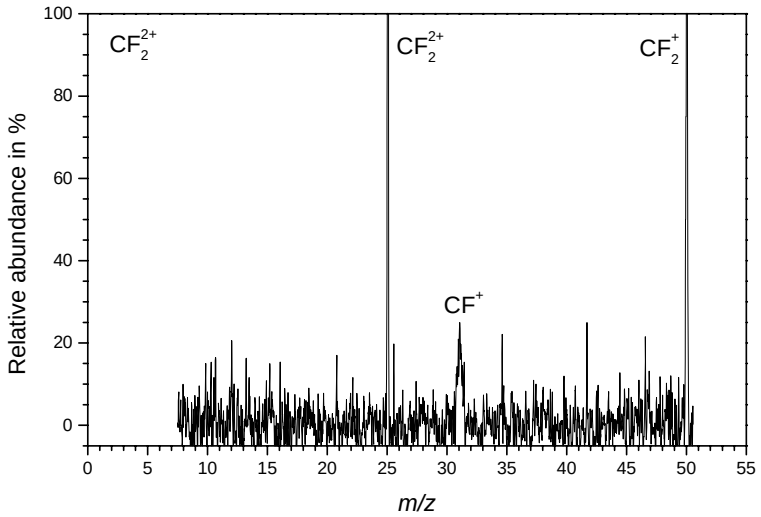

Figure 4.4 MIKE spectrum of CF_2^{2+} upon collision with O_2. The abundances are relative to that of CF_2^+.

The spectrum of CF_2^{2+} upon collision with H_2 was less noisy than obtained upon collision of CF_2^{2+} with O_2 but it has the same features. It is interesting that CF_2^{2+} can undergo non-dissociative reduction in contrast to SF_4^{2+}. Both are dications with no lone electrons placed on the central atom. The fragmentation of SF_4^+ was enabled by the large relaxation energy and the low dissociation energy which was 0.36 eV [5]. The calculated relaxation energy of CF_2^+ was 3.15 eV arising from the significant geometry change in the linear CF_2^{2+} ion [11] and the calculated dissociation energy of the relaxed ion is 3.48 eV according to Appendix B. The FCF angle of CF_2^+ is

expected to be about 120° by VSEPR theory [17]. VSEPR theory describes the geometries of molecules of second row elements well because their p orbitals are pure in the sense they are not affected by core p orbitals. CCl_2^{2+} was also subjected to collision with H_2 and O_2 and the resulting MIKE spectra were obtained. Those spectra were very similar to those following collision of CF_2^{2+} with H_2 and O_2 in terms of features and interpretation.

Asymmetric carbon halides

Collision of $CHCl^{2+}$ with D_2 and Ar with the centre of mass collision energies 1.5 eV for D_2 and 18 eV for Ar has been investigated [18]. It was found that ions formed by protonation of the reactant gas dominated over those formed by charge exchange. Calculations have been performed on $CHCl^{2+}$ and it was found to be linear [19].

$CClF^{2+}$ produced upon ionisation of CF_2Cl_2 was collided with O_2. The resulting spectrum is shown in Figure 4.5.

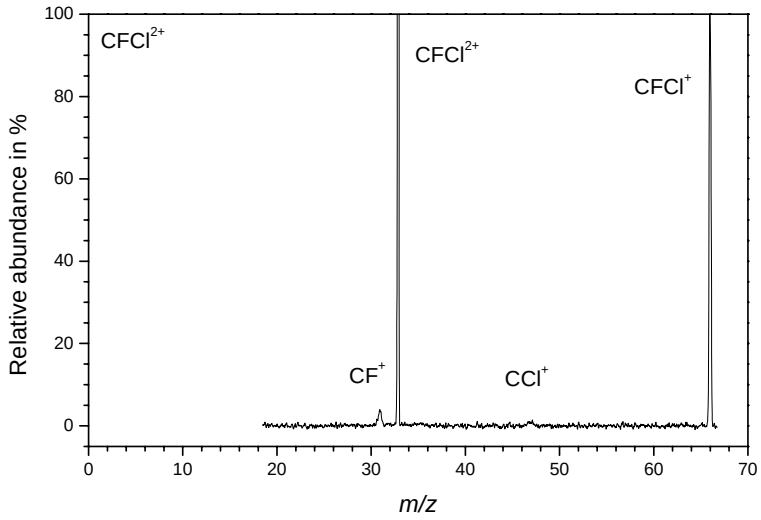

Figure 4.5 MIKE spectrum of $CClF^{2+}$ upon collision with O_2. The abundances are relative to that of $CClF^{+}$.

It is not surprising that C-F bonds are stronger than C-Cl bonds in this dication. In CCl_2F_2 one bond involving fluorine is stronger than one bond involving chlorine. The BDE of F–CCl_2F is 4.8 ± 0.1eV and the BDE of Cl–$CClF_2$ is 3.6 ± 0.1 eV [20].

4.2.2 Systems with π-bonds

Furan

The structure of furan is completely different from that of systems consisting of single bonds. The HOMO orbital has non-bonding character and the HOMO-1 bonding character. Both orbitals are delocalised in the pi system of the aromatic ring. Consequently there is very little change in the geometry of any individual bond when furan becomes ionised or doubly ionised.

From an experimental viewpoint furan is a nice system because although is has an even mass, none of its possible fragment ions has the same mass to charge ratio as its unfragmented dication. The mass of furan is 68 so the apparent mass of its dication is 34 amu. The heaviest possible fragment ion containing two heavy atoms formed by fragmentation of furan is CH_4O^+ with the mass 32 amu and the lightest fragment ion with three heavy atoms is C_3^+ with the mass 36 amu. Furan^{2+} was collided with O_2 and the spectrum obtained is displayed in Figure 4.6.

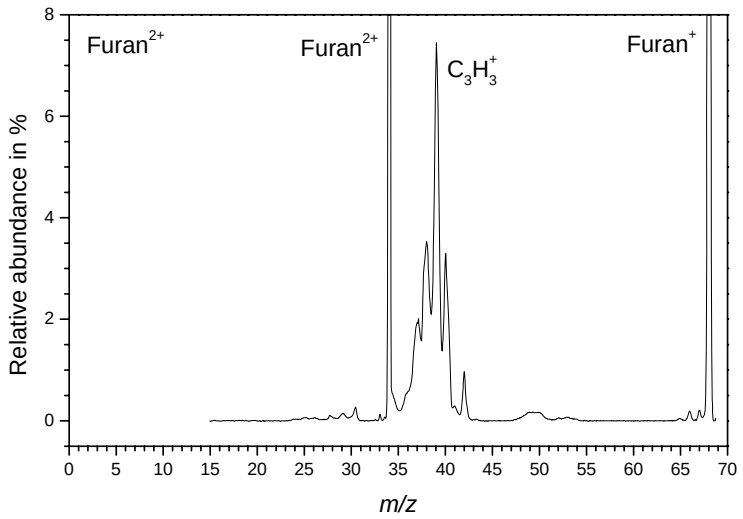

Figure 4.6 MIKE spectrum of $C_4H_4O^{2+}$ upon collision with O_2. The abundances are relative to that of furan$^+$.

The spectrum is strongly dominated by non-dissociative reduction but the spectrum of fragments resemble the spectrum given in the NIST chemistry webbook [4]. Only one hydrogen atom may be lost in fragments of the type $C_4H_nO^+$ in the NIST EI spectrum whereas up to three may be lost in the collision spectrum. In both CID and EI spectra fragments formed by loss of two heavy atoms are dominant with mass 39 being the

most abundant and only small abundances are formed of fragments with two or four heavy atoms. Also bromo-benzene was double ionised producing $C_6H_5Br^{2+}$ which was collided with O_2 and H_2. Non-dissociative reduction dominates the MIKE spectrum which contains singly charged fragment ions separated by approximately 13 mass units in practically the whole mass range.

Trifluoropropene

Not all pi bonded systems investigated in this thesis are cyclic aromatic systems. The other type is linear. Trifluoropropene has the most complex structure of all the pi-bonded non-aromatic systems examined. The isomer examined 1,1,1 trifluoropropene has a three fold rotation axis. $CF_3C_2H^{2+}$ was produced upon electron impact on trifluoropropene by loss of two hydrogen atoms. Unfortunately the signal was very low when the dication was collided with O_2 so the resulting MIKE spectrum was noisy and unfit for presentation. Instead the spectrum where $CF_3C_2H^{2+}$ is collided with H_2 is shown as Figure 4.7.

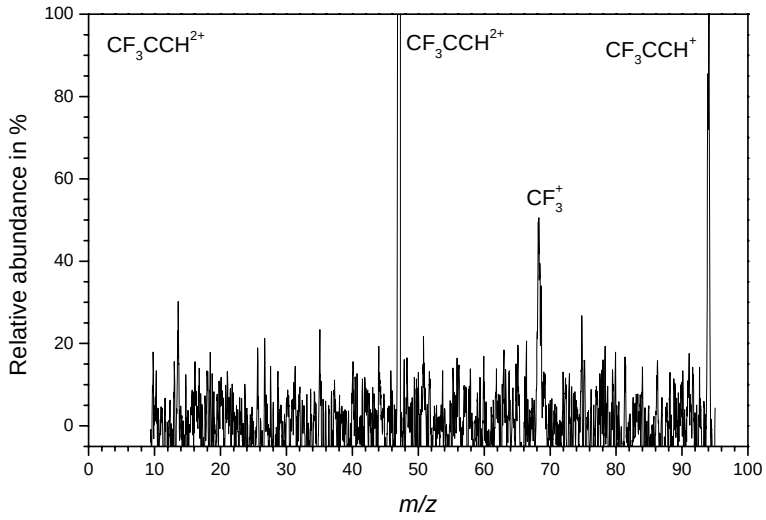

Figure 4.7 MIKE spectrum of $CF_3C_2H^{2+}$ upon collision with H_2. The abundances are relative to that of $CF_3C_2H^{2+}$.

The MS(EI) spectrum of CF_3C_2H is available from NIST [4]. A summary of abundances in EI spectrum and in MIKE spectrum upon collision with H_2 is displayed in Table 4.3 alongside results from calculations.

Ion	H_2	EI	Ion	Symmetry	Neutral	Symmetry	Energy
M^+	100	100					eV
CF_3CC^+	-	8	CF_3CC^+	C_s	H	K_h	4.3
CF_2CCH^+	-	74	CF_2CCH^+	C_{2v}	F	K_h	0.0
CF_3^+	51	23	CF_3^+	D_{3h}	CCH	$C_{\infty v}$	1.3
CCH^+	-	7	CCH^+	C_s	CF_3	C_{3v}	3.5
F^+	-	1	F^+	K_h	CF_2CCH	C_s	9.0
H^+	-	-	H^+	K_h	CF_3CC	C_s	6.4

Table 4.3 Abundances in MS and calculated energies of fragment ions from CF_3CCH. Calculations were CCSD using 6-31G* and the relative energies of different fragmentation channels are shown in eV. The CC moiety of neutral CCH and CF_3CC is $^2\Sigma^+$ and their charged counterparts are $^3\Pi$. The only other triplet is F^+ and all the neutral fragments are doublets.

It was attempted to optimise the geometry of CF_3CCH^{2+} using the *ab initio* methods HF, MP2, MP3, and CCSD. The starting geometry was that of neutral CF_3CCH but unfortunately the dication always dissociated into CF_3^+ and CCH^+. CF_3CCH^{2+} could be optimised using B3LYP which were used with 6-31G because convergence issues arose with larger basis sets. The optimised structure of CF_3CCH^{2+} was C_{3v} symmetric with both electrons removed from the unsaturated bonds in neutral CF_3CCH. Cleavage of a σ-bond in CF_3CCH^+ can lead to six different ions as shown in Table 5.3. It is observed that fragment ions in MS(EI) of CF_3CCH are abundant if their formation is energetically favourable indicating a statistical decay. In contrast fragmentation resulting from collision of CF_3CCH^{2+} exclusively leads to CF_3^+. Calculations using CCSD with 6-31G* reveal formation of CF_2CCH^+ is the lowest energy fragmentation path followed by CF_3^+ which requires 1.3 eV more. CF_3CCH^{2+} has a stretched CF_3-CCH bond as can be concluded by its dissociation into CF_3^+ and CCH^+ during geometry optimisation with *ab initio* methods. The lowest energy orbitals in CF_3CCH^{2+} are presumably the π-bonds from which ionisation has taken place as well as the σ* orbital of the stretched CF_3-CCH bond. Recombination to the π-bonds will reduce the bond distance of the $CF_3C{\equiv}CH$ bond which in turn increases the length of the CF_3-CCH bond. Recombination to the σ* bond will directly increase the CF_3-CCH distance so both these processes favour dissociation of the CF_3-CCH bond. The absence of any CCH^+ ions however is not understood as the energy difference between formation of CF_3^+ and CCH^+ is rather small.

Carbon dioxide type dications

Not all pi bonded systems investigated in this thesis are cyclic aromatic systems. The other type is linear. Trifluoropropyne was linear aside from the F atoms but the other

systems investigated were either linear triatomic or diatomic. Carbon dioxide is a typical triatomic system.

CO_2^{2+} produced by electron impact ionisation was subjected to recombination using free electrons of tuneable energy [21]. The energy available was so large that all dications fragmented upon recombination. Collision of CO_2^{2+} and OCS^{2+} with noble gases at 49 eV laboratory energy was examined [22]. It was found that collision with H and Ne gave almost exclusively collision induced dissociation while collision with Ar, Kr, and Xe gave predominantly charge transfer. A similar study investigated charge transfer between CO_2^{2+} and Ne or Ar at centre of mass collision energies between 3 and 10 eV [23]. The predominant reaction with Ar was of the $^3\Sigma_g^-$ ground state leading to excited states of CO_2^+ A $^2\Pi_u$ and B $^2\Sigma_u^+$. The predominant reaction of CO_2^{2+} with Ne was of $^1\Sigma_g^+$ leading to the ground state $^2\Sigma_g$. Other excited states of CO_2^{2+} were less reactive but also lead to the ground state of CO_2^+. Dications CO_2^{2+} and OCS^{2+} were collided with Xe, D_2, N_2, and NO at 30 eV in the laboratory frame [2]. Charge exchange could lead to simple products CO_2^+ and OCS^+ or to products XeO^+, DCO_2^+, DCO^+, OD^+, and SD^+ involving new bonds. Charge exchange both by electron transfer and formation of new bonds could lead to fragmentation forming neutral fragments. Translational spectroscopy was carried out on CO_2^{2+}, OCS^{2+}, and CS_2^{2+} [24]. Theoretical studies on states of dications of CO_2^{2+}, OCS^{2+}, and CS_2^{2+} as well as their formation by collision H^+ with their neutral precursors giving H^- were carried out [25]. CO_2^{2+} and OCS^{2+} were collided with He and Xe and the abundance of fragment ions were no more than 5 % of intact monocations [26].

CO_2^{2+}, OCS^{2+}, and CS_2^{2+} were subjected to collision with O_2 and their resulting MIKE spectra are shown in Figure 4.8.

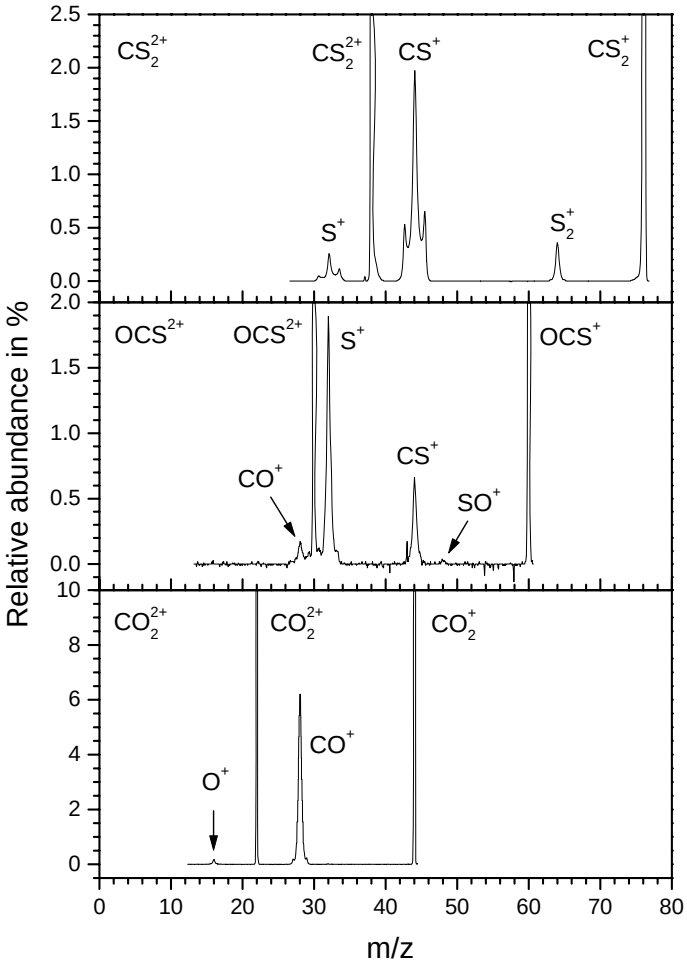

Figure 4.8 MIKE spectra of CO_2^{2+} OCS^{2+}, and CS_2^{2+} upon collision with O_2. The abundances are relative to those of CO_2^+, OCS^+, and CS_2^+.

CO_2 like systems have two degenerate non-bonding HOMO orbitals making the geometries of their corresponding monocations and dications close to that of the neutrals. By far the most abundant product ions formed upon collision of CO_2^{2+},

OCS^{2+}, and CS_2^{2+} with H_2 and O_2 are CO_2^+, OCS^+, and CS_2^+. The most abundant fragment ions are formed by loss of either an O atom or an S atom. The most abundant fragment ions formed from the symmetric dications CO_2^{2+} and CS_2^{2+} are CO^+ and CS^+ while OCS^{2+} predominantly gives S^+. In EI spectra of CO_2 O^+ is formed in equal abundance as CO^+ and from CS_2 S^+ is formed in equal abundance as CS^+ [4]. In MIKE spectra detection is more efficient for the heavier product ions and perhaps this can explain why predominantly the heavier CO^+ and CS^+ ions are observed from collision of dications rather than O^+ and S^+. The dominant position of S^+ as a fragment ion from OCS^{2+} is also observed in the EI spectrum of OCS and this can be explained by the energies of processes leading to the different products. The BDE of CO_2 to O and CO is 5.516 ± 0.004 eV while the corresponding BDE in CS_2 is eV 4.5 ± 0.1 eV [20]. These values should be close to those in OCS. The ionisation energies of S, CS, O, and CO are 10.4 eV, 11.3 eV, 13.6 eV, and 14.0 eV respectively [4]. Thus the formation energies of S^+, CS^+, O^+, and CO^+ from OCS should be close to 14.9 eV, 16.8 eV, 18.1 eV, and 18.5 eV respectively. These approximate energies can also explain why CS^+ is the second most abundant fragment ion.

In the spectra of OCS^{2+} and CS_2^{2+} product ions SO^+ and S_2^+ are formed by rearrangement and subsequent fragmentation. While SO^+ is formed with almost vanishing abundance S_2^+ is formed with abundance comparable to that of S^+. It appears to be the ability of sulphur to form hypervalent compounds which facilitates this rearrangement as sulphur in a hypervalent state can simultaneously form strong bonds to both the C atom and the other atom. Neither SO^+ or S_2^+ are formed by EI on OCS or CS_2 [4] and their absence is problematic to explain. Perhaps a reactive phase space or reactive electronic states are exclusively populated by collision of dications.

CS_2^{2+} has a decay channel involving Coulomb explosion giving the ion pair S^+/CS^+ while CO_2^{2+} has a similar decay channel leading to the ion pair O^+/CO^+. The S^+ and CO^+ peaks in the spectrum of OCS^{2+} have broadenings which is probably due to Coulomb explosion. Also the S_2^+ peak in the spectrum of CS_2^{2+} has broadening suggesting Coulomb explosion with C^+ as the corresponding ion. The abundance of the broad part of the S_2^+ peak was larger when the collision gas was H_2. Perhaps a different set of electronic states are formed by collision with H_2 leading to more Coulomb explosion.

Diatomic molecules

CF^{2+}, CO^{2+}, NO^{2+} of this type was examined and the spectrum of CO^{2+} collided with O_2 is shown in Figure 4.9.

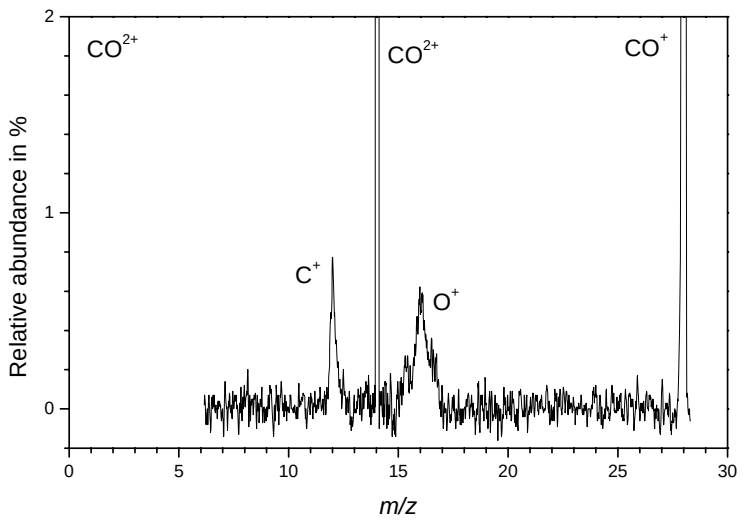

Figure 4.9 MIKE spectrum of CO^{2+} upon collision with O_2. The abundances are relative to that of CO^+.

The most abundant product ion formed is CO^+ while the two atomic fragment ions C^+ and O^+ have rather low abundance. This is also the situation arising from collision of NO^{2+} but for CF^{2+} the atomic fragment ions are completely missing. The bond orders for the ground states of monocations formed in collision are 2.5 and 3 so this can account for the low abundance of fragment ions. The abundance of fragment ions is in all instances observed to be below 1 % of the abundance of the non-dissociated reduced ions. The spectra using H_2 as collision gas were near identical to those using O_2 though this cannot be concluded in the case of NO^{2+} where O_2 was not used. A MIKE spectrum following collision of $ZnAr^{2+}$ with O_2 was also recorded and the only observed fragment ion was Zn^+ with 42 % of the abundance of $ZnAr^+$. This means dissociation energies matter as the dissociation energy of $ZnAr^+$ is much smaller than those of CO^+, NO^+, and CF^+.

4.2.3 Electrostatic bound systems

Zinc argon complexes

Systems bound with single or double bonds have considerable dissociation energies. This is in contrast with metal ion complex systems where for instance $ZnAr^+$ have a bond order of one half. The half bond is even a weak one as the participating orbitals have very different orbital energies. The complex $NaAr^+$ has a dissociation energy of 0.14 eV [27]. $ZnAr^+$ has a reported dissociation energy of 0.32 eV in contrast to MAr^+ for M = Fe, Co, Ni, Cu where the dissociation energy in all cases was reported to be very close to 0.5 eV [28]. The dissociation energy of VAr^+ is reported to be 0.37 eV [29]. The dissociation energy of VAr^+ is reported to be 0.39 eV [30].

Zn-Ar complexes were collided with O_2. The MIKE spectrum following collision of $ZnAr^{2+}$ and $ZnAr_2^{2+}$ with O_2 is shown in Figure 4.10.

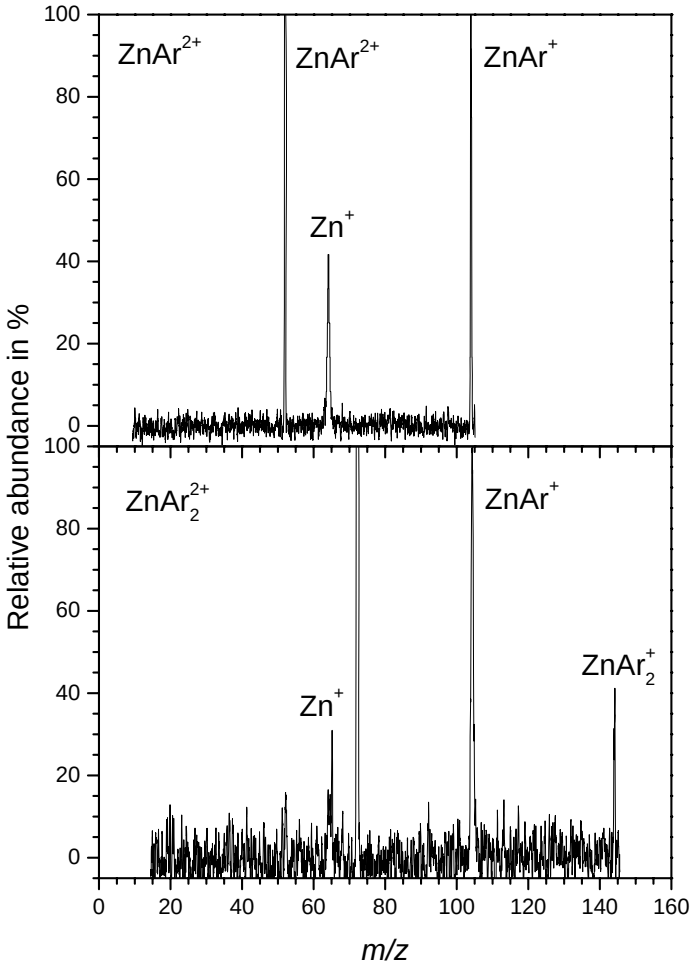

Figure 4.10 MIKE spectra of $ZnAr^{2+}$ and $ZnAr_2^{2+}$ upon collision with O_2. The abundances are relative to the most abundant product ions which in both cases are $ZnAr^+$.

It is observed that the most abundant product ion is $ZnAr^+$. It is no surprise this ion could be formed. Both the monocationic and dicationic potential energy curves of Zn-Ar have deep energy wells. The wells are much deeper than what would be the case if the only interactions were Van der Waal interactions. The dominant product ion from

$ZnAr_2^{2+}$ is $ZnAr^+$. This is because the sequential binding energy of the last bound Ar atom is now lower than the reorganisation energy upon reduction of $ZnAr_2^{2+}$.

MP2 calculations with G3MP2LARGE were performed on zinc argon complexes and they were much more accurate than CCSD calculations with 6-31G*. The second ionisation energy of Zn found by MP2 is 17.57 eV so it compares reasonably well to the literature value of 17.96 eV [20] in contrast the value 16.79 eV was found using CCSD with 6-31G*. The results of MP2 calculations are shown in Table 4.4.

Process	Decay	Relaxation	Ionisation	Dissociation	Dissociation
Reactant	$ZnAr_n^{+*}$	$ZnAr_n^{+*}$	$ZnAr_n^{+}$	$ZnAr_n^{+}$	$ZnAr_n^{2+}$
Products	$ZnAr_{n-1}^{+}$ + Ar	$ZnAr_n^{+}$	$ZnAr_n^{2+}$ + e^-	$ZnAr_{n-1}^{+}$ + Ar	$ZnAr_{n-1}^{2+}$ + Ar
n = 0	-	0	17.57	-	-
n = 1	-0.01	-0.26	15.87	0.25	1.95
n = 2	-0.78	-0.99	14.31	0.21	1.77

Table 4.4 Calculated energies required by various processes of $ZnAr_n^+$ complexes. Energies from MP2 calculations with G3MP2LARGE are shown in eV. Strained reactant monocations denoted $ZnAr_n^{+*}$ are formed by vertical recombination of their precursors.

4.3 Crossing distances

The curve crossing model has been used to calculate at which distance electron transfer occurs. Several values had to be obtained from literature and calculations in order to find the crossing distance. The energies of $H_2(^1\Sigma_g^+)$, $H_2^+(^2\Sigma_g^+)$, and $H_2^+(^2\Sigma_u^+)$ were calculated. The experimentally reported equilibrium value of H_2 was r = 0.7414 Å [20] but a study by A. Ishikawa *et al*. calculated the electronic energies of $H_2^+(^2\Sigma_g^+)$ and $H_2^+(^2\Sigma_u^+)$ at 2 a.u. [31] which is close to the equilibrium distance of H_2^+ $(^2\Sigma_g^+)$. The two-electron system H_2 was calculated using CCSD while the one-electron

system H_2^+ was calculated using HF. All calculations were performed using the basis set G3LARGE. The total energies and the reaction energies for formation of species from neutral ground state H_2 is listed in Table 4.6.

Reaction	$2\ H^+ \rightarrow X$	$H_2 \rightarrow X$	$2\ H^+ \rightarrow X$	$H_2 \rightarrow X$
Distance	0.7414 Å	0.7414 Å	1.0584 Å	1.0584 Å
$X = H_2\ (^1\Sigma_g^+)$	-31.86	0.00	-30.87	0.00
$X = H_2^+(^2\Sigma_g^+)$	-15.49	16.37	-16.39 [31]	14.49
$X = H_2^+(^2\Sigma_u^+)$	-2.77	29.10	-4.55 [31]	26.32

Table 4.5 Potential energies and ionisation energies of H_2. The energies of three states are shown in eV for both the equilibrium distance of H_2 and H_2^+. Values were calculated using CCSD with G3LARGE.

In order to determine the electron transfer distance several calculations using B3LYP have been performed. The basis set used was cc-pVTZ for atoms where that basis set was available but LANL2DZ was used for iodine and 6-31G* for zinc. The necessary values to calculate were the ionisation energies and excitation energies of projectiles and those values are listed in Appendix B. The electron transfer distances are listed in Table 4.7.

H_2^+ state	$^2\Sigma_g^+$	$^2\Sigma_g^+$	$^2\Sigma_g^+$	$^2\Sigma_u^+$	$^2\Sigma_u^+$	$^2\Sigma_u^+$
P^+ state	GS	ES	SF	GS	ES	SF
Projectile	Crossing distance in Å					
SF_4^{2+}	-	-	-	-	-	-
SF_3^{2+}	**3.1**	-	-	-	-	-
SF_2^{2+}	**3.9**	-	-	-	-	-
SF^{2+}	**2.9**	-	-	-	-	-
CF^{2+}	**1.7**	>10	**3.0**	-	-	-
CF_2^{2+}	**8.9**	-	-	-	-	-
$CFCl^{2+}$	**>10**	-	-	-	-	-
CCl_2^{2+}	-	-	-	-	-	-
CFI^{2+}	-	-	-	-	-	-
$Furan^{2+}$	**>10**	-	-	-	-	-
$Ph\text{-}Br^{2+}$	-	-	-	-	-	-
CF_3CCH^{2+}	**5.1**	>10	-	-	-	-
CO_2^{2+}	**2.1**	**4.0**	>10	-	-	-
OCS^{2+}	**5.4**	-	-	-	-	-
CS_2^{2+}	**>10**	-	-	-	-	-
CO^{2+}	**1.5**	**1.8**	**3.7**	-	-	-
NO^{2+}	**1.4**	**4.1**	**2.5**	-	-	**>10**
$ZnAr^{2+}$	-	-	-	-	-	-
$ZnAr_2^{2+}$	-	-	-	-	-	-

Table 4.6 Crossing distances in collisions between projectiles and H_2. All distances are shown in Å. The values used were IE(forming $^2\Sigma_g^+$) = 16.1 eV, IE(forming $^2\Sigma_u^+$) = 28.8 eV, $\alpha(H_2)$ = 0.802 Å^3. The designation of the projectile cation states were GS = ground state, ES = excited state, and SF = spin flip state with states calculated to be stable marked in bold.

It is predicted that no H_2^+ ion is formed in any excited state and some dications should not recombine efficiently. However SF_4^{2+}, CCl_2^{2+}, CFI^{2+}, Bromobenzene^{2+}, CS_2^{2+}, $ZnAr^{2+}$, and $ZnAr_2^{2+}$ are all observed to recombine.

Crossing distances have also been determined for projectiles colliding with O_2 but the excitation energy of O_2 was taken from a study by P. L. Kronebusch *et al*. [32] rather than calculated. The ionisation energies of the ground state of O_2 ($^3\Sigma_g^-$) are 12.07 eV leading to the ground state of O_2^+ ($^2\Pi_g$) and 16.10 eV leading to the first excited state

of O_2^+ ($^4\Pi_u$). Ionisation energies of the ground state to additional low lying excited states of O_2^+ are 17.15 eV ($^2\Pi_u$), 18.17 eV ($^4\Sigma_g^-$), and 20.30 eV ($^2\Sigma_g^-$). The crossing distances are shown in Table 4.8.

O_2^+ state	$^2\Pi_g$	$^2\Pi_g$	$^2\Pi_g$	$^4\Pi_u$	$^4\Pi_u$	$^4\Pi_u$
P^+ state	GS	ES	SF	GS	ES	SF
Projectile	Crossing distance in Å					
SF_4^{2+}	5.9	-	-	-	-	-
SF_3^{2+}	**2.0**	8.4	7.8	**3.2**	-	-
SF_2^{2+}	**2.2**	6.0	-	**4.0**	-	-
SF^{2+}	**1.9**	4.3	-	**3.0**	-	-
CF^{2+}	**1.5**	3.0	**2.0**	**1.8**	>10	**3.1**
CF_2^{2+}	**2.8**	4.1	-	**8.9**	-	-
$CFCl^{2+}$	**3.6**	>10	-	**>10**	-	-
CCl_2^{2+}	**4.7**	-	-	-	-	-
CFI^{2+}	**4.4**	>10	-	-	-	-
$Furan^{2+}$	**3.3**	5.2	-	**>10**	-	-
$Ph\text{-}Br^{2+}$	**6.3**	**>10**	-	-	-	-
CF_3CCH^{2+}	**2.4**	3.5	5.7	**5.1**	>10	-
CO_2^{2+}	**1.7**	**2.2**	3.5	**2.2**	**4.1**	>10
OCS^{2+}	**2.4**	9.2	>10	**5.4**	-	-
CS_2^{2+}	**3.1**	**8.4**	**9.9**	**>10**	-	-
CO^{2+}	**1.4**	**1.6**	**2.1**	**1.6**	**2.0**	**3.7**
NO^{2+}	**1.4**	**2.2**	**1.8**	**1.5**	**4.1**	**2.6**
$ZnAr^{2+}$	**4.0**	-	-	-	-	-
$ZnAr_2^{2+}$	9.6	-	-	-	-	-

Table 4.7 Crossing distances in collisions between projectiles P and O_2. All distances are shown in Å. The values used were IE(forming O_2^+ as $^2\Pi_g$) = 12.1 eV, IE(forming O_2^+ as $^4\Pi_u$) = 16.1 eV, $\alpha(O_2)$ = 1.58 Å^3. The designation of the projectile cation states were GS = ground state, ES = excited state, and SF = spin flip state with states calculated to be stable marked in bold.

In many cases it is predicted that charge exchange with O_2 forming excited states of O_2^+ are efficient. The only case where recombination to form two monocations in their ground states would happen outside the reaction window is for $ZnAr_2^{2+}$. $ZnAr_2^{2+}$ is observed to undergo recombination but in contrast neutral argon atom loss producing $ZnAr^{2+}$ is not observed. This raises the question if the theory is really

applicable in this case. Landau-Zener crossings turn out to be a poor indicator of the presence or absence of recombination. According to LZ theory the projectiles have efficient reaction if their crossings lie within the reaction window of 2-6 Å. Only $ZnAr_2^{2+}$ and SF_4^{2+} do not have crossings within the reaction window leading to non-fragmenting states of the projectile monocation. Formation of SF^+ and CO_2^+ in their ground states is possible within the reaction window only due to formation of O_2^+ in an excited state. Both SF^+ and CO_2^+ are observed experimentally and no excited state of SF^+ is stable so this is an indication that O_2^+ is formed in an excited state following charge exchange between O_2 and SF^{2+}. Table B.7 in Appendix B includes information about which excited states of projectile ions are energetically stable to fragmentation. It is assumed that ground states of CF^+, CO^+, and NO^+ may be formed within the reaction window upon collision with O_2 due to high density of excited states of O_2^+ [32].

4.4 Summary and conclusions

MIKE spectra have been obtained upon collision of molecular dications and dicationic metal complexes with H_2 and O_2. Experimental conditions were standard conditions described in chapter 2. Calculations have been performed in order to aid the interpretation of experimental data. The calculations included both DFT and *ab initio* calculations with several different basis sets. Finally the LZ model has been used to estimate curve crossing distances leading to predictions for reactivity.

Molecular dications CCl_2^{2+} [33] or NH_3^{2+} [34] were collided with several different target gases and a minimum was observed for target gases of intermediate IE in the ratio of product ions formed by dissociative versus non-dissociative recombination.

This finding corresponds well to low energy collision of CO^{2+} with noble gases where collisions predominantly gives Coulomb explosion of CO^{2+} with He, intact CO^{+} with Ar, and dissociative excited states of CO^{+} with Xe [35].

The experiments reveal only tiny differences between spectra taken with O_2 and H_2 as collision gases. Thus no difference arises from the fact that electrons are available at only one electron binding energy in H_2 but at a range of electron binding energies in O_2. It turns out the reaction window in the range 2-6 Å is a poor indicator of the presence or absence of recombination. Observed monocations formed upon collision with O_2 outside the reaction window are bromobenzene^{+} and $ZnAr_2^{+}$ while the corresponding ions for H_2 are CF_2^{+}, $CFCl^{+}$, CCl_2^{+}, CFI^{+}, furan^{+}, bromobenzene^{+}, CS_2^{+}. Formation of $ZnAr^{+}$ and $ZnAr_2^{+}$ was not probed with H_2 experimentally but it would lie outside the reaction window. Excited states formed upon charge exchange with H_2 within the reaction window all have insufficient energy to decay according to Table 4.7. In contrast dissociative excited states of projectile cations are formed within the reaction window under charge exchange with O_2 under formation of O_2^{+} in its $^2\Pi_g$ ground state according to Table 4.8. The presence of these states does not explain fragmentation patterns or probabilities of fragmentation.

It might be conceived that reaction occurs if the projectile passes within a certain distance of the target gas due to collisional activation even if this reaction does not involve charge exchange. Such reactions would be fragmentation of projectile dications either with or without charge separation. Fragmentation without charge separation is observed for SF_3^{2+} which upon collision with H_2 or O_2 both gives SF_2^{2+} in 0.9 % of the abundance of SF_3^{+}. Fragmentation by loss of a neutral fragment is not

observed for any of the other collisions in chapter 4 but is stereotypical for the metal complexes in chapter 5 where the recombination energies of dicationic metal complexes are comparable to IEs of ligands. Fragmentation with charge separation is observed for CO_2, OCS, and CS_2 but is again a minor reaction channel.

Literature reports are that collision of NH_3^{2+} [34] as well as linear hydrocarbons $HCCD^{2+}$ [36] and CH_2CCCH^{2+} [37] all result in atomic hydrogen loss as the dominant product ion for some target gases. This is not observed for the aromatic molecules $C_4H_4O^{2+}$ and $C_6H_5Br^{2+}$ examined in this work. CF_3CCH^{2+} does not fragment forming CF_3CC^+ or CF_2CCH^+ which is the lowest energy fragmentation mode. Instead it exclusively fragments forming CF_3^+ and it is not known why.

Fragmentation patterns and intensities are not well described by LZ theory but rather by the relaxation energy of vertically formed monocations and the lowest BDE of relaxed monocations. The lowest BDE minus the relaxation energy is here called the decay energy and it ranges from -2.40 eV for SF_4^+ to 11.15 eV for NO^+. Dissociative recombination becomes less important relative to non-dissociative recombination as the decay energy increases. Contrary to LZ theory charge transfer reactions releasing too little energy to lie in the reaction window rarely give the reported fragmentation of projectiles but rather charge exchange with the target gas. Charge transfer reactions releasing too much energy to lie in the reaction window primarily give non-dissociative recombination. Reports are that fragmentation should be extensive for such collisions due to formation of excited states of projectile monocations.

4.5 References

1. S. D. Price, M. Manning, and S. R. Leone, *Collision-induced neutral loss reactions of molecular dications.* Chem. Phys. Lett., 1993. **214**: p. 553.
2. S. D. Price, M. Manning, and S. R. Leone, *Bond-forming reactions of gas-phase molecular dications.* J. Am. Chem. Soc., 1994. **116**: p. 8673.
3. P. W. Burnside and S. D. Price, *Electron transfer and bond-forming reactions following collisions of SF^{2+} with Ar.* Int. J Mass Spectrom., 2006. **249**: p. 279.
4. NIST. *NIST Chemistry WebBook.* [Webpage] [cited; Available from: http://webbook.nist.gov/chemistry/.
5. E. R. Fisher, B. L. Kickel, and P. B. Armentrout, *Collision-induced dissociation and charge transfer reactions of SF_x^+ (x=1–5): Thermochemistry of sulfur fluoride ions and neutrals.* J. Chem. Phys., 1992. **97**: p. 4859.
6. N. Lambert, N. Kaltsoyannis, and S. D. Price, *The bond-forming reaction between CF_2^{2+} and H_2O/D_2O: A computational and experimental study.* J. Chem. Phys., 2003. **119**: p. 1421.
7. O. Abu-Haija, E. Y. Kamber, and D. Mathur, *Low-energy reactions of CF_2^{2+} dications with atoms and molecules.* Chem. Phys. Lett., 2005. **408**: p. 5.
8. J. Zabka and Z. Herman, *Single-electron charge transfer in collisions of CF_2^{++} with Ar and Ne at collision energies 3-5eV.* Czech. J. Phys., 1999. **49**: p. 373.
9. Z. Herman, et al., *Dynamics of chemical and charge transfer reactions of molecular dications: beam scattering and total cross section data on CF_2D^+ (CF_2H^+), CF_2^+, and CF^+ formations in $CF_2^{2+}+D_2(H_2)$ collisions.* Int. J. Mass Spectrom., 1999. **192**: p. 191.
10. J. Hrusak, et al., *Heat of formation of the CF_2^{++} dication: a theoretical estimate.* Int. J. Mass Spectrom., 2000. **201**: p. 269.
11. J. Hrusak, *Some remarks on the stability of the ground and excited electronic states of the CF_2^{++} dication.* Chem. Phys. Lett., 2001. **338**: p. 189.
12. S. D. Price, *Interactions of molecular doubly charged ions with atoms, molecules and photons.* J. Chem. Soc. Faraday Trans. , 1997. **93**: p. 2451.
13. N. Tafadar, N. Kaltsoyannis, and S. D. Price, *Electron-transfer and neutral-loss reactions in collisions of CF_3^{2+} with argon* Int. J Mass Spectrom., 1999. **192**: p. 205.
14. N. Tafadar and S. D. Price, *Bond-forming reactivity between CF_3^{2+} and H_2/D_2.* Int. J. Mass Spectrom., 2003. **223**: p. 547.
15. W. P. Hu, S. M. Harper, and S. D. Price, *The dynamics and kinematics of the electron transfer reactions of CF_3^{2+} with Ar* Mol. Phys., 2005. **103**: p. 1809.
16. J. Hrusak, N. Sandig, and W. Koch, *Structure and stability of the CF_3^{2+} dication.* Int. J. Mass Spectrom., 1999. **187**: p. 701.
17. R. J. Gillespie and I. Hargittai, *The VSEPR model of molecular geometry*. 1991: Boston.
18. J. Roithova, et al., *Reactions of molecular dications: collision energy dependence of integral cross-sections of processes in $CHCl^{2+}$ + Ar, D_2 systems from guided beam studies.* Int. J. Mass Spectrom., 2003. **228**: p. 487.
19. J. Roithova, J. Hrusak, and Z. Herman, *A theoretical study of the ground and excited states of the $CHCl^{2+}$ dication and the $CHCl^+$ cation.* Int. J. Mass Spectrom., 2003. **228**: p. 497.
20. D. R. Lide, *Handbook of Chemistry and Physics*. 85th ed. 2004: CRC Press.
21. K. Seiersen, et al., *Dissociative recombination of the cation and dication of CO_2.* Phys. Rev. A, 2003. **68**: p. 022708.
22. S. D. Price, S. A. Rogers, and S. R. Leone, *Charge-transfer and collision-induced dissociation reactions of OCS^{2+} and CO_2^{2+} with the rare-gases at a laboratory collision energy of 49 eV* J Chem. Phys., 1993. **98**: p. 9455.
23. L. Mrazek, et al., *Charge transfer between CO_2^{2+} and Ar or Ne at collision energies 3-10 eV* Coll. Czech. Chem. Comm., 2003. **68**: p. 178.
24. P. Jonathan, et al., *Translational spectroscopy of the triatomic dications CO_2^{2+}, OCS^{2+} and CS_2^{2+}* Chem. Phys., 1988. **119**: p. 159.
25. P. Millie, et al., *Theoretical and experimental studies of the triatomic doubly charged ions CO_2^{2+}, OCS^{2+}, and CS_2^{2+}.* J Chem. Phys., 1986. **84**: p. 1259.
26. C.J. Reid, J. A. Ballantine, and F. M. Harris, *Dissociative and non-dissociative single-electron capture by CO_2^{2+} and OCS^{2+} from rare-gas atoms.* Int. J. Mass Spectrom. Ion Proc., 1989. **93**: p. 23.

27. B. Rhouma, M. Calvo, and F. Spiegelman, *Solvation of Na^+ in Argon Clusters.* J. Phys. Chem. A, 2006. **110**: p. 5010.
28. T. Bastug, et al., *All-electron relativistic Dirac-Fock-Slater self-consistent-field calculations of the singly charged diatomic transition-metal- (Fe, Co, Ni, Cu, Zn) argon molecules.* Phys Rev. A, 1995. **52**: p. 2734.
29. T. Hayes, et al., *The bond length of VAr^+.* Chem. Phys. Lett., 1998. **287**: p. 22.
30. T. Buthelezi, et al., *The adiabatic binding energy of $NbAr^+$.* Chem. Phys. Lett., 1996. **262**: p. 303.
31. A. Ishikawa, H. Nakashima, and H. Nakatsuji, *Solving the Schrödinger and Dirac equations of hydrogen molecular ion accurately by the free iterative complement interaction method.* J. Chem. Phys., 2008. **128**: p. 124103.
32. P. L. Kronebusch and J. Berkowitz, *Photodissociative ionization in the 21–41 eV region: O_2, N_2, CO, NO, CO_2, H_2O, NH_3, and CH_4.* Int. J. Mass Spectrom. Ion Phys., 1976. **22**: p. 283.
33. B. Leyh and D. Hautot, *Mechanisms of single-electron capture by the dichlorocarbene dication.* J. Am. Soc. Mass Spectrom., 1996. **7**: p. 266.
34. B. Leyh and A. Hoxha, *Reaction window in the single-electron capture by ammonia dications.* Chem. Phys., 1995. **192**: p. 65.
35. S. A. Rogers, S. D. Price, and S. R. Leone, *Charge transfer and collision-induced dissociation reactions of CO^{++} with the rare gases at E_{lab} = 49 eV.* J. Chem. Phys., 1993. **98**: p. 280.
36. R. E. March, J. G. Macmillan, and A. B. Young, *Unimolecular and collision-induced processes of ethyne and ethyne-d_1 dications and charge separation of dications derived from butadiene.* Int. J. Mass Spectrom. Ion Proc., 1988. **82**: p. 177.
37. D. Schroder, et al., *Does ionized diacetylene have a positive proton affinity?* Int. J. Mass Spectrom., 2003. **230**: p. 113.

Chapter 5
Metal halides

5.1 Introduction

Monocationic and dicationic metal complexes were collided with O_2 and the resulting MIKE spectra were recorded. The experimental conditions used to obtain MIKE spectra were in all cases those standard conditions described in Chapter 2. Usually the ligands were methyl halides but few experiments were done with carbon dioxide as ligand. The purpose was to examine the propensity of metal atoms to abstract electronegative atoms from ligands. Few experiments were made by abstraction within the ion source with subsequent characterisation of the resulting ion by CID.

Reaction energies for various reactions were calculated by DFT. Computed geometrical properties of metal complexes are included in Appendix C.

5.2 Experiments on collisional halide abstraction

5.2.1 ML_n^+ complexes

Several MIKE spectra were recorded upon collision of singly charged complexes with O_2. The purpose was to examine whether halide atoms were abstracted by the metal atom producing metal halides according to Reaction R5.1.

$$ML_n^+ \rightarrow MXL_{n-m-1}^+ + R + m\,L \qquad \text{(R5.1)}$$

In Reaction R5.1 M = Metal, L = RX = Ligand, X = halogen atom, and R = organic radical. These abbreviations will be used throughout the chapter especially in tables where space is too limited to write full chemical formulae. Metals used were Mg, Ca, Mn, Cu, and Zn while ligands used were CH_3F and CH_3Cl. Thus R = CH_3 and X = F, Cl. An example of a MIKE spectrum upon collision is displayed in Figure 5.1.

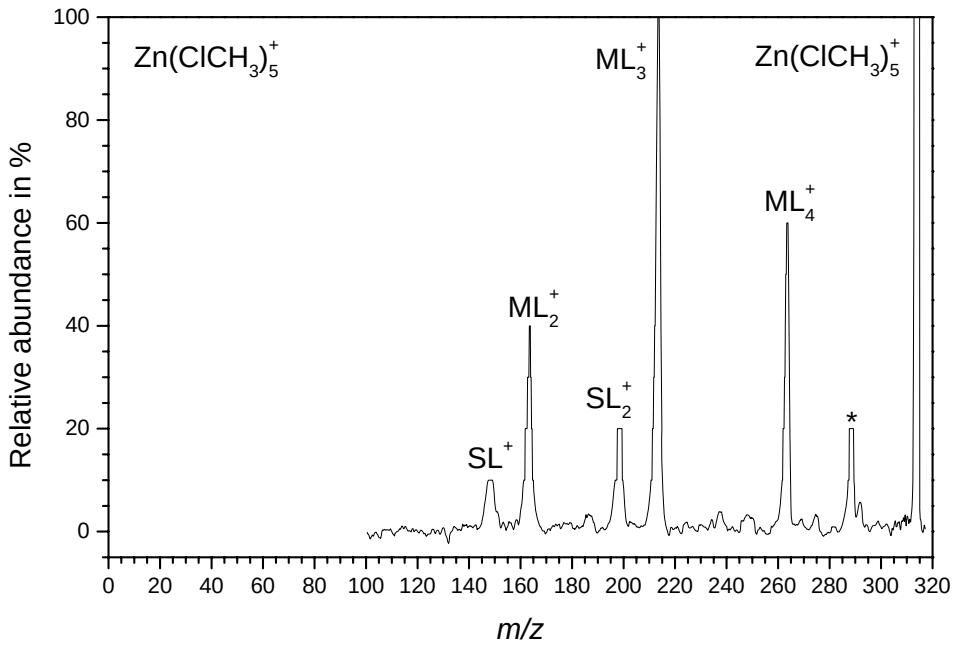

Figure 5.1 MIKE spectrum upon collision of ML_5^+ with O_2. M = Zn, S = ZnCl, and L = CH_3Cl. Peaks denoted by * represent metaclusters 'clusters of clusters'.

The summary of reactions for singly charged complexes with CH_3F ligands is displayed in Table 5.1.

L = RX	Fragmentation				Abstraction			
R = CH_3	$ML_n^+ \rightarrow$				$ML_n^+ \rightarrow$			
X = F	$ML_{n-m}^+ + m\ L$				$MXL_{n-m-1}^+ + m\ L + R$			
Parent	m = 1	m = 2	m = 3	m = 4	m = 1	m = 2	m = 3	m = 4
MgL^+	-	-	-	-	100	-	-	-
MgL_2^+	100	-	-	-	-	-	-	-
MgL_3^+	100	-	-	-	12	12	-	-
MgL_4^+	100	23	-	-	-	-		-
MgL_5^+	100	59	-	-	-	-	18	-
CaL_2^+	100	-	-	-	44	-	-	-
CaL_3^+	100	-	-	-	-	-	-	-
CaL_4^+	49	-	-	-	35	100	-	-
MnL^+	100	-	-	-	-	-	-	-
MnL_2^+	100	-	-	-	-	-	-	-
MnL_3^+	100	55	-	-	-	-	-	-
MnL_4^+	100	50	35	-	-	-	-	-
MnL_5^+	100	67	33	-	-	-	-	-
CuL_3^+	100	26	-	-	-	-	-	-
CuL_4^+	100	80	-	-	-	-	-	-
CuL_5^+	100	57	21	-	-	-	-	-
CuL_6^+	100	46	15	-	-	-	-	-
ZnL^+	100	-	-	-	-	-	-	-
ZnL_2^+	100	-	-	-	-	-	-	-
ZnL_3^+	100	44	-	-	-	-	-	-
ZnL_4^+	100	91	-	-	-	-	-	-
ZnL_5^+	100	89	56	-	-	-	-	-
ZnL_6^+	100	48	78	-	-	-	-	-

Table 5.1 Abundances of product ions collision of ML_n^+ with O_2. M = Mg, Ca, Mn, Cu, and Zn while L = RX for R = CH_3 and X = F. All numbers are in percent of the most abundant product ion.

Alkaline earth metals are the only ones which can abstract fluorine. Furthermore the ability for Ca to abstract fluorine appears slightly larger than that of Mg. There appears to be no preferred number of ligands that facilitates fluorine abstraction.

Metal complexes containing CH_3Cl ligands were collided with O_2 and the summary of reactions is shown in Table 5.2.

L = RX	$ML_n^+ \rightarrow$				$ML_n^+ \rightarrow$			
R = CH_3	$ML_{n-m}^+ + m\ L$				$MXL_{n-m-1}^+ + m\ L + R$			
X = Cl	m = 1	m = 2	m = 3	m = 4	m = 1	m = 2	m = 3	m = 4
MgL_3^+	100	-	-	-	-	-	-	-
MgL_4^+	100	36	-	-	-	-	-	-
MgL_5^+	50	100	50	-	-	-	-	-
MnL_2^+	100	-	-	-	-	-	-	-
MnL_3^+	100	43	-	-	-	-	-	-
MnL_4^+	50	100	23	-	23	30	32	-
MnL_5^+	50	100	80	-	-	-	40	-
ZnL^+	-	-	-	-	100	-	-	-
ZnL_2^+	100	-	-	-	24	7	-	-
ZnL_3^+	100	21	-	-	4	17	2	-
ZnL_4^+	100	92	8	-	-	9	18	-
ZnL_5^+	60	100	40	-	-	-	20	10
ZnL_6^+	97	84	100	29	-	-	-	26

Table 5.2 Abundances of product ions upon collision of ML_n^+ with O_2. M = Mg, Mn, and Zn while L = RX for R = CH_3 and X = Cl. All numbers are in percent of the most abundant product ion.

This time the situation is reversed from that of fluorine containing complexes. Here only Mg did not exhibit halide abstraction of the metals probed. Unfortunately data were not obtained for Ca and Cu. Loss of a single ligand tends not be the most abundant fragmentation channel for the larger complexes. Here Mn appears to give slightly higher yields of halide abstraction than Zn.

5.2.2 ML_n^{2+} complexes

Metal complexes of the type ML_n^{2+} for M = Mg, Ca, Mn, Cu, and Zn while L = CH_3F were collided with O_2 and the spectra were recorded. One such example is shown in Figure 5.2.

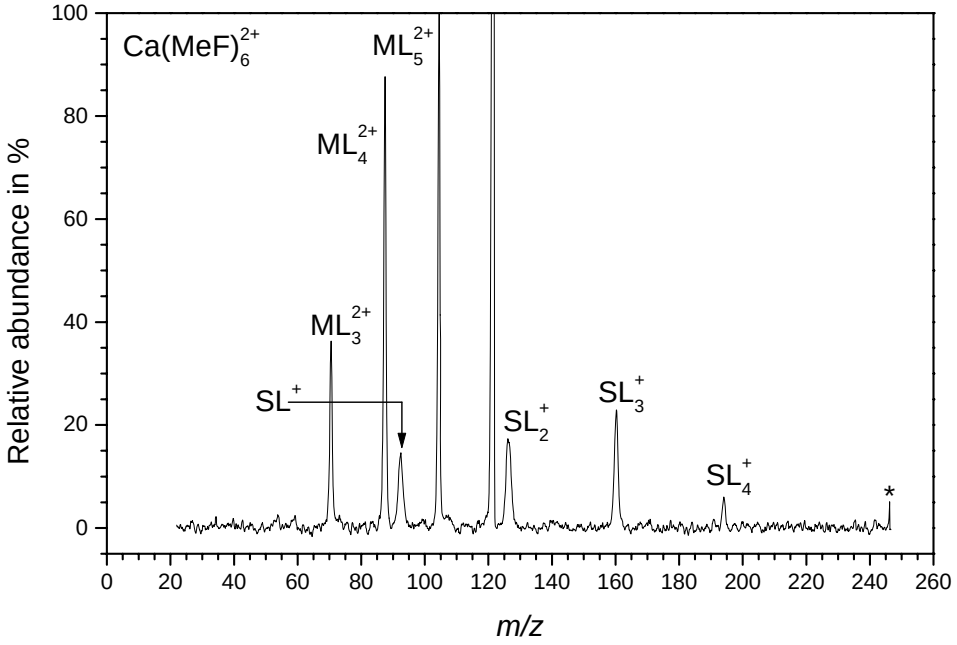

Figure 5.2 MIKE spectrum upon collision of ML_6^{2+} with O_2. M = Ca, S = CaF, and L = CH_3F. Pollution denoted * were present in the spectrum.

Figure 5.2 displays an example of a spectrum with two decay channels both neutral ligand loss and methyl loss following charge reduction. A summary of all reactions examined is given in Table 5.3.

L = RX	Fragmentation			Recombination					Abstraction				
R = CH_3	$ML_n^{2+} \rightarrow$			$ML_n^{2+} \rightarrow$					$ML_n^{2+} \rightarrow$				
X = F	ML_{n-m}^{2+} + m L			ML_{n-m}^{+} + m L					MXL_{n-m-1}^{+} + m L + R				
Parent	m=1	m=2	m=3	m=0	m=1	m=2	m=3	m=4	m=1	m=2	m=3	m=4	m=5
MgL_3^{2+}	8	2	-	-	9	12	-	-	100	68	7	-	-
MgL_4^{2+}	55	23	-	-	-	11	-	-	2	35	100	24	-
MgL_5^{2+}	100	68	-	-	-	3	4	-	2	56	51	11	-
MgL_6^{2+}	89	100	8	-	-	-	-	-	-	13	54	23	8
CaL^{2+}	-	-	-	36	50	-	-	-	100	-	-	-	-
CaL_6^{2+}	100	88	36	5	-	-	-	-	-	6	23	17	15
MnL^{2+}	-	-	-	100	-	-	-	-	-	-	-	-	-
MnL_2^{2+}	-	-	-	100	-	-	-	-	-	-	-	-	-
MnL_3^{2+}	-	-	-	40	-	20	-	-	80	100	20	-	-
MnL_5^{2+}	100	29	-	-	-	-	-	-	-	14	43	14	-
CuL_3^{2+}	100	-	-	-	-	-	-	-	-	-	-	-	-
CuL_4^{2+}	-	-	-	-	-	-	37	-	-	100	46	-	-
CuL_5^{2+}	100	99	-	-	-	-	28	-	-	-	63	-	-
CuL_6^{2+}	100	59	-	-	-	-	-	-	-	-	29	49	-

Table 5.3 Abundances of product ions collision of ML_n^{2+} with O_2. M = Mg, Ca, Mn, and Cu while L = RX where R = CH_3 and X = F. All numbers are in percent of the most abundant product ion.

The ability to abstract fluorine is much higher for doubly charged complexes than for singly charged and this is true both for alkaline earth metals and transition metals. It is remarkable that the five coordinate complex of Ca displays a fragmentation channel with halide abstraction where it loses all its carbon atoms. Many spectra with Ca (n = 2-5) were taken under poor experimental settings where the detector went into saturation. Thus it is not easy to tell exactly how reactive the complexes are. It seems Ca complexes are the most reactive while Cu complexes are the least reactive and this is well explained by the 'IE inducator'.

A few dicationic CH_3Cl containing complexes were collided with O_2 and the reactions are summarised in Table 5.4.

L = RX	Fragmentation		Recombination			Abstraction			
R = CH_3	$ML_n^{2+} \rightarrow$		$ML_n^{2+} \rightarrow$			$ML_n^{2+} \rightarrow$			
X = Cl	ML_{n-m}^{2+} + m L		ML_{n-m}^{+} + m L			MXL_{n-m-1}^{+} + m L + R			
Parent	m = 1	m = 2	m = 1	m = 2	m = 3	m = 1	m = 2	m = 3	m = 4
MgL_3^{2+}	11	-	-	-	-	100	78	-	-
MgL_4^{2+}	73	9	-	-	-	16	100	37	9
ZnL_2^{2+}	-	-	-	-	-	100	-	-	-
ZnL_3^{2+}	-	-	9	30	-	74	100	9	-
ZnL_4^{2+}	38	13	-	11	-	7	100	63	-
ZnL_5^{2+}	100	75	-	8	14	-	24	75	25
ZnL_6^{2+}	36	100	-	-	-	-	-	9	18

Table 5.4 Abundances of product ions upon collision of ML_n^{2+} with O_2. M = Mg and Zn while L = RX where R = CH_3 and X = Cl. All numbers are in percent of the most abundant product ion.

It is again clear that ML_n^{2+} complexes are more prone to halide abstraction than ML_n^{+} complexes. ZnL_5^{2+} and ZnL_6^{2+} are more prone to ligand loss than to halide abstraction. ML_n^{+} ions formed by reduction of ML_n^{2+} are of low abundance like for L = CH_3F so dications tend to decay by halide abstraction rather than simple ligand loss. Dications can have higher internal energy than monocations as their solvation energies are higher and they have shorter equilibrium metal-halide distances. These two effects are believed to be responsible for the higher reactivity of dications.

5.3 Other experiments

The main body of experiments performed in this chapter was collision of metal complexes containing methyl halides. However a few other experiments were done and the conclusions will be presented.

5.3.1 Abstraction of oxygen

Collision experiments were made with a small number of $ML_n^{+/2+}$ where L = CO_2 and OCS. The spectra reveal that metal oxides were formed but no metal sulphides were formed. An example is displayed in Figure 5.3.

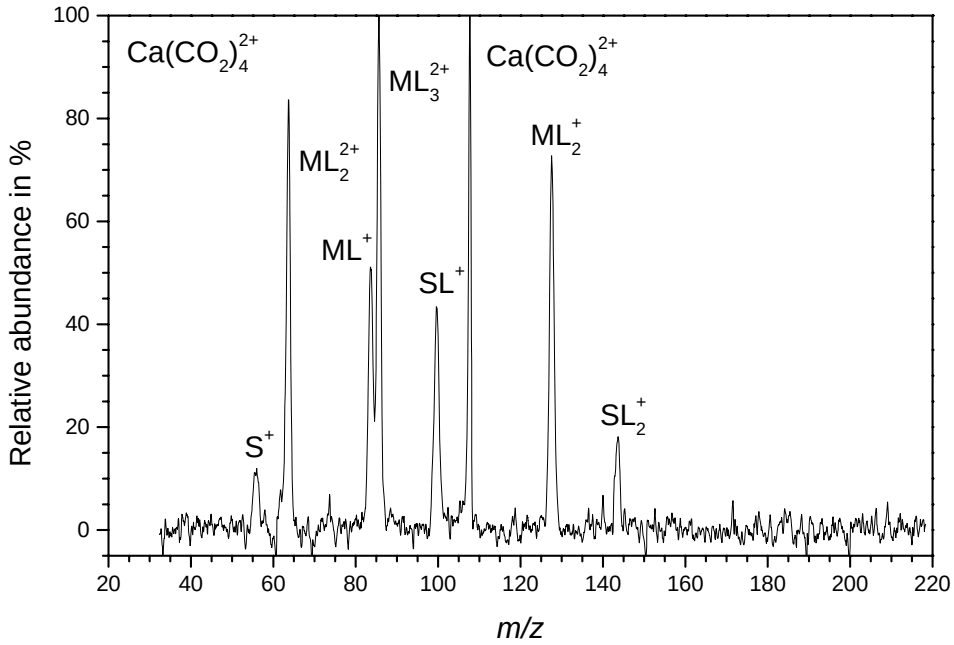

Figure 5.3 MIKE spectrum upon collision of ML_4^{2+} with O_2. M = Ca, S = CaO, and L = CO_2.

5.3.2 Reactions in the ion source

It was possible to make MXL_n^+ ions in the ion source by electron impact ionisation where X = F, Cl, and O while L = CH_3F, CH_3Cl, and CO_2. The MXL_n^+ ions decay predictably upon collision, by L loss and they do not react by further abstraction of electronegative elements. An example of a MIKE spectrum is displayed in Figure 5.4.

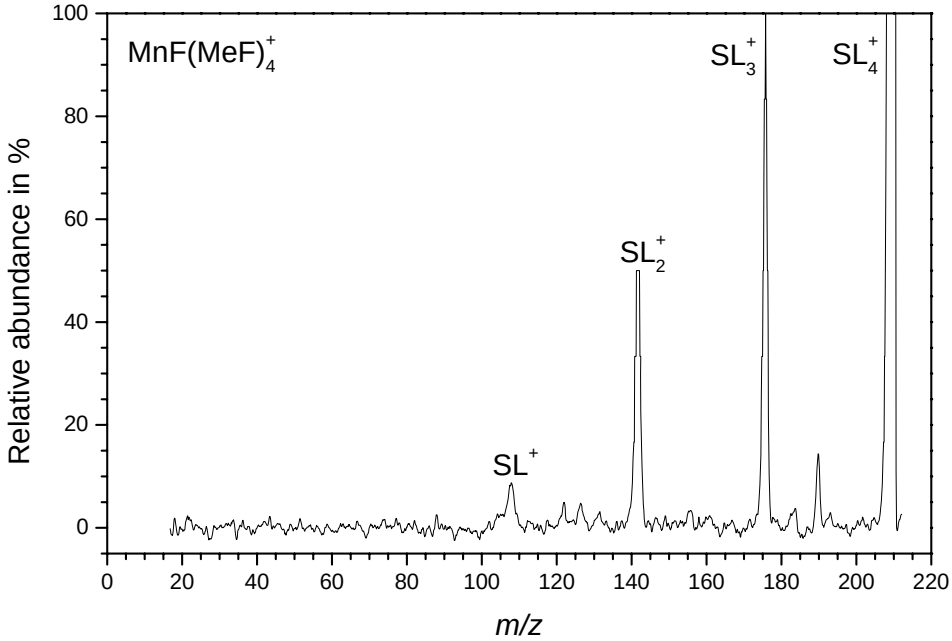

Figure 5.4 MIKE spectrum upon collision of SL_4^+ with O_2. S = MnF and L = CH_3F.

5.4 Tests of computational methods

Theoretical work was done using the B3LYP hybrid functional which is the only method capable of treating open shell species of this size with a reasonable accuracy and speed. The pseudopotential LANL2DZ, the Aldrich basis sets VDZ and VTZ, the Pople basis sets 6-31G and 6-31G*, and the thermo chemical basis set G3MP2LARGE were all examined. A set of tests were made to test the accuracy of the different basis sets in order to see if calculations using them have any predictive power. The results of these tests are all given in Appendix D. The first test was to calculate first and second ionisation energies for the isolated metal atoms by comparing total energies. These values are then compared to experimental values. The

last test was to calculate dissociation energies of MX and RX with subsequent comparison between to literature values.

Ionisation energies can be calculated accurately for any non-metallic or metallic species other than Cu and Cu^+. The most pathological case is the severe underestimation of the ionisation energy of Cu^+ by Pople basis sets. In contrast calculations using any of the other basis sets all give reasonable values for ionisation energies of Cu and Cu^+.

Dissociation energies of molecules could be calculated accurately using any basis set. Unfortunately dissociation energies of metal monohalide salts MX for X = F, Cl were seriously underestimated by the pseudopotential and extremely underestimated by the Aldrich basis sets.

In short the only basis set which always gave accurate results was G3MP2LARGE and the only basis sets which gave sufficiently fast calculations for geometry optimisations was LANL2DZ. Thus geometries were optimised using LANL2DZ and energies were found using G3MP2LARGE on the optimised geometries.

5.5 Halide abstraction

One set of data calculated was reaction energies for halide abstraction. Reactions examined are reactions where halide atoms jump from methyl halides to metals. The reaction energies are displayed in Table 5.5.

L = RX	R = CH_3	X = F	$ML_n^+ \rightarrow MXL_{n-1}^+ + R$		
Metal	n = 1	n = 2	n = 3	n = 4	IE
M = Mg	1.85	0.60	-0.24	-0.98	15.04
M = Ca	0.22	-0.19	-0.70	-1.12	11.87
M = Mn	1.68	0.62	0.12	-0.41	15.64
M = Cu	4.76	4.08	3.12	2.45	20.29
M = Zn	3.13	1.64	0.97	0.40	17.96
L = RX	R = CH_3	X = Cl	$ML_n^+ \rightarrow MXL_{n-1}^+ + R$		
Metal	n = 1	n = 2	n = 3	n = 4	IE
M = Mg	1.47	0.39	-0.42	-0.95	15.04
M = Ca	0.16	-0.30	-0.81	-1.28	11.87
M = Mn	1.27	0.30	-0.32	-0.78	15.64
M = Cu	3.78	3.41	2.86	2.65	20.29
M = Zn	2.32	0.75	0.19	-0.18	17.96

Table 5.5 Energies required for fluorine abstraction in singly charged metal complexes. Geometries were optimised using B3LYP with LANL2DZ. Energies were calculated using B3LYP with G3MP2LARGE and displayed in eV.

The most obvious trend is that the reactions become more energetically favourable as the metal becomes more solvated. Halide abstraction becomes energy releasing for ML_4^+ complexes for most of the metals examined. In the reactions the formal charge on the metals increases from one to two. Thus when n is small in ML_n^+ systems the reaction energies should depend on the second ionisation energy of the metal atoms. In systems with many ligands the second ionisation energy of the metal is less important as their behaviour begins to resemble bulk solution due to solvation effects.

Cu^{2+} has extensive chemistry in water [1] but this is due to a special arrangement with four water molecules in a plane in D_{4h} symmetry in the first solvation shell [2]. These form strong hydrogen bonds to four water molecules in the second solvation shell. Thus in order for a solvent to stabilise the copper dication it should be highly polar and form strong hydrogen bonds. The methyl halides satisfy none of these criteria so they are not expected to stabilise Cu^{2+}. Methyl halides resemble acetonitrile to some

degree as solvent as they solvate by their lone pair and point the methyl group away from the metal. A difference between the compounds is that acetonitrile is a π acid while methyl halides are π bases. Acetonitrile cannot stabilise Cu^{2+} but it strongly solvates Cu^{+} [1]. Methyl halides are thus not expected to stabilise the oxidation state II of Cu and reaction to produce $CuXL_{n-1}^{+}$ remain strongly energy demanding even for n = 4. Although the reaction for formation of CaF^{+} is calculated to require 0.22 eV to occur the reaction is observed in an ICR mass spectrometer [3].

5.6 Dissociation energies of MX and MX^{+}

The dissociation energies of MX were calculated and compared to those of MX^{+}. The calculated values are given in Appendix C. It was found that CuX salts significantly decrease their dissociation energies upon ionisation whereas the dissociation energies of the other MX salts remain essentially unchanged. Cu^{+} is the only closed shell ion and naturally the total number of unpaired electrons does not decrease upon association of Cu^{+} and X in contrast to association of any of the other M^{+} with X. This is indicative that the bond order is ½ for CuX^{+} and 1 for all the other MX^{+} ions. The bond order for all the neutral MX salts is 1. This finding is consistent with the inability of K^{+}, Rb^{+}, and Cs^{+} to abstract F from CH_3F [3] in contrast to the ability of the corresponding neutral alkali metal atoms to abstract F from CH_3F. The dissociation energies of MX and MX^{+} is an indicator of the ability to form each of those substances since the energies released by their formation are BDE(M–X) - BDE(R–X) and BDE(M^{+}–X) - BDE(R–X) respectively. Thus CuF may be formed from Cu + F–SF_5 [4] but CuF^{+} may not be formed from Cu^{+} + F–CH_3 [3].

5.7 Ionisation energies of M and MX

Upon reaction forming metal halides the charge could reside either on the metal halide or on the methyl group. The expectation is that the charge resides on the species with the lowest IE. Formation of molecular ions is reported for successive reaction of Ti^+ and Ln^+ ions with organic halides. Reaction of Ti^+ with halogenated methanes gave halogenated methyl ions [5] while reaction of Ln^+ ions gave $C_5H_{10}^+$ [6]. Cu^+ abstracted Cl^- from $CHCl_3$ forming $CHCl_2^+$ [7]. Formation of molecular cations is very likely occurring by X^- transfer though it is possible that some molecular cations are formed due to collisional ionisation forming free electrons.

Ionisation energies of M and MX were calculated and are shown in Appendix C. The ionisation energies of MX are lower than of CH_3 except for CuX. Thus CuX^+ ions are not expected to be observed in the mass spectrometer following halide abstraction.

5.8 Solvation studies

An isolated metal atom ion has a strongly localised charge so it will easily accept electron density from any nearby molecules. The result is that the BDE of $M–L^+$ by far exceeds that of M–L.

Geometries of ML_n^+, MXL_{n-1}^+, and ML_n^{2+} complexes were optimised by B3LYP with LANL2DZ and energies were found with B3LYP with G3MP2LARGE. Results are displayed in Appendix C. It was found that BDEs decrease with increasing n due to the falling electron density donation from each single ligand. BDEs increase in the following order $L–ML_{n-1}^+ < L–MXL_{n-2}^+ < L–ML_{n-1}^{2+}$ due to the increasing local

charge on the metal atom. The effect is that ML_n^{2+} ions in a mass spectrometer can have higher internal energy than ML_n^{+} ions as the range of possible internal energies extend up to the BDE of the M–L bond. The higher internal energy facilitates production of MXL_{n-1}^{+} from vertically recombined ML_n^{2+} ions relative to collision activated ML_n^{+} ions.

5.9 Bond distances

Internuclear distances between metals and halides were determined for the geometries optimised using B3LYP with LAN2DZ and the results are shown in Appendix C. The M–X distances increase in the following order $X–ML_{n-1}^{+} < L–ML_{n-1}^{2+} < L–MXL_{n-2}^{+} < L–ML_{n-1}^{+}$. Bond lengths increases as n increases and bond lengths are naturally larger for X = Cl than for X = F. Mg based complexes usually have the smallest M–X distances followed by the transition metals while Ca based complexes always have the largest M–X distances. The smaller M–X distances in ML_n^{2+} than in ML_n^{+} provides a minor driving force in overcoming reaction barriers to abstraction.

Geometric properties of complexes such as angles and local symmetries are listed in Appendix C. It is observed that open shell species Mg^{+}, Ca^{+}, Mn^{+}, Cu^{2+}, and Zn^{+} exert more orientation of ligands than Mg^{2+}, Ca^{2+}, Mn^{2+}, Cu^{+}, and Zn^{2+} which tend to give symmetrical arrangements of ligands. This finding is consistent with crystal field theory and ligand field theory.

5.10 Summary and conclusions

Complexes ML_n^+ and ML_n^{2+} were collided with O_2 for L = CH_3F and CH_3Cl while M = Mg, Ca, Mn, Cu, and Zn at 5 kV acceleration voltage under standard conditions described in Chapter 2 and the resulting MIKE spectra were recorded. Few experiments were made for L = CO_2 and OCS and few experiments were made by collision with O_2 of MXL_n^+ and MOL_n^+ formed by electron impact. In order to aid in the interpretation of observed trends DFT calculations were performed. Geometries were optimised using B3LYP with LANL2DZ and energies were found using B3LYP with G3MP2LARGE. Many studies are reported regarding reaction of M^+ with organic halides but this is the first work regarding reaction of ML_n^+ and ML_n^{2+} upon collision and formation of MXL_n^+ by electron impact. The motivation was both fundamental research and formation of MX_n^+ ions for charge permutation collisions.

Complexes of the types ML_n^+ and ML_n^{2+} were both found to abstract halogen atoms forming MXL_{n-m-1}^+. Formation of MF^+ from ML_n^+ was achieved exclusively by Mg and Ca while formation of MCl^+ from ML_n^+ was achieved exclusively by Mn and Zn. In contrast little or no selectivity was observed for the much more reactive ML_n^{2+}. Two properties of ML_n^{2+} are likely to be responsible for its high reactivity. First the M–X distance in complexes increase in the following order $X–ML_{n-1}^+ < L–ML_{n-1}^{2+} < L–MXL_{n-2}^+ < L–ML_{n-1}^+$ according to calculations in Section 5.9 so reaction barriers are initially already partly overcome for ML_n^{2+} complexes. Secondly and more importantly ML_n^{2+} complexes passing through the collision cell can have much more internal energy due to the higher threshold to fragmentation as calculated in Section 5.8. This favours reaction for ML_n^{2+} as high internal energy facilitates penetration of reaction barriers.

Association of a metal atom with a halogen atom increases the formal oxidation state of the metal by one. An important consequence is that the ionisation energy of the reactive species has a large impact on its reactivity. Thus the reactivity of lanthanides Ln^+ with C_6H_5F in an ICR spectrometer to produce LnF^+ is highly correlated with the IEs of the Ln^+ ions providing an 'IE indicator' for reactivity of metal atoms [6]. This is also the case for reaction of 46 atomic cations M^+ with CH_3F where production of MF^+ was observed for main group II and side groups III-V but not for other transition metals nor for alkali metals. This is in reasonable agreement with calculations in Section 5.5 predicting that formation of CaX^+ is slightly energy demanding while formation of other MX^+ ions are strongly energy demanding. Calculations in Section 5.6 indicate that BDEs of MX for remain fairly constant upon ionisation to MX^+ except for CuX where they fall drastically in line with the reported reaction $CuX^+ + L \rightarrow CuL^+ + X$ for L = RX = CH_3Cl [7]. The BDEs of M–X decrease in the series Ca < Mg ≈ Mn ≈ Cu < Zn while the BDEs of $M–X^+$ decrease in the series Ca < Mg ≈ Mn < Zn < Cu. These observations are all in line with the 'IE indicator' for reactivity. It is well known that the IE as indicator of reactivity only works within a single charge state so for instance CaF and CaF^+ have about the same BDE despite Ca and Ca^+ having very different IEs. The IE of a metal ion M^+ decrease upon solvation forming ML_n^+ and this is consistent with Reaction R5.1 becoming increasingly energetically favourable as calculated in Section 5.5. The driving force for abstraction becoming increasingly favourable is that MX^+ is more strongly solvated than M^+ as the solvation energy increases in the series $ML_n^+ < MXL_{n-1}^+ < ML_n^{2+}$. It is assumed that the effect is stronger for solvents with high dielectric constant like water than organic halide solvents like CH_3F and CH_3Cl.

Few experiments were performed where ML_n^+ and ML_n^{2+} for L = CO_2 and OCS were collided with O_2 giving MOL_{n-m-1}^+ ions when L = CO_2 but no reaction when L = OCS. Few experiments were also made by electron impact in the ion source to produce the first MFL_n^+, $MClL_n^+$, and MOL_n^+ ions ever generated by electron impact. These ions were subsequently collided with O_2 but no further abstraction of electronegative atoms was observed. Thus the highest observed oxidation state is II for MXL_n^+ and III for MOL_n^+ complexes.

5.11 References

1. F. A. Cotton, G. Wilkinson, and P. L. Gaus, *Basic Inorganic Chemistry*. 1995: John Wiley & Sons, Inc.
2. A. Berces, et al., *Solvation of Cu^{2+} in Water and Ammonia. Insight from Static and Dynamical Density Functional Theory.* J. Phys. Chem. A, 1999. **103**: p. 9693.
3. X. Zhao, G. K. Koyanagi, and D. K. Bohme, *Reactions of Methyl Fluoride with Atomic Transition-Metal and Main-Group Cations: Gas-Phase Room-Temperature Kinetics and Periodicities in Reactivity.* J. Phys. Chem. A, 2006. **110**: p. 10607.
4. N. R. Walker and M. C. L. Gerry, *Microwave spectra, geometries, and hyperfine constants of OCCuX (X = F, Cl, Br).* Inorg. Chem., 2001. **40**: p. 6158.
5. J. S. Uppal and R. H. Staley, *Gas-phase chemistry of Ti^{+} with halomethanes, alkyl chlorides, chloroethylenes, and chlorobenzene* J. Am. Chem. Soc., 1980. **102**: p. 4144.
6. H. H. Cornehl, G. Hornung, and H. Schwarz, *Gas-Phase Reactivity of Lanthanide Cations with Fluorocarbons: C−F versus C−H and C−C Bond Activation.* J. Am. Chem. Soc., 1996. **118**: p. 9960.
7. R. W. Jones and R. H. Staley, *Gas-phase chemistry of copper(1+) with alkyl chlorides.* J. Am. Chem. Soc., 1980. **102**: p. 3794.

Chapter 6
Conclusions and future work

6.1 Charge stripping

The acceleration voltage in the mass spectrometer was unfortunately too low to allow charge stripping of ML_n^+ complexes with collision gases other than O_2. Thus any systematic experimental study of the effect of the collision gas on the charge stripping efficiencies was not possible. This makes the comparison between theory and experimental data in this work impossible as the theory developed here only deals with the electron trapping species in depth, while treating the electron donor only by its IE.

The σ* orbitals of saturated molecules have been analysed using the NBO package. This is the first time centrifugal barriers of target gases are analysed this way. The sum of s orbital contributions of σ* bonds between two heavy atoms are found to decrease steadily with increasing electronegativity of the two atoms according to the series C_2H_6 (28%) > CH_3F (21%) > CH_3Cl (16%) ≈ SF_6 (16%) > NF_3 (11%) > SF_4 (9%) > Cl_2 (0%) ≈ F_2 (0%). The centrifugal barriers of Cl_2 and F_2 should then be the most effective towards detachment. Unsaturated molecules always have low energy π* orbitals which usually are the LUMO orbitals. Those orbitals due to symmetry have no s orbital contributions so they have efficient centrifugal barriers.

The centrifugal potential has r^{-2} dependence so atomic radii are expected to play a role in the depth of centrifugal barriers. Hence the ability to trap electrons should decrease

in the series S < Cl < C < N < O < F as it reflects falling atomic radii. The effect of atomic radii combined with electron affinities can explain certain trends in reported electron capture cross sections (O_2 > NO > Cl_2 > N_2).

6.2 Charge recombination

High energy collisions of small dications with various target gases have been performed previously but only with a limited number of projectiles. In contrast this work examines collisions of many different projectiles with O_2 and H_2. This work reveals only tiny differences between spectra with the two collision gases. Thus no difference arises from the fact that electrons are available at only one electron binding energy in H_2 but at a range of electron binding energies in O_2.

Contrary to LZ theory and experiments reported in literature the dominant reaction channel in this work is typically non-dissociative recombination for the whole range of reaction energies from -2.40 eV to 11.15 eV. Thus the reaction window where curve crossing lie in the range 2-6 Å is a poor indicator for reactivity.

Fragmentation according to LZ theory depends on formation of dissociative excited states but in this work fragmentation depends on the decay energy i.e. the energy needed to dissociate vertically formed monocations. The decay energy is equal to the dissociation energy of relaxed monocations minus the relaxation energy of vertically formed monocations. Decay energies calculated in Section 4.3 range from -2.40 eV for SF_4^+ to 11.15 eV for NO^+. Dissociative recombination becomes less important relative to non-dissociative recombination as the decay energy increases. For SF_4^{2+} the calculated decay energy is -2.40 eV and non-dissociative recombination is absent

while for $ZnAr_2^{2+}$ it is -0.61 eV and non-dissociative recombination present but not dominant. All other systems have positive decay energies and for them non-dissociative recombination is dominant.

According to LZ theory collisions where charge exchange is insufficiently energy releasing to occur instead results in post collisional fragmentation of projectile dications. Such fragmentations are only rarely observed in this work. The projectiles fragment either with charge separation giving discernible Coulomb explosion or without charge separation giving product dications. Fragmentation without charge separation is observed for SF_3^{2+} which upon collision with H_2 or O_2 both gives SF_2^{2+} in 0.9 % of the abundance of SF_3^+. Fragmentation by loss of a neutral fragment is not observed for any of the other collisions in chapter 4 but is stereotypical for the metal complexes in chapter 5 where the recombination energies of dicationic metal complexes are comparable to IEs of ligands. Coulomb explosion is observed for CO_2, OCS, and CS_2 but it is again a minor reaction channel.

Literature reports are that collision of NH_3^{2+} as well as linear hydrocarbons $HCCD^{2+}$ and CH_2CCCH^{2+} all result in atomic hydrogen loss as the dominant product ion for certain target gases. This is not observed for the aromatic dications $C_4H_4O^{2+}$ and $C_6H_5Br^{2+}$ examined in this work. CF_3CCH^{2+} does not fragment by hydrogen loss or by fluorine loss which is the lowest energy fragmentation mode. Instead it exclusively fragments forming CF_3^+ and it is not known why.

It is clear from the discussion above that many reactions observed in this work are in contradiction with expectations from LZ theory and literature reports.

6.3 Metal halides

Many studies are reported regarding reaction of M^+ with L = RX but this is the first work regarding reaction of ML_n^+ and ML_n^{2+} upon collision and formation of MXL_n^+ by electron impact. The motivation was both fundamental research and formation of MX_n^+ ions for charge permutation collisions.

Complexes of the types ML_n^+ and ML_n^{2+} were both found to abstract halogen atoms forming MXL_{n-m-1}^+. Formation of MF^+ from ML_n^+ was achieved exclusively by Mg and Ca while formation of MCl^+ from ML_n^+ was achieved exclusively by Mn and Zn. In contrast little or no selectivity was observed for the much more reactive ML_n^{2+}. Two properties of ML_n^{2+} are likely to be responsible for its high reactivity. First the MX distance in complexes increase in the following order $X–ML_{n-1}^+ < L–ML_{n-1}^{2+} < L–MXL_{n-2}^+ < L–ML_{n-1}^+$ according to calculations in Section 5.9 so reaction barriers are initially already partly overcome for ML_n^{2+} complexes. Secondly and more importantly ML_n^{2+} complexes passing through the collision cell can have much more internal energy due to the higher threshold to fragmentation as calculated in Section 5.8. This favours reaction for ML_n^{2+} as high internal energy facilitates penetration of reaction barriers.

Calculations in Section 5.5 predict that formation of CaX^+ is slightly energy demanding while formation of other MX^+ ions is strongly energy demanding and this is in agreement with literature reports for reactions of M^+ with CH_3F. Calculations in Section 5.6 indicate that BDEs of MX for remain fairly constant upon ionisation to MX^+ except for CuX where they fall drastically in line with the reported reaction

$CuX^+ + L \rightarrow CuL^+ + X$ for L = RX = CH_3Cl. The BDEs of MX decrease in the series Ca > Mg ≈ Mn ≈ Cu > Zn according to calculations in Section 5.6 while the BDEs of MX^+ decrease in the series Ca > Mg ≈ Mn > Zn > Cu. These observations are all in line with the 'IE indicator' for reactivity. The IE of a metal ion M^+ decrease upon solvation forming ML_n^+ and this is consistent with Reaction 5.1 becoming increasingly energetically favourable as calculated in Section 5.5. The driving force for abstraction becoming increasingly favourable is that MX^+ is more strongly solvated than M^+ as the solvation energy increases in the series $ML_n^+ < MXL_{n-1}^+ < ML_n^{2+}$.

Few experiments were performed where ML_n^+ and ML_n^{2+} for L = CO_2 and OCS were collided with O_2 giving MOL_{n-m-1}^+ ions when L = CO_2 but no reaction when L = OCS. Few experiments were also made by electron impact in the ion source to produce the first MFL_n^+, $MClL_n^+$, and MOL_n^+ ions ever generated by electron impact. These ions were subsequently collided with O_2 but no further abstraction of electronegative atoms was observed. Thus the highest observed oxidation state is II for MXL_n^+ and III for MOL_n^+ complexes.

6.4 Future work

6.4.1 Charge stripping

NRMS experiments could be performed of atomic projectiles colliding with target gases. Simultaneous detection of charged and neutral particles on a phosphorous screen following electric deflection would allow for measurement of cross sections.

Solid state ion sources may give large but fluctuating ion currents of atomic ions necessitating beam intensity corrections which fortunately can be made with this setup. The stripping cross section depends on EA, centrifugal barriers and steric hindrance so the best imaginable neutral charge stripper would be atomic fluorine which is the prime candidate for further research.

It may be desirable to form MX_n^+ and MO_n^+ complexes in order to use them for double charge transfer or neutralisation reionisation experiments with detection in a double focusing mass spectrometer. MX_n complexes are expected to have high EAs while MO_n complexes are expected to have high EAs and LUMO orbitals with efficient centrifugal barriers. Formation of such ions is discussed under metal halides.

Efficient charge strippers are expected to have positive adiabatic EAs enabling formation of stable anions which may be studied by field detachment. The expectation is that efficient charge strippers can survive long time in constant field strength.

6.4.2 Recombination

Dications could be collided with low IE atoms Xe, Zn, Mg, and Na. Electrons are likely only available by reactions forming Xe^+ (^2P), Zn^+ (^2S, ^2D), Mg^+ (^2S), and Na^+ (^1S) so only very few different electron binding energies are available for each element. Dissociative excited states are then more likely to be formed as it becomes increasingly unlikely that enough of the available energy can be converted into translational kinetic energy. Dications could also be collided with He to test whether more post collisional fragmentation of dications will occur relative to reactions by recombination.

High resolution MIKE spectra can be made of ions formed by non-dissociative recombination as this would give energetic information about the states formed.

6.4.3 Metal halides

Considering the comparable binding energies of X and L in CuX^+ and CuL^+ it may be interesting to examine competitive loss of X or L from $CuXL_n^+$ complexes. CuL_n^{2+} complexes may be collided with Na probing formation of triplet states of CuL_n^+ which should decay by halide abstraction under separation of the two unpaired electrons. Complexes of the type $M(H_2O)_nRX^+$ and $M(H_2O)_nRX^{2+}$ may be examined experimentally and theoretically to find out whether the stronger solvent increases reactivity. An increase in reactivity is expected due to the lower IE of ML_n^+ for L = H_2O than for L = CH_3X.

MX_n^+ and MO_n^+ compounds can be formed by chemical reaction but the F, Cl, or O donor molecule would have to have lower BDE than the species examined here. It is possible that the devastating effect of $FeCl_3$ on the turbo pumps was due to its high volatility and corrosivity. MX_2 salts are less hygroscopic and most have boiling points suitable for vaporisation in a high temperature oven with subsequent EI ionisation. It should also be possible to generate MX_n^+ and MO_n^+ ions by laser ablation despite the fact that many metal oxides are refractive.

Appendix A

Charge stripping

H_2 Hydrogen								
PG	Location	Type	H s	H p	H d	H s	H p	H d
$D_{\infty h}$	H-H	σ	50	-	-	50	-	-
$D_{\infty h}$	H-H	σ*	50	-	-	50	-	-
Number	Irrep	Energy	H s	H p	H d	H s	H p	H d
1	A_{1g}	-10.2	50	-	-	50	-	-
2	A_{1u}	0.1	41	9	-	41	9	-
CH_4 Methane								
PG	Location	Type	C s	C p	C d	H s	H p	H d
T_d	C-H	σ	15	46	-	39	-	-
T_d	C-H	σ*	10	29	-	61	-	-
Number	Irrep	Energy	C s	C p	C d	ΣH s	ΣH p	ΣH d
3-5	T_2	-9.3	0	29	-1	74	-2	-
6	A_1	-0.5	-41	-	-	136	5	-
NH_3 Ammonia								
PG	Location	Type	N s	N p	N d	H s	H p	H d
C_{3v}	N	LP	25	75	-	-	-	-
C_{3v}	N-H	σ*	8	23	-	69	-	-
Number	Irrep	Energy	N s	N p	N d	ΣH s	ΣH p	ΣH d
5	A_1	-6.1	11	78	-	4	7	-
6	A_1	-0.8	-13	2	-	107	4	-
H_2O Water								
PG	Location	Type	O s	O p	O d	H s	H p	H d
C_{2v}	O	LP	-	100	-	-	-	-
C_{2v}	O-H	σ*	6	20	-	74	-	-
Number	Irrep	Energy	O s	O p	O d	ΣH s	ΣH p	ΣH d
5	B_2	-7.2	-	95	-	-	5	-
6	A_1	-1.1	-4	4	-	95	5	
HF Hydrofluoric acid								
PG	Location	Type	F s	F p	F d	H s	H p	H d
$C_{\infty v}$	F	LP	-	100	-	-	-	-
$C_{\infty v}$	F-H	σ*	4	18	-	78	-	-
Number	Irrep	Energy	F s	F p	F d	H s	H p	H d
4-5	E_1	-9.6	-	98	-	-	2	-
6	A_1	-1.2	1	2	-	91	6	-

Table A.1 Simple hydrides. First natural bond orbitals then symmetry orbitals are calculated using BLYP with aug-cc-pVDZ. Percentages refer to various orbital contributions to the orbital under investigation. Orbital energies are shown in eV for HOMO and LUMO with LUMO marked in bold. PG = Point Group, Number = Orbital number of energy ranked orbitals, Irrep = Irreducible representation of orbital, Energy = orbital energy eigenvalue, LP = Lone Pair.

C_2H_6 Ethane								
PG	Location	Type	C s	C p	C d	C s	C p	C d
D_{3d}	C-C	σ	14	36	-	14	36	-
D_{3d}	C-C	σ*	14	36	-	14	36	-
Number	Irrep	Energy	ΣC s	ΣC p	ΣC d	ΣH s	ΣH p	ΣH d
8-9	E_g	-8.1	-	23	-	83	-6	-
10	A_{1g}	-0.5	-72	8	1	158	5	-
CH_3F Methyl fluoride								
PG	Location	Type	C s	C p	C d	F s	F p	F d
C_{3v}	F	LP	-	-	-	-	100	-
C_{3v}	C-F	σ*	14	58	-	7	21	-
Number	Irrep	Energy	C s	C p	C d	F s	F p	F d
8-9	E	-8.0	-	9	1	-	65	-
10	A_1	-0.5	1	77	4	-16	8	-
CH_3Cl Methyl chloride								
PG	Location	Type	C s	C p	C d	Cl s	Cl p	Cl d
C_{3v}	Cl	LP	-	-	-	-	100	-
C_{3v}	C-Cl	σ*	10	47	-	6	37	-
Number	Irrep	Energy	C s	C p	C d	Cl s	Cl p	Cl d
12-13	E	-7.0	-	3	1	-	89	-
14	A_1	-1.0	9	29	3	5	27	13
SF_6 Sulphur hexafluoride								
PG	Location	Type	S s	S p	S d	F s	F p	F d
O_h	F	LP	-	-	-	-	100	-
O_h	S-F	σ*	13	40	26	3	18	-
Number	Irrep	Energy	S s	S p	S d	ΣF s	ΣF p	ΣF d
33-35	T_{1g}	-10.3	-	-	-	-	100	-
36	A_{1g}	-5.3	47	-	-	-5	58	-

Table A.2 Electron deficient saturated molecules. First natural bond orbitals then symmetry orbitals are calculated using BLYP with aug-cc-pVDZ. Percentages refer to various orbital contributions to the orbital under investigation. Orbital energies are shown in eV for HOMO and LUMO with LUMO marked in bold. PG = Point Group, Number = Orbital number of energy ranked orbitals, Irrep = Irreducible representation of orbital, Energy = orbital energy eigenvalue, LP = Lone Pair.

F_2 Fluorine								
PG	Location	Type	F s	F p	F d	F s	F p	F d
$D_{\infty h}$	F	LP	-	100	-	-	-	-
$D_{\infty h}$	F-F	σ*	-	50	-	-	50	-
Number	Irrep	Energy	F s	F p	F d	F s	F p	F d
8-9	E_{1g}	-9.6	-	50	-	-	50	-
10	A_{1u}	-6.3	-	49	1	-	49	1
Cl_2 Chlorine								
PG	Location	Type	Cl s	Cl p	Cl d	Cl s	Cl p	Cl d
$D_{\infty h}$	Cl	LP	-	100	-	-	-	-
$D_{\infty h}$	Cl-Cl	σ*	-	50	-	-	50	-
Number	Irrep	Energy	Cl s	Cl p	Cl d	Cl s	Cl p	Cl d
16-17	E_{1g}	-7.3	-	50	-	-	50	-
18	A_{1u}	-4.9	-1	49	2	-1	49	2
NF_3 Nitrogen trifluoride								
PG	Location	Type	N s	N p	N d	F s	F p	F d
C_{3v}	N	LP	70	30	-	-	-	-
C_{3v}	N-F	σ*	7	57	-	4	32	-
Number	Irrep	Energy	N s	N p	N d	F s	F p	F d
17	A_1	-9.0	22	23	-	-2	57	-
18	A_1	-2.6	-	66	3	-2	32	1
SF_4 Sulphur tetrafluoride								
PG	Location	Type	S s	S p	S d	F s	F p	F d
C_{2v}	S	LP	81	19	-	-	-	-
C_{2v}	S-F	σ*	6	63	7	3	21	0
Number	Irrep	Energy	S s	S p	S d	ΣF s	ΣF p	ΣF d
26	A_1	-8.8	16	9	3	-1	73	-
27	B_2	-4.2	-	64	13	-	22	1

Table A.3 Electron rich saturated molecules. First natural bond orbitals then symmetry orbitals are calculated using BLYP with aug-cc-pVDZ. Percentages refer to various orbital contributions to the orbital under investigation. Orbital energies are shown in eV for HOMO and LUMO with LUMO marked in bold. PG = Point Group, Number = Orbital number of energy ranked orbitals, Irrep = Irreducible representation of orbital, Energy = orbital energy eigenvalue, LP = Lone Pair.

C_2H_4 Ethylene								
PG	Location	Type	C s	C p	C d	C s	C p	C d
D_{2h}	C-C	π	-	50	-	-	50	-
D_{2h}	C-C	π*	-	50	-	-	50	-
Number	Irrep	Energy	ΣC s	ΣC p	ΣC d	ΣH s	ΣH p	ΣH d
8	B_{1u}	-6.5	-	95	1	-	4	-
9	B_{2g}	-1.0	-	90	4	-	6	-
CH_2O Formaldehyde								
PG	Location	Type	C s	C p	C d	O s	O p	O d
C_{2v}	O	LP	-	-	-	-	100	-
C_{2v}	C-O	π*	-	65	-	-	35	-
Number	Irrep	Energy	C s	C p	C d	O s	O p	O d
8	B_1	-6.2	-	3	4	-	70	-
9	B_2	-2.7	-	70	2	-	21	-
C_3H_6O Acetone								
PG	Location	Type	C s	C p	C d	O s	O p	O d
C_s	O	LP	-	-	-	-	100	-
C_s	C-O	π*	-	67	-	-	33	-
Number	Irrep	Energy	C s	C p	C d	O s	O p	O d
16	A"	-5.6	-	-2	3	-	74	-
17	A'	-1.7	-	57	1	-	21	-
C_2H_6OS Dimethylsulphoxide								
PG	Location	Type	S s	S p	S d	O s	O p	O d
C_s	O	LP	-	-	-	-	100	-
C_s	S	NL	19	12	69	-	-	-
Number	Irrep	Energy	S s	S p	S d	O s	O p	O d
21	A'	-5.3	7	10	5	-	66	-
22	A'	-0.8	-	77	15	-10	9	-

Table A.4 Isolated double bonds. First natural bond orbitals then symmetry orbitals are calculated using BLYP with aug-cc-pVDZ. Percentages refer to various orbital contributions to the orbital under investigation. Orbital energies are shown in eV for HOMO and LUMO with LUMO marked in bold. PG = Point Group, Number = Orbital number of energy ranked orbitals, Irrep = Irreducible representation of orbital, Energy = orbital energy eigenvalue, LP = Lone Pair, NL = Non-Lewis.

$C_2H_2O_2$ Glyoxal								
PG	Location	Type	C s	C p	C d	O s	O p	O d
C_{2h}	O	LP	-	-	-	-	100	-
C_{2h}	C-O	π^*	-	65	-	-	35	-
Number	Irrep	Energy	ΣC s	ΣC p	ΣC d	ΣO s	ΣO p	ΣO d
15	A_g	-6.3	1	9	5	-	69	-
16	A_u	-4.4	-	54	5	-	40	-
C_5H_4O Cyclopentadienone								
PG	Location	Type	ΣC s	ΣC p	ΣC d	O s	O p	O d
C_{2v}	O	LP	-	-	-	-	100	-
C_{2v}	C-C	π^*	-	100	-	-	-	-
Number	Irrep	Energy	ΣC s	ΣC p	ΣC d	O s	O p	O d
21	B_1	-6.0	2	16	10	-	68	-
22	B_2	-3.8	-	75	5	-	18	-
$C_6H_4O_2$ Para-Quinone								
PG	Location	Type	ΣC s	ΣC p	ΣC d	O s	O p	O d
D_{2h}	O	LP	-	-	-	-	100	-
D_{2h}	C-C	π^*	-	100	-	-	-	-
Number	Irrep	Energy	ΣC s	ΣC p	ΣC d	ΣO s	ΣO p	ΣO d
28	B_{1g}	-6.3	4	12	7	-	69	-
29	B_{2g}	-4.5	-	63	5	-	32	-

Table A.5 Conjugated carbonyl groups. First natural bond orbitals then symmetry orbitals are calculated using BLYP with aug-cc-pVDZ. Percentages refer to various orbital contributions to the orbital under investigation. Orbital energies are shown in eV for HOMO and LUMO with LUMO marked in bold. PG = Point Group, Number = Orbital number of energy ranked orbitals, Irrep = Irreducible representation of orbital, Energy = orbital energy eigenvalue, LP = Lone Pair.

C_6H_6 Benzene								
PG	Location	Type	C s	C p	C d	C s	C p	C d
D_{6h}	C-C	π	-	50	-	-	50	-
D_{6h}	C-C	π*	-	50	-	-	50	-
Number	Irrep	Energy	ΣC s	ΣC p	ΣC d	ΣH s	ΣH p	ΣH d
20-21	E_{1g}	-6.1	-	96	3	-	1	-
22-23	E_{2u}	-1.1	-	89	8	-	3	-
C_6F_6 Perfluorobenzene								
PG	Location	Type	C s	C p	C d	C s	C p	C d
D_{6h}	C-C	π	-	50	-	-	50	-
D_{6h}	C-C	π*	-	50	-	-	50	-
Number	Irrep	Energy	ΣC s	ΣC p	ΣC d	ΣF s	ΣF p	ΣF d
44-45	E_{1g}	-6.8	-	71	4	-	25	-
46	A_{1g}	-2.5	128	26	6	-67	7	-
C_4H_4O Furan								
PG	Location	Type	ΣC s	ΣC p	ΣC d	O s	O p	O d
C_{2v}	O	LP	-	-	-	-	100	-
C_{2v}	C-C	π*	-	100	-	-	-	-
Number	Irrep	Energy	ΣC s	ΣC p	ΣC d	O s	O p	O d
18	A_2	-5.5	-	94	3	-	-	1
19	B_2	-0.9	-	76	5	-	14	-

Table A.6 Aromatic molecules. First natural bond orbitals then symmetry orbitals are calculated using BLYP with aug-cc-pVDZ. Percentages refer to various orbital contributions to the orbital under investigation. Orbital energies are shown in eV for HOMO and LUMO with LUMO marked in bold. PG = Point Group, Number = Orbital number of energy ranked orbitals, Irrep = Irreducible representation of orbital, Energy = orbital energy eigenvalue, LP = Lone Pair.

CF_3NO_2 Perfluoronitromethane								
PG	Location	Type	N s	N p	N d	ΣO s	ΣO p	ΣO d
C_s	O	LP	-	-	-	-	100	-
C_s	N-O	π*	-	57	-	-	43	-
Number	Irrep	Energy	N s	N p	N d	ΣO s	ΣO p	ΣO d
28	A"	-8.0	-	-	2	-	96	-
29	A'	-4.2	-	42	1	-	53	-
SO_3 Sulphur trioxide								
PG	Location	Type	S s	S p	S d	O s	O p	O d
D_{3h}	S-O	π	-	28	1	-	71	-
D_{3h}	S-O	π*	-	70	2	-	28	-
Number	Irrep	Energy	S s	S p	S d	ΣO s	ΣO p	ΣO d
20	A_2'	-8.2	-	-	-	-	100	-
21	A_2"	-4.4	-	50	-	-	51	-1
O_2 Singlet oxygen								
PG	Location	Type	O s	O p	O d	O s	O p	O d
$D_{\infty h}$	O-O	π	-	50	-	-	50	-
$D_{\infty h}$	O-O	π*	-	50	-	-	50	-
Number	Irrep	Energy	ΣO s	ΣO p	ΣO d			
8	B_{2u}	-7.4	-	99	1			
9	B_{3u}	-5.5	-	100	-			
O_3 Ozone								
PG	Location	Type	O s	O p	O d	ΣO s	ΣO p	ΣO d
C_{2v}	O	LP	-	100	-	-	-	-
C_{2v}	O-O	π*	-	-	-	-	100	-
Number	Irrep	Energy	O s	O p	O d	ΣO s	ΣO p	ΣO d
12	A_1	-8.0	7	8	2	-1	84	-
13	B_2	-6.3	-	32	-	-	68	-
SO_2 Sulphur dioxide								
PG	Location	Type	S s	S p	S d	ΣO s	ΣO p	ΣO d
C_{2v}	O	LP	-	-	-	-	99	1
C_{2v}	S-O	π*	-	68	1	-	32	-
Number	Irrep	Energy	S s	S p	S d	ΣO s	ΣO p	ΣO d
16	A_1	-7.9	11	7	9	1	72	-
17	B_2	-5.0	-	53	3	-	44	-

Table A.7 Oxygen group. First natural bond orbitals then symmetry orbitals are calculated using BLYP with aug-cc-pVDZ. Percentages refer to various orbital contributions to the orbital under investigation. Orbital energies are shown in eV for HOMO and LUMO with LUMO marked in bold. PG = Point Group, Number = Orbital number of energy ranked orbitals, Irrep = Irreducible representation of orbital, Energy = orbital energy eigenvalue, LP = Lone Pair.

N_2 Nitrogen								
PG	Location	Type	N s	N p	N d	N s	N p	N d
N_2	N-N	σ	19	31	-	19	31	-
$D_{\infty h}$	N-N	π*	-	50	-	-	50	-
Number	Irrep	Energy	ΣN s	ΣN p	ΣN d			
7	A_{1g}	-10.2	33	66	1			
8-9	E_{1g}	-2.1	-	95	5			
CO Carbon monoxide								
PG	Location	Type	C s	C p	C d	O s	O p	O d
CO	C-O	σ	7	21	-	32	40	1
$C_{\infty v}$	C-O	π*	-	77	-	-	23	-
Number	Irrep	Energy	C s	C p	C d	O s	O p	O d
7	A_1	-9.0	41	39	-	8	11	1
8-9	E_1	-2.1	-	67	4	-	28	1
CO_2 Carbon dioxide								
PG	Location	Type	C s	C p	C d	ΣO s	ΣO p	ΣO d
CO_2	O	LP	-	-	-	-	100	-
$D_{\infty h}$	C-O	π*	-	74	-	-	26	-
Number	Irrep	Energy	C s	C p	C d	ΣO s	ΣO p	ΣO d
10-11	E_{1u}	-8.6	-	-	-	-	100	-
12-13	E_{1g}	-1.0	-	67	-	-	33	-
N_2O Nitrous oxide								
PG	Location	Type	ΣN s	ΣN p	ΣN d	O s	O p	O d
N_2O	O	LP	-	-	-	-	100	-
$C_{\infty v}$	N-N	π*	-	100	-	-	-	-
Number	Irrep	Energy	ΣN s	ΣN p	ΣN d	O s	O p	O d
10-11	E_1	-8.3	-	37	5	-	58	-
12-13	E_1	-2.2	-	86	-	-	13	1
C_2H_2 Acetylene								
PG	Location	Type	ΣC s	ΣC p	ΣC d			
C_2H_2	C-C	π	-	100	-			
$D_{\infty h}$	C-C	π*	-	100	-			
Number	Irrep	Energy	ΣC s	ΣC p	ΣC d	ΣH s	ΣH p	ΣH d
10-11	E_{1u}	-7.0	-	99	-	-	1	-
12-13	E_{1g}	-0.4	-	83	12	-	5	-

Table A.8 Linear Molecules. First natural bond orbitals then symmetry orbitals are calculated using BLYP with aug-cc-pVDZ. Percentages refer to various orbital contributions to the orbital under investigation. Orbital energies are shown in eV for HOMO and LUMO with LUMO marked in bold. PG = Point Group, Number = Orbital number of energy ranked orbitals, Irrep = Irreducible representation of orbital, Energy = orbital energy eigenvalue, LP = Lone Pair.

	KT	KT	ΔSCF	ΔSCF	TT	TT	Literature
Molecule	BLYP	B3LYP	BLYP	B3LYP	BLYP	B3LYP	[1, 2]
O_2	-	5.66	-	2.10	-	1.50	-0.091
O_3	6.29	5.42	1.98	2.21	1.46	2.20	2.10
Quinone	4.52	3.92	1.81	1.88	0.92	1.76	1.86
Cl_2	4.90	3.97	1.40	1.37	0.64	0.97	(1.02)
C_5H_4O	3.81	3.16	0.93	1.01	0.51	0.86	-
SO_2	4.95	4.25	1.26	1.45	0.50	1.24	1.11
SF_6	5.31	3.67	1.90	1.02	0.48	0.78	(1.07)
Glyoxal	4.35	3.54	0.96	1.00	0.23	0.80	(0.62)
SF_4	4.19	3.16	0.66	0.53	0.01	0.31	(1.50)
F_2	6.29	4.49	1.03	0.71	-0.09	0.05	(1.24)
SO_3	4.35	3.54	0.94	0.85	-0.17	0.62	(1.90)
C_6F_6	2.53	1.71	0.27	-1.60	-0.41	-0.14	(0.53)
CF_3NO_2	4.24	3.43	0.47	0.68	-0.42	0.42	-
CH_2O	2.69	1.80	-	-0.59	-1.97	-1.43	-1.5
C_6H_6	1.14	0.52	-0.56	-0.52	-2.00	-1.67	-1.5
NF_3	2.59	0.60	-	-1.83	-2.12	-2.74	-
Acetone	1.69	0.82	-	-0.41	-2.33	-1.79	-1.5
N_2O	2.20	0.93	-1.35	-1.32	-2.46	-2.40	-2.2
Furan	0.90	0.19	-0.63	1.08	-2.49	-2.22	-
DMSO	0.79	0.49	-0.44	-0.38	-2.81	-1.91	-
C_2H_4	1.03	0.33	-0.78	-0.87	-2.97	-2.59	-1.8
CO	2.12	1.17	-1.21	-1.08	-3.06	-2.52	-2.2
CH_3Cl	1.03	0.49	-0.56	-0.51	-3.32	-2.58	-3.7
N_2	2.12	1.09	-1.84	-1.85	-3.49	-2.81	-2.2
C_2H_6	0.49	0.19	-0.70	-0.64	-3.66	-2.65	-
C_2H_2	0.44	-0.03	-0.68	-0.27	-3.92	-3.21	-2.6
NH_3	0.84	0.49	-0.65	-0.51	-3.95	-2.95	-3.7
CO_2	0.95	0.54	-3.74	-0.90	-4.26	-2.81	-3.8
CH_4	0.46	0.19	-0.73	-0.69	-4.43	-3.31	-3.7
CH_3F	0.54	0.24	-0.66	-0.60	-4.49	-3.16	-3.7
H_2O	1.12	0.68	-0.61	-0.52	-4.50	-3.30	-3.7
HF	1.22	0.73	-0.66	-0.59	-5.55	-4.11	-3.7
H_2	-0.05	-0.38	-1.27	-1.23	-6.22	-5.11	-2.0
Mean(+)	4.72	3.84	1.21	1.02	0.40	0.87	1.04
Mean(–)	1.22	0.55	-1.00	-0.71	-3.50	-2.76	-2.69
RMS(+)	3.84	3.01	0.83	1.05	1.13	0.83	
RMS(–)	4.01	3.39	1.96	2.15	1.32	0.91	

Table A.9 Calculated and experimental vertical electron affinities. Values are shown in eV. KT = Koopmans' theorem, TT = Tozer's theorem. B3LYP was used to calculate ionisation energies for use in Tozer's theorem as calculations using BLYP frequently fails to converge for open shell cations. The basis set used was aug-cc-pVDZ in all cases. Literature values given in parenthesis are obtained by other methods than electron transmission spectroscopy (ETS) or laser photoelectron spectroscopy (LPES). Mean(+) = mean value of species with reported positive EA. Mean(–) = mean value of species with reported negative values of EA. RMS(+) = root mean square of species with reported positive EA. RMS(–) = root mean square of species with reported negative EA.

	IE KT	IE KT	IE ΔSCF	IE ΔSCF	Literature
Molecule	BLYP	B3LYP	BLYP	B3LYP	Ref [1]
O_2	-	7.59	-	11.75	12.07
O_3	7.97	9.58	12.57	12.80	12.73
Quinone	6.31	7.76	9.22	9.91	10.00
Cl_2	7.35	8.60	11.24	11.60	11.54
C_5H_4O	5.99	6.99	-	9.29	9.49
SO_2	7.92	9.36	11.93	12.37	12.51
SF_6	10.26	12.19	13.73	15.08	15.72
Glyoxal	6.31	7.70	9.93	10.44	10.58
SF_4	8.82	10.15	12.62	13.00	12.45
F_2	9.58	11.51	15.46	15.95	15.70
SO_3	8.19	9.80	12.05	12.71	12.81
C_6F_6	6.80	7.89	-	9.74	10.09
CF_3NO_2	8.00	9.36	11.90	12.66	-
CH_2O	6.20	7.65	10.68	10.87	10.10
C_6H_6	6.10	7.05	9.03	9.24	9.24
NF_3	8.95	10.31	13.35	13.65	13.73
Acetone	5.61	7.02	9.38	9.63	9.71
N_2O	8.27	9.61	12.72	12.93	12.89
Furan	5.50	6.48	8.72	8.89	8.89
DMSO	5.25	6.45	8.67	8.85	9.06
C_2H_4	6.53	7.62	10.45	10.54	10.54
CO	9.03	10.53	13.93	14.22	14.01
CH_3Cl	6.97	8.25	11.04	11.32	11.30
N_2	10.20	11.92	15.33	15.82	15.59
C_2H_6	8.05	9.36	-	12.20	12.02
C_2H_2	6.97	8.14	11.19	11.32	11.46
NH_3	6.12	7.48	10.93	10.92	10.85
CO_2	8.60	10.45	13.35	13.81	13.78
CH_4	9.31	10.69	13.79	14.20	13.60
CH_3F	8.03	9.66	12.65	13.06	13.05
H_2O	7.16	8.79	12.70	12.77	12.61
HF	9.58	11.51	16.26	16.35	16.12
H_2	10.20	11.65	16.23	16.37	15.43
Mean	7.69	9.06	11.94	12.25	12.18
RMS	4.57	3.18	0.52	0.32	

Table A.10 Calculated and experimental ionisation energies of Molecules. Values are shown in eV. KT = Koopmans' theorem. The basis set was aug-cc-pVDZ in all cases.

Molecule	CH_4	NH_3	H_2O	HF
Distance [3]	1.087	1.012	0.958	0.917
Molecule	SiH_4	PH_3	H_2S	HCl
Distance [3]	1.480	1.420	1.336	1.275

Table A.11 Bond lengths between hydrogen and the heavy atom in simple hydrides. Bond lengths are displayed in Å.

1. NIST. *NIST Chemistry WebBook*. [Webpage] [cited; Available from: http://webbook.nist.gov/chemistry/.
2. R. G. Pearson, *Absolute electronegativity and hardness: Application to inorganic chemistry.* Inorg. Chem., 1988. **27**: p. 734.
3. D. R. Lide, *Handbook of Chemistry and Physics*. 85th ed. 2004: CRC Press.

Appendix B

Charge recombination

Parent	Product ion abundances upon collision with H_2								
SF_n^{2+}	SF_3^{2+}	SF_2^{2+}	SF^{2+}	S^{2+}	SF_4^{+}	SF_3^{+}	SF_2^{+}	SF^{+}	S^{+}
n = 4	-	-	-	-	-	100	14	1.3	-
n = 3	-	0.9	-	-	-	100	13	1.3	-
n = 2	-	-	-	-	-	-	100	6.8	-
n = 1	-	-	-	-	-	-	-	100	3.0
Parent	Product ion abundances upon collision with O_2								
SF_n^{2+}	SF_3^{2+}	SF_2^{2+}	SF^{2+}	S^{2+}	SF_4^{+}	SF_3^{+}	SF_2^{+}	SF^{+}	S^{+}
n = 4	-	-	-	-	-	100	14	0.9	-
n = 3	-	0.9	-	-	-	100	18	1.5	-
n = 2	-	-	-	-	-	-	100	11	-
n = 1	-	-	-	-	-	-	-	100	4.3

Table B.1 Summary of product ions upon collision of SF_n^{2+} with H_2 and O_2. The numbers given are abundances in percent of the most abundant ion in each spectrum.

Parent	Product ions upon collision with H_2			Product ions upon collision with O_2		
CX_2^{2+}	CX_2^{+}	CX^{+}	C^{+}	CX_2^{+}	CX^{+}	C^{+}
X = F	100	19	-	100	25	-
X = Cl	100	8.3	-	100	9.3	-
Parent	Product ions upon collision with H_2			Product ions upon collision with O_2		
CFX^{2+}	CFX^{+}	CF^{+}	CX^{+}	CFX^{+}	CF^{+}	CX^{+}
X = Cl	100	4.2	-	100	3.9	1.0
X = I	100	-	-	100	-	-

Table B.2 Summary of product ions upon collision of CX_2^{2+} and CFX^{2+} with H_2 and O_2. The numbers given are abundances in percent of the most abundant ion in each spectrum.

Collision with H_2										
Parent	CO_2^{+}	OCS^{+}	CS_2^{+}	CO^{+}	CS^{+}	O^{+}	S^{+}	O_2^{+}	SO^{+}	S_2^{+}
CO_2^{2+}	100	-	-	5.7	-	0.1	-	-	-	-
OCS^{2+}	-	100	-	0.07	0.3	-	0.7	-	0.03	-
CS_2^{2+}	-	-	100	-	1.5	-	0.1	-	-	0.5
Collision with O_2										
Parent	CO_2^{+}	OCS^{+}	CS_2^{+}	CO^{+}	CS^{+}	O^{+}	S^{+}	O_2^{+}	SO^{+}	S_2^{+}
CO_2^{2+}	100	-	-	6.3	-	0.2	-	-	-	-
OCS^{2+}	-	100	-	0.2	0.7	-	1.9	-	0.03	-
CS_2^{2+}	-	-	100	-	2.0	-	0.3	-	-	0.4

Table B.3 Summary of product ions upon collision of CO_2^{2+}, OCS^{2+}, and CS_2^{2+} with H_2 and O_2. The numbers given are abundances in percent of the most abundant ion in each spectrum.

Collision with H_2							
Parent	NO^+	CO^+	CF^+	C^+	N^+	O^+	F^+
NO^{2+}	100	-	-	-	0.1	0.4	-
CO^{2+}	-	100	-	0.6	-	0.3	-
CF^{2+}	-	-	100	-	-	-	-
Collision with O_2							
Parent	NO^+	CO^+	CF^+	C^+	N^+	O^+	F^+
CO^{2+}	-	100	-	0.8	-	0.6	-
CF^{2+}	-	-	100	-	-	-	-

Table B.4 Summary of product ions upon collision of NO^{2+}, CO^{2+} , and CF^{2+} with H_2 and O_2. The numbers given are abundances in percent of the most abundant ion in each spectrum.

Parent	Zn^+	$ZnAr^+$	$ZnAr_2^+$
$ZnAr^{2+}$	42	100	-
$ZnAr_2^{2+}$	25	100	50

Table B.5 Summary of product ions upon collision of $ZnAr_n^{2+}$ with O_2. The numbers given are abundances in percent of the most abundant ion in each spectrum.

H_2 Target	Heaviest	Abundance	Dominant	Abundance
$CClF^{2+}$	-	-	CF^+	4.2
$Furan^{2+}$	$C_4H_3O^+$	0.5	$C_3H_3^+$	8.5
SCO^{2+}	SO^+	0.03	S^+	0.7
CS_2^{2+}	S_2^+	0.5	CS^+	1.5
CO^{2+}	O^+	0.3	C^+	0.6
O_2 Target	Heaviest	Abundance	Dominant	Abundance
$CClF^{2+}$	CCl^+	1.0	CF^+	3.9
$Furan^{2+}$	$C_4H_3O^+$	0.2	$C_3H_3^+$	7.4
SCO^{2+}	SO^+	0.03	S^+	1.9
CS_2^{2+}	S_2^+	0.4	CS^+	2.0
CO^{2+}	O^+	0.6	C^+	0.8
O_2 Target	Intact	Abundance	Dominant	Abundance
$ZnAr_2^{2+}$	$ZnAr_2^+$	50	$ZnAr^+$	100

Table B.6 Summary of fragmentations yielding ‘inverted’ abundance. The abundances are given in percent of the most abundant product ion in each spectrum which is usually the intact monocation. The dominant fragment ions in this table are lighter than the heaviest fragment ions or the intact monocation.

Process	Relaxation	Dissociation	Decay	Excitation	Spin flip	Basis
Reactant	M^+	$\mathbf{M}^+$	M^+	$^sM^+$	$^sM^+$	
Product	M^+	$F_1^+ + F_2$	$F_1^+ + F_2$	$^s\mathbf{M}^+$	$^{s+2}\mathbf{M}^+$	
M = SF_4	-2.91	0.51	-2.40	2.76	No conv.	cc-pVTZ
M = SF_3	-0.85	3.93	3.08	7.04	6.90	cc-pVTZ
M = SF_2	-0.20	3.90	3.70	5.29	8.32	cc-pVTZ
M = SF	-0.11	4.00	3.89	5.74	9.97	cc-pVTZ
M = CF	-0.04	7.92	7.88	8.64	**4.84**	cc-pVTZ
M = CF_2	-3.15	3.48	0.33	2.01	10.23	cc-pVTZ
M = CFCl	-1.64	2.72	1.08	3.08	6.26	cc-pVTZ
M = CCl_2	-0.75	3.16	2.41	3.69	4.90	cc-pVTZ
M = CFI	-1.06	2.31	1.25	2.11	4.07	LANL2DZ
M = C_4H_4O	-0.30	2.01	1.71	**1.70**	4.69	cc-pVTZ
M = C_6H_5Br	-0.26	3.86	3.60	**1.47**	3.79	cc-pVTZ
M = C_3HF_3	-0.66	1.33	0.67	2.65	4.34	cc-pVTZ
M = CO_2	-0.11	6.08	5.97	**3.87**	7.27	cc-pVTZ
M = OCS	-0.23	2.69	2.46	5.10	5.23	cc-pVTZ
M = CS_2	-0.01	5.22	5.21	**3.09**	**3.35**	cc-pVTZ
M = CO	-0.03	8.45	8.42	**3.18**	**8.01**	cc-pVTZ
M = NO	-0.02	11.17	11.15	**9.88**	**7.47**	cc-pVTZ
M = ZnAr	-0.25	0.29	0.04	5.11	11.12	cc-pVTZ*
M = $ZnAr_2$	-0.75	0.14	-0.61	3.70	10.33	cc-pVTZ*

Table B.7 Energies required for reaction by cations formed vertically by recombination. Bold characters denote relaxed geometry, electronically excited states, and requiring energy to fragment in the second, third, and later rows respectively. Energies are shown in eV and were calculated using B3LYP with the basis set shown in the last column where cc-pVTZ* has G3MP2LARGE on the zinc atom. Excited states were calculated using the random phase approximation. 'Relaxation' is the energy difference between vertical and adiabatic formation of M^+. 'Dissociation' is the dissociation energy of M^+ while 'Decay' is the energy required to dissociate vertically formed M^+. 'Excitation' is the energy required to excite M^+ while preserving its spin. 'Spin flip' is the energy required to excite M^+ while increasing the overall spin by two.

Quantity	RE_a	RE_v	RE_v	
Reactant	M^{2+}	M^{2+}	M^{2+}	
Product	$^{s}M^{+}$	$^{s}M^{+}$	$^{s+2}M^{+}$	Basis
M = SF_4	14.56	11.80	No convergence	cc-pVTZ
M = SF_3	20.85	13.81	13.95	cc-pVTZ
M = SF_2	19.82	14.53	11.50	cc-pVTZ
M = SF	21.23	15.49	11.26	cc-pVTZ
M = CF	25.87	17.23	21.03	cc-pVTZ
M = CF_2	17.72	15.71	7.49	cc-pVTZ
M = CFCl	16.24	13.16	9.98	cc-pVTZ
M = CCl_2	15.20	11.51	10.30	cc-pVTZ
M = CFI	15.42	13.31	11.35	LANL2DZ
M = C_4H_4O	16.60	14.90	11.91	cc-pVTZ
M = C_6H_5Br	14.41	12.94	10.62	cc-pVTZ
M = CF_3CCH	18.97	16.32	14.63	cc-pVTZ
M = CO_2	23.58	19.71	16.31	cc-pVTZ
M = OCS	18.77	13.67	13.54	cc-pVTZ
M = CS_2	16.91	13.82	13.56	cc-pVTZ
M = CO	28.09	24.91	20.08	cc-pVTZ
M = NO	29.54	19.66	22.07	cc-pVTZ
M = ZnAr	15.77	10.66	4.65	cc-pVTZ*
M = $ZnAr_2$	13.61	9.91	3.28	cc-pVTZ*

Table B.8 Recombination energies to several electronic states. Values were calculated using B3LYP and are shown in eV. RE_a = recombination energy (adiabatic) and RE_v = recombination energy (vertical). The last column shows the basis set used. The basis set cc-pVTZ* contain G3MP2LARGE on the zinc atom. These values were used to calculate curve crossing distances.

Appendix C

Metal halides

L = RX	Monocation			Dication			Salt		
R = Me	ML_n^+			ML_n^{2+}			MXL_{n-1}^+		
X = F	MIN	MAX	M–**X**	MIN	MAX	M–**X**	MIN	MAX	M–**X**
M	n = 1	n = 1	n = 1	n = 1	n = 1	n = 1	n = 1	n = 1	n = 1
Mg	1.901	1.901	1.901	1.809	1.809	1.809	1.713	1.713	1.713
Ca	2.292	2.292	2.292	2.179	2.179	2.179	2.032	2.032	2.032
Mn	2.046	2.046	2.046	1.862	1.862	1.862	1.742	1.742	1.742
Cu	1.935	1.935	1.935	1.918	1.918	1.918	1.750	1.750	1.750
Zn	1.996	1.996	1.996	1.812	1.812	1.812	1.744	1.744	1.744
M	n = 2	n = 2	n = 2	n = 2	n = 2	n = 2	n = 2	n = 2	n = 2
Mg	1.940	1.943	1.286	1.827	1.827	0.207	1.724	1.856	0.128
Ca	2.310	2.310	1.358	2.199	2.199	1.149	2.050	2.236	1.074
Mn	2.085	2.091	1.370	1.915	1.915	0.431	1.752	1.993	0.203
Cu	1.931	1.932	0.017	1.835	1.835	0.032	1.741	1.899	0.081
Zn	2.055	2.055	1.279	1.836	1.836	0.016	1.747	1.887	0.072
M	n = 3	n = 3	n = 3	n = 3	n = 3	n = 3	n = 3	n = 3	n = 3
Mg	1.980	1.982	1.045	1.849	1.850	0.007	1.733	1.883	0.129
Ca	2.333	2.345	1.279	2.214	2.215	0.277	2.062	2.249	0.198
Mn	2.130	2.143	1.139	1.965	1.968	0.113	1.777	2.047	0.264
Cu	1.985	2.083	0.341	1.869	1.893	0.199	1.794	1.929	0.397
Zn	2.105	2.151	1.200	1.892	1.895	0.028	1.773	1.960	0.226
M	n = 4	n = 4	n = 4	n = 4	n = 4	n = 4	n = 4	n = 4	n = 4
Mg	2.020	2.079	0.871	1.880	1.882	0.003	1.769	1.923	0.079
Ca	2.350	2.440	1.059	2.229	2.235	0.008	2.096	2.296	0.239
Mn	2.163	2.284	0.978	2.009	2.027	0.017	1.826	2.112	0.205
Cu	2.099	2.100	0.006	1.939	1.941	0.002	1.785	2.010	0.153
Zn	2.175	2.250	1.000	1.936	1.940	0.022	1.818	2.012	0.122

Table C.1 Calculated MX bond lengths of complexes for L = RX = CH_3F. The three distances shown for each complex are the smallest MX distance in the complex, the largest MX distance in the complex, and the distance between the metal atom M and the centre of mass of the halogen atoms (**X** in bold). Geometries were optimised using B3LYP with LANL2DZ and all distances are shown in Å.

L = RX	Monocation			Dication			Salt		
R = Me	ML_n^+			ML_n^{2+}			MXL_{n-1}^+		
X = Cl	MIN	MAX	M–**X**	MIN	MAX	M–**X**	MIN	MAX	M–**X**
M	n = 1	n = 1	n = 1	n = 1	n = 1	n = 1	n = 1	n = 1	n = 1
Mg	2.575	2.575	2.575	2.309	2.309	2.309	2.190	2.190	2.190
Ca	2.935	2.935	2.935	2.706	2.706	2.706	2.578	2.578	2.578
Mn	2.641	2.641	2.641	2.284	2.284	2.284	2.181	2.181	2.181
Cu	2.296	2.296	2.296	-	-	-	2.240	2.240	2.240
Zn	2.586	2.586	2.586	2.249	2.249	2.249	2.158	2.158	2.158
M	n = 2	n = 2	n = 2	n = 2	n = 2	n = 2	n = 2	n = 2	n = 2
Mg	2.614	2.662	1.865	2.358	2.359	0.000	2.199	2.433	0.216
Ca	3.009	3.068	2.311	2.734	2.735	0.238	2.591	2.845	0.759
Mn	2.644	2.702	1.806	2.336	2.341	0.003	2.184	2.446	0.137
Cu	2.289	2.289	0.020	2.272	2.272	0.158	2.193	2.285	0.074
Zn	2.715	2.719	0.071	2.301	2.305	0.141	2.158	2.392	0.131
M	n = 3	n = 3	n = 3	n = 3	n = 3	n = 3	n = 3	n = 3	n = 3
Mg	2.646	2.727	1.502	2.413	2.415	0.022	2.223	2.470	0.190
Ca	3.037	3.110	1.859	2.751	2.757	0.044	2.615	2.894	0.543
Mn	2.703	2.784	1.533	2.435	2.440	0.039	2.234	2.520	0.124
Cu	2.390	2.408	0.065	2.316	2.381	0.450	2.195	2.394	0.324
Zn	2.724	2.772	1.368	2.376	2.378	0.019	2.192	2.455	0.257
M	n = 4	n = 4	n = 4	n = 4	n = 4	n = 4	n = 4	n = 4	n = 4
Mg	2.719	2.940	1.149	2.467	2.471	0.024	2.262	2.531	0.216
Ca	3.073	3.221	1.584	2.802	2.826	0.055	2.642	2.901	0.357
Mn	2.768	3.010	1.157	2.501	2.511	0.026	2.273	2.578	0.204
Cu	2.481	2.483	0.006	2.409	2.422	0.082	2.242	2.465	0.175
Zn	2.784	2.975	0.972	2.443	2.448	0.029	2.226	2.543	0.262

Table C.2 Calculated MX bond lengths of complexes for L = RX = CH_3Cl. The three distances shown for each complex are the smallest MX distance in the complex, the largest MX distance in the complex, and the distance between the metal atom M and the centre of mass of the halogen atoms (**X** in bold). Geometries were optimised using B3LYP with LANL2DZ and all distances are shown in Å.

X = F	ML_n^+		ML_n^{2+}		MXL_{n-1}^+	
n = 2	MIN	MAX	MIN	MAX	MIN	MAX
M = Mg	97		167		173	
M = Ca	108		117		120	
M = Mn	98		154		170	
M = Cu	179		178		179	
M = Zn	103		179		179	
n = 3	MIN	MAX	MIN	MAX	MIN	MAX
M = Mg	94	95	120	121	111	124
M = Ca	92	94	113	127	112	131
M = Mn	93	95	114	131	102	129
M = Cu	93	146	106	139	99	162
M = Zn	86	100	118	122	103	129
n = 4	MIN	MAX	MIN	MAX	MIN	MAX
M = Mg	82	157	109	110	101	122
M = Ca	72	150	109	110	84	124
M = Mn	78	156	108	110	97	137
M = Cu	96	143	90	180	88	180
M = Zn	78	145	108	110	100	129

Table C.3 Calculated angles of complexes for L = RX = CH_3F. Geometries were optimised using B3LYP with LANL2DZ. Metals coordinated by 2, 3, and 4 halogen atoms are vertices of 1, 3, and 6 angles respectively but only the smallest and largest of those angles are shown.

X = Cl	ML_n^+		ML_n^{2+}		MXL_{n-1}^+	
n = 2	MIN	MAX	MIN	MAX	MIN	MAX
M = Mg	90		180		171	
M = Ca	81		170		148	
M = Mn	95		180		178	
M = Cu	179		172		177	
M = Zn	177		173		177	
n = 3	MIN	MAX	MIN	MAX	MIN	MAX
M = Mg	86	101	119	121	112	129
M = Ca	78	100	117	122	95	151
M = Mn	86	101	119	122	115	123
M = Cu	117	125	101	151	98	135
M = Zn	90	107	119	121	107	133
n = 4	MIN	MAX	MIN	MAX	MIN	MAX
M = Mg	81	169	104	119	100	131
M = Ca	75	153	105	113	93	144
M = Mn	80	168	104	116	104	127
M = Cu	106	117	88	152	86	155
M = Zn	84	172	105	117	100	128

Table C.4 Calculated angles of complexes for L = RX = CH_3Cl. Geometries were optimised using B3LYP with LANL2DZ. Metals coordinated by 2, 3, and 4 halogen atoms are vertices of 1, 3, and 6 angles respectively but only the smallest and largest of those angles are shown.

L = RX	ML_n^+		ML_n^{2+}		MXL_{n-1}^+	
n = 2	X = F	X = Cl	X = F	X = Cl	X = F	X = Cl
M = Mg	N	R	R	R	V	R
M = Ca	R	R	N	V	N	V
M = Mn	R	R	R	V	V	N
M = Cu	N	N	R	R	N	N
M = Zn	N	R	R	R	N	N
n = 3	X = F	X = Cl	X = F	X = Cl	X = F	X = Cl
M = Mg	V	R	R	V	R	N
M = Ca	R	R	V	R	N	R
M = Mn	R	R	V	R	R	R
M = Cu	V	N	V	N	N	N
M = Zn	R	R	R	N	R	N
n = 4	X = F	X = Cl	X = F	X = Cl	X = F	X = Cl
M = Mg	R	R	R	R	R	R
M = Ca	N	R	R	R	R	N
M = Mn	N	R	R	R	N	R
M = Cu	V	N	N	V	V	R
M = Zn	R	R	R	N	R	R

Table C.5 Imaginary frequencies of complexes for L = RX = CH_3F and CH_3Cl. Rotational frequencies rotate ligands around RX or MX axes. Vibrational frequencies bend $M<X_1X_2$ angles. N = No imaginary frequencies. R = Rotational frequencies only. V = Vibrational frequencies.

IE	MF	MF [1]	MCl	MCl [1]	M [2]	M^+ [2]
M = Me	12.48	12.50	11.21	11.26	9.84	-
M = Mg	8.07	7.68	7.90	7.49	7.65	15.04
M = Ca	6.03	5.83	6.19	5.86	6.11	11.87
M = Mn	7.98	8.50	7.79	-	7.43	15.64
M = Cu	10.77	10.15	10.13	10.70	7.73	20.29
M = Zn	9.54	-	9.01	-	9.39	17.96

Table C.6 Adiabatic ionisation energies of examined species. Values were calculated using B3LYP with G3MP2LARGE and are shown in eV. Me = CH_3.

BDE	MF	MF [2]	MCl	MCl [2]	MF^+	MCl^+	IE(M)	IE(M^+)
M = Me	4.87	4.89	3.58	3.68	2.20	2.23	9.84	-
M = Mg	4.51	4.79	3.16	3.40	4.17	2.99	7.65	15.04
M = Ca	5.56	5.46	4.08	4.24	5.68	4.05	6.11	11.87
M = Mn	4.64	4.38	3.45	3.51	4.19	3.18	7.43	15.64
M = Cu	4.10	4.28	3.53	3.92	1.41	1.47	7.73	20.29
M = Zn	2.95	3.81	2.02	2.37	2.86	2.46	9.39	17.96

Table C.7 Bond dissociation energies of examined species. Values were calculated using B3LYP with G3MP2LARGE and are shown in eV. Me = CH_3.

L = RX	R = CH_3	$ML_n^+ \rightarrow ML_{n-1}^+ + L$			
X = F	n = 1	n = 2	n = 3	n = 4	IE(M) [2]
M = Mg	1.18	0.85	0.65	0.40	7.65
M = Ca	1.06	0.87	0.60	0.47	6.11
M = Mn	1.03	0.74	0.58	0.37	7.43
M = Cu	1.33	1.34	0.51	0.41	7.73
M = Zn	1.15	0.77	0.55	0.34	9.39
X = Cl	n = 1	n = 2	n = 3	n = 4	IE(M) [2]
M = Mg	0.93	0.66	0.47	0.28	7.65
M = Ca	0.67	0.55	0.40	0.38	6.11
M = Mn	0.93	0.67	0.48	0.28	7.43
M = Cu	1.72	1.55	0.55	0.35	7.73
M = Zn	1.25	0.63	0.55	0.30	9.39

Table C.8 Binding energies of ligands in ML_n^+ complexes for L = RX = CH_3F and CH_3Cl. Geometries were optimised using B3LYP with LANL2DZ. Energies were calculated using B3LYP with G3MP2LARGE and displayed in eV. Literature values of first ionisation energies of the metal atoms are also listed.

L = RX	R = CH_3	$ML_n^{2+} \rightarrow ML_{n-1}^{2+} + L$			
X = F	n = 1	n = 2	n = 3	n = 4	IE(M^+) [2]
M = Mg	3.59	2.99	2.22	1.71	15.04
M = Ca	2.52	2.08	1.75	1.47	11.87
M = Mn	3.55	2.79	1.92	1.57	15.64
M = Cu	4.72	3.29	1.84	2.20	20.29
M = Zn	4.29	3.37	2.07	1.59	17.96
X = Cl	n = 1	n = 2	n = 3	n = 4	IE(M^+) [2]
M = Mg	3.40	2.71	1.89	1.39	15.04
M = Ca	2.18	1.67	1.31	1.21	11.87
M = Mn	3.66	2.67	1.92	1.36	15.64
M = Cu	-	3.04	2.12	1.30	20.29
M = Zn	5.07	3.47	1.90	1.31	17.96

Table C.9 Binding energies of ligands in ML_n^{2+} complexes for L = RX = CH_3F and CH_3Cl. Geometries were optimised using B3LYP with LANL2DZ. Energies were calculated using B3LYP with G3MP2LARGE and displayed in eV. $Cu(CH_3Cl)^{2+}$ always dissociated during geometry optimisation. Literature values of second ionisation energies of the metal atoms are also listed.

L = RX	R = CH_3	$MXL_{n-1}^+ \rightarrow MXL_{n-2}^+ + L$			
X = F	n = 2	n = 3	n = 4	IE(M) [2]	IE(M^+) [2]
M = Mg	2.10	1.49	1.14	7.65	15.04
M = Ca	1.27	1.11	0.90	6.11	11.87
M = Mn	1.79	1.08	0.90	7.43	15.64
M = Cu	2.02	1.47	1.08	7.73	20.29
M = Zn	2.26	1.22	0.91	9.39	17.96
X = Cl	n = 2	n = 3	n = 4	IE(M) [2]	IE(M^+) [2]
M = Mg	1.74	1.28	0.81	7.65	15.04
M = Ca	1.00	0.91	0.84	6.11	11.87
M = Mn	1.64	1.10	0.74	7.43	15.64
M = Cu	1.92	1.10	0.55	7.73	20.29
M = Zn	2.19	1.11	0.67	9.39	17.96

Table C.10 Binding energies of ligands in MXL_n^+ complexes for L = RX = CH_3F and CH_3Cl. Geometries were optimised using B3LYP with LANL2DZ. Energies were calculated using B3LYP with G3MP2LARGE and displayed in eV. Literature values of first and second ionisation energies of metal atoms are also listed.

1. NIST. *NIST Chemistry WebBook*. [Webpage] [cited; Available from: http://webbook.nist.gov/chemistry/.
2. D. R. Lide, *Handbook of Chemistry and Physics*. 85th ed. 2004: CRC Press.

Appendix D

Basis sets

Basis	IE(Mg)	IE(Ca)	IE(Mn)	IE(Cu)	IE(Zn)	RMS
LANL2DZ	7.69	6.44	7.88	7.83	9.17	0.12
6-31G	7.75	6.15	7.31	9.48	8.95	0.36
6-31G*	7.73	6.15	7.31	8.50	8.95	0.18
VDZ	7.71	6.21	7.47	7.52	9.15	0.07
VTZ	7.72	6.15	7.43	7.66	9.19	0.04
G3MP2L	7.73	6.16	7.53	8.08	9.45	0.08
Ref [1]	7.65	6.11	7.43	7.73	9.39	-
Basis	IE(Mg^+)	IE(Ca^+)	IE(Mn^+)	IE(Cu^+)	IE(Zn^+)	RMS
LANL2DZ	14.62	11.77	15.30	20.78	17.21	0.21
6-31G	15.42	12.10	15.64	16.63	17.81	0.74
6-31G*	15.46	12.10	15.64	17.63	17.81	0.54
VDZ	15.31	12.02	15.63	20.66	17.99	0.10
VTZ	15.44	12.08	15.82	20.52	18.18	0.12
G3MP2L	15.46	12.07	15.91	20.78	18.40	0.17
Ref [1]	15.04	11.87	15.64	20.29	17.96	-

Table D.1 Ionisation energies of metal atoms. Values were calculated using B3LYP and shown in eV. Calculated values are compared to literature values and the last column displays the root mean square difference (RMS) between calculated and literature values for each basis set.

Basis	IE(F)	IE(Cl)	IE(CH_3F)	IE(CH_3Cl)	IE(CH_3)	RMS
LANL2DZ	17.42	13.18	12.53	11.36	9.76	0.05
6-31G	17.42	13.04	12.53	11.32	9.76	0.03
6-31G*	17.38	13.03	12.27	11.21	9.74	0.05
VDZ	17.56	12.94	12.61	11.27	9.88	0.04
VTZ	17.70	13.07	12.80	11.36	9.91	0.09
G3MP2L	17.76	13.06	12.48	11.21	9.91	0.07
Ref [1]	17.42	12.97	12.50	11.26	9.84	-

Table D.2 Ionisation energies of non-metallic species. Values were calculated using B3LYP and shown in eV. Calculated values are compared to literature values and the last column displays the root mean square difference (RMS) between calculated and literature values for each basis set.

BDE	M–X	M–X	M–X	M–X	M–X	R–X	
Basis	MgF	CaF	MnF	CuF	ZnF	CH_3F	RMS
LANL2DZ	4.23	3.65	4.14	3.74	2.62	4.39	0.39
6-31G	3.87	5.40	4.14	4.51	3.17	4.39	0.21
6-31G*	4.42	5.76	4.35	4.82	3.47	4.90	0.13
VDZ	2.35	2.60	2.87	3.31	1.36	4.41	0.81
VTZ	3.23	3.70	3.61	3.80	1.98	4.33	0.53
G3MP2L	4.52	5.56	4.65	4.11	2.96	4.87	0.16
Ref [1]	4.79	5.46	4.38	4.28	3.81	4.89	-
BDE	M–X	M–X	M–X	M–X	M–X	R–X	
Basis	MgCl	CaCl	MnCl	CuCl	ZnCl	CH_3Cl	RMS
LANL2DZ	3.00	3.03	2.99	3.33	1.80	3.18	0.28
6-31G	2.76	4.05	3.08	3.55	2.24	3.25	0.16
6-31G*	3.08	4.17	3.26	3.86	2.44	3.65	0.07
VDZ	1.58	2.12	2.01	2.98	0.88	3.12	0.61
VTZ	1.99	2.71	2.47	3.24	1.18	3.16	0.46
G3MP2L	3.17	4.08	3.45	3.53	2.02	3.58	0.10
Ref [1]	3.40	4.24	3.51	3.92	2.37	3.68	-

Table D.3 Bond dissociation energies of examined species. Values were calculated using B3LYP and are shown in eV. The last row displays the root mean square difference between calculated and literature values.

Basis	H	C, F	Mg	Cl	Ca	Mn, Cu	Zn
LANL2DZ	S	P	P	P	P	D	D
6-31G	S	P	P	P	D	D	D
6-31G*	S	D	D	D	D	F	F
VDZ	S	P	P	P	P	D	D
VTZ	S	P	P	P	P	D	D
G3MP2L	P	F	F	F	F	G	G

Table D.4 Maximum angular momentum basis orbitals on different atoms.

Basis	H	C, F	Mg	Cl	Ca	Mn, Cu	Zn
LANL2DZ	2	9	8	8	12	22	18
6-31G	2	9	13	13	29	29	29
6-31G*	2	15	19	19	35	36	36
VDZ	2	9	7	13	11	21	21
VTZ	3	15	13	22	23	38	38
G3MP2L	10	34	54	54	62	92	92

Table D.5 Basis functions per atom. The total number of basis set functions in a species is the sum of basis set functions on each atom in the species.

Basis	Mg	Ca	Mn	Cu	Zn	RMS
6-31G	0.42	1.33	3.92	9.82	9.32	2.83
6-31G*	0.38	1.33	3.92	9.79	9.32	2.83
VDZ	2.10	2.71	4.49	6.87	6.76	2.24
VTZ	0.06	0.35	0.75	1.89	1.42	0.50
Basis	Mg^{+}	Ca^{+}	Mn^{+}	Cu^{+}	Zn^{+}	RMS
6-31G	0.44	1.32	3.70	11.22	8.82	2.96
6-31G*	0.38	1.32	3.70	10.22	8.82	2.81
VDZ	2.08	2.76	4.43	6.32	6.47	2.13
VTZ	0.04	0.34	0.64	1.48	1.17	0.40
Basis	Mg^{2+}	Ca^{2+}	Mn^{2+}	Cu^{2+}	Zn^{2+}	RMS
6-31G	0.39	1.35	3.42	7.07	8.23	2.29
6-31G*	0.37	1.34	3.42	7.06	8.23	2.29
VDZ	1.93	2.71	4.15	6.20	6.06	2.03
VTZ	0.03	0.35	0.55	1.22	0.95	0.33

Table D.6 Estimates of basis set truncation errors of metallic species. Values displayed in eV were calculated using B3LYP as E(basis) - E(G3MP2LARGE) where basis refers to the basis set under investigation. The last column displays the root mean square difference between E(basis) and E(G3MP2LARGE).

Basis	F	Cl	CH_3F	CH_3Cl	CH_3	RMS
6-31G	1.31	1.04	2.51	2.10	0.73	0.75
6-31G*	1.26	0.90	1.76	1.37	0.53	0.55
VDZ	3.33	4.49	5.45	6.62	1.67	2.07
VTZ	-0.17	0.01	0.70	0.78	0.34	0.22
Basis	F^{+}	Cl^{+}	CH_3F^{+}	CH_3Cl^{+}	CH_3^{+}	RMS
6-31G	0.96	1.01	2.56	2.22	0.58	0.74
6-31G*	0.87	0.87	1.54	1.37	0.36	0.49
VDZ	3.12	4.36	5.58	6.69	1.64	2.07
VTZ	-0.23	0.02	1.02	0.94	0.34	0.29

Table D.7 Estimates of basis set truncation errors of non-metallic species. Values displayed in eV were calculated using B3LYP as E(basis) - E(G3MP2LARGE) where basis refers to the basis set under investigation. The last column displays the root mean square difference between E(basis) and E(G3MP2LARGE).

1. D. R. Lide, *Handbook of Chemistry and Physics*. 85th ed. 2004: CRC Press.